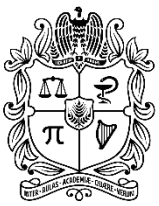

UNIVERSIDAD
NACIONAL
DE COLOMBIA

Predictive heat transfer models in fibrous insulation at high temperatures

Sergio Andrés Carvajal Perdomo

Universidad Nacional de Colombia
Facultad de Ingeniería, Departamento de Ingeniería Química y Ambiental
Bogotá, Colombia
2024

Predictive heat transfer models in fibrous insulation at high temperatures

Sergio Andrés Carvajal Perdomo

Dissertation submitted in partial fulfillment of the requirements for the degree of:

PhD. in Engineering - Chemical Engineering

Advisor:

Ph.D. José Herney Ramírez Franco

Co-Advisor:

Ph.D. Kamran Daryabeigi

Universidad Nacional de Colombia

Facultad de Ingeniería, Departamento de Ingeniería Química y Ambiental

Bogotá, Colombia

2024

Statemen of original work

Yo declaro lo siguiente:

He leído el Acuerdo 035 de 2003 del Consejo Académico de la Universidad Nacional. «Reglamento sobre propiedad intelectual» y la Normatividad Nacional relacionada al respeto de los derechos de autor. Esta disertación representa mi trabajo original, excepto donde he reconocido las ideas, las palabras, o materiales de otros autores.

Cuando se han presentado ideas o palabras de otros autores en esta disertación, he realizado su respectivo reconocimiento aplicando correctamente los esquemas de citas y referencias bibliográficas en el estilo requerido.

He obtenido el permiso del autor o editor para incluir cualquier material con derechos de autor (por ejemplo, tablas, figuras, instrumentos de encuesta o grandes porciones de texto).

Por último, he sometido esta disertación a la herramienta de integridad académica, definida por la universidad.

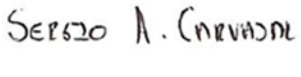

Sergio Andrés Carvajal Perdomo

19/01/2024

Acknowledgement

I would like to express my gratitude to my advisor, Professor José Herney Ramírez Franco, for his unwavering goodwill and unconditional support in both academic and administrative matters.

I especially want to thank my co-advisor, Kamran Daryabeigi, for all his edits, advice, technical discussions, data, and careful revision of the products associated with this research. My thanks will not be complete without acknowledging that Kamran's inspiring work has helped me focus my research interest on the wonderful world of thermal insulation.

I would also like to express my gratitude to Professor Matthew Berg from Kansas State University for introducing me to the welcoming atmosphere of Kansas community and allowing me to enjoy a very productive summer there.

My sincere thanks also go to Professor Carlos Arturo Martinez Riascos from UNAL for providing me with the computational resources necessary to complete the research, and my colleague Luis Carlos López Rojas for all the support with the connections and remote access. I am also grateful to Professors Hugo Ricardo Zea Ramírez and José Javier Toro Calderón from UNAL for their help in my education and honest opinions about the progress of the research.

I also want to thank my *alma mater* for giving me the opportunity to complete all my education and find friends for life.

This material is based upon work supported by the Air Force Office of Scientific Research under award number FA9550-23-1-0335. Any opinions, findings, and conclusions or recommendations expressed in this material are those of the author and do not necessarily reflect the views of the United States Air Force

Resumen

Modelos predictivos de transferencia de calor en aislantes fibroso a altas temperaturas

El modelamiento de la transferencia de calor en materiales fibrosos es importante para el diseño y mejoramiento de los sistemas de aislamiento térmico. A altas temperaturas y bajas densidades, se espera que la radiación térmica sea el principal mecanismo de transferencia de calor. Actualmente los modelos más exitosos para modelar la transferencia de calor en aislantes a altas temperaturas requieren el uso de métodos semi-empíricos. La principal limitación de este enfoque es que los parámetros del modelo deben ser determinados a partir de mediciones calorimétricas para cada posible material y determinados nuevamente si la estructura morfológica es modificada, incluso para el mismo material. Esta investigación presenta un modelo predictivo para la transferencia de calor por radiación basada exclusivamente en propiedades físicas y morfológicas. El modelo fue validado usando mediciones previamente realizadas de la conductividad térmica efectiva en un aislante de baja densidad basado en alúmina. Para distinguir los diferentes mecanismos de transferencia de calor, se analizaron mediciones en vacío y temperaturas criogénicas. El modelo muestra una buena concordancia con las mediciones; sus predicciones son consistentes con las incertidumbres estimadas para las mediciones y el modelo y son comparables con las estimaciones obtenidas a través de métodos semi-empiricos para temperaturas entre 300 K y 1700 K

Palabras clave: Aislamiento térmico, Modelamiento de transferencia de calor, Altas temperaturas, Radiación térmica, Ecuación de transferencia radiativa, Conductividad térmica, propiedades radiativas.

Abstract

Predictive heat transfer models in fibrous insulation at high temperatures

The modeling of heat transfer in fibrous materials is important for designing and improving thermal insulation systems. At high temperatures and low sample density, thermal radiation is expected to be the primary mode of heat transfer in fibrous insulation. Currently, the most common and successful models for modelling heat transfer in insulation at high temperatures require the use of semi-empirical methods. The main limitation of this approach is that the model parameters need to be determined from thermal measurements for each possible material and re-determined if the morphological structure is modified, even for the same material. This research presents a predictive model for radiation heat transfer based solely on physical and morphological properties. The model was validated using previously measured effective thermal conductivity of a low-density alumina-based insulation. In order to distinguish the different modes of heat transfer, prior measurements at vacuum and cryogenic temperatures were analyzed. The model demonstrates good agreement with experimental measurements, and its predictions are within the estimated uncertainties of both measurements and model, and is comparable to those obtained by semi-empirical methods for temperatures between 300 K and 1700 K.

Keywords: Fibrous insulation, Heat transfer modeling, High temperature, Radiation heat transfer, Radiative transfer equations (RTE), Thermal conductivity, Radiative properties

Table of contents

Pág.

List of figures

Pág.

List of tables

Pág.

List of symbols and abbreviations

Symbols with Latin letters

Symbol	Term	Unit SI	Definition
q	Heat flux	W m^{-2}	ASTM C168
x, y, z	Dimensional coordinates	-	-
k	Thermal conductivity	W m^{-1} K^{-1}	ASTM C168
T	Temperature	K	-
I	Radiant intensity	W m^{-1} sr^{-1}	-
S	Path of radiation	m	-
f	Volume fraction	-	ASTM C168
F, m	Empirical parameters	-	-
C	Cross section	m^2	-
r	Fiber radius	m	-
Q	Efficiency	-	-
k_0	wavenumber in the outer medium	m^{-1}	-
a, b	Coefficients for Mie Theory	-	-
i	Scattering intensity	-	-
$T_{1,1}, T_{1,2}, T_{2,1}, T_{2,2}$	Coefficients for Mie Theory	-	Eqs (2.4) to (2.7)
f_L	Fraction of total fiber length	-	-
$N(r)$	Distribution of number of fibers	-	-
g	Asymmetry factor	-	Eq (2.21)
G	Asymmetry scattering factor	-	Eq (2.27)
$\bar{n}$	Complex index of refraction	-	-
n	Refractive index	-	-
k	Absorption index	-	-

Symbol	Term	Unit SI	Definition
c	Velocity of light in vacuum	m s^{-1}	The International System of Units
h	Planck constant	m^2 kg s^{-1}	The International System of Units
k_B	Boltzmann constant	m^2 kg s^{-2} K^{-1}	The International System of Units
K	Parameter for multiphonon absorption model	m^{-2}	Table 2-2
ν_{max}	Parameter for multiphonon absorption model	m^{-1}	Table 2-2
D_0	Parameter for multiphonon absorption model	m^{-1}	Table 2-2
$J, \omega_0, m_{max}, M, Q', N$ $j', \rho_n, \sigma_n', \alpha_1, \alpha_2, \alpha_3$	Parameter for multiphonon absorption model	-	Eqs (2.34) to (2.41)
w_m	Parameter for discrete ordinate method	-	
$v(r)$	Fractional volume fiber	-	Eq (4.1)
L_f	Length of the fiber	m	-
ρ_b	Density of the insulation sample	kg m^{-3}	-
ρ_s	Density of the parent material of the fibers	kg m^{-3}	-
u	Standard uncertainty	-	-
u_c	Combined uncertainty	-	-
U	Expanded uncertainty	-	-
k_{ex}	Coverage factor	-	-
c_i	Sensitivity coefficient	-	-

Symbols with Greek letters

Symbol	Term	Unit SI	Definition
κ_s	Absorption coefficient	m^{-1}	-
σ	Steffan-Boltzmann constants	W m^{-2} K^{-4}	The International

Symbol	Term	Unit SI	Definition
			System of Units
λ	Wavelength	m	-
Ω	Solid angle	sr	-
β	Extinction coefficient	m^{-1}	-
β_R	Rosseland mean	m^{-1}	Eq (3.2)
σ_s	Scattering coefficient	m^{-1}	-
Φ	Phase function	-	-
θ	Polar angle	rad	-
τ	Optical thickness	-	Eq (1.8)
ϖ	Scattering albedo	-	Eq (1.7)
ϕ	Incidence angle	rad	-
ϕ_c	half apex angle	rad	$\phi_c = \lvert\pi/2 - \phi\rvert$
η	Scattering angle	rad	Eq (2.16)
μ	Cosine direction	-	-
ω	Azimuthal angle	rad	-
$\bar{\beta}$	Modified extinction coefficient	m^{-1}	Eq (2.26)
ν	Wavenumber	m^{-1}	-
$\nu_i, \Delta\epsilon_i, a1, a2, b1, b2$	Parameters for Sellmeier equation	-	Table 2-1
ν_i	Degrees of freedom of i	-	Eq (C. 4)
α	Thermal diffusivity	$m^2\ s^{-1}$	-
C_p	Specific heat	$J\ kg^{-1}\ K^{-1}$	-
a_i	Coefficient of polynomial	-	-
N_{total}	Total number of elements counted	-	-
E_n	Normalized error	-	Eq (5.12)

Subscript

Subscript	Term
R	Denotes Radiative
λ	Denotes Wavelength dependence
b	Denotes Blackbody

Subscript	Term
i	Denotes Incident direction
e	Denotes Extinction
s	Denotes Scattering
c	Denotes Conduction
g	Denotes Gas
S	Denotes Solid
L	Denotes Length
eff	Denotes Effective
r	Denotes Radiation
model	Denotes Model
int	Denotes Integral
exp	Denotes Experimental
h	Denotes Hot boundary
c	Denotes Cold boundary
LP	Denotes Low pressure

Superscript

Superscript	Term
_	Denotes Relative to the medium
*	Denotes Scaled

Abbreviations

Abbreviation	Term
TPS	Thermal Protection System
RTE	Radiative transfer equation
OFI	Opacified fibrous insulation
GHPA	Guarded hot plate apparatus
SRM	Standard Reference Material

Abbreviation	Term
NIST	National Institute of Standards and Technology
GUM	Guide to the Expression of Uncertainty in Measurement
MCRT	Monte Carlo Ray Trace Method
HFMA	Heat flux meter apparatus
NASA	National Aeronautics and Space Administration
APA	Alumina paper insulation

Introduction

Thermal insulation has been considered as one of the most important components in industrial and scientific applications where it is necessary to save energy or maintain the temperature at a desired level. In fact, energy losses to the surrounding environment represent a significant percentage of the energy consumption in processes involving heat exchange, and the research on Thermal Protection Systems (*TPS*) remains an active field (Al-Jothery et al., 2020; Le et al., 2021; Papadopoulos, 2005; Uyanna & Najafi, 2020). It is especially important at high temperatures (T>1000 K), since approximately 30 % of worldwide CO_2 emissions come from high-temperature industries such as metallurgical, petrochemical, and glass industries, and nearly 50 % of the generated energy is lost due to energy wastage(Curran & Porter, 2020). Given that radiation is the main heat transfer mechanism at high temperatures in thermal insulation, the modeling of this mechanism is fundamental in improving the insulation system performance and manufacturing process.

Depending on the application, different properties are required for a good thermal insulation system. For instance, in the insulation system used on aerospace vehicles, in addition to keeping a low thermal conductivity at extreme temperatures and high vacuum, it is necessary to use lightweight, mechanically stable and low-cost materials (Rodriguez & Snapp, 2010).

Fibrous insulation has demonstrated high effectiveness and good performance for various applications subject to extreme conditions. Materials formed from refractory ceramic fibers can be used at temperatures as high as 1900 K with thermal conductivities of the order of 0.5 W m^{-1} K^{-1} and densities of the order of 100 kg m^{-3}. The interest in this material lies on its relatively inexpensive manufacturing process, its mechanical stability, and its capability to provide effective thermal resistance to heat flow.

It has been recognized that the main heat transfer mechanism in fibrous insulation at high temperatures and low sample densities are radiation and conduction (Bhattacharyya, 1980; Daryabeigi, 2003; Verschoor et al., 1952). The success of fibrous insulation in reducing heat transfer is related to the scattering and absorption of the radiative energy by the fibers and the mitigation of gas conduction at low and intermediate pressure due to small pore size in fibers. The coupled radiation and conduction can be represented by the energy conservation equation and the radiative transfer equation (*RTE*). Given that the radiative properties depend nonlinearly on temperature, direction, and wavelength, in general, there is no analytical solution for the energy balance. However, for optically thick materials, as in the case of typical fibrous insulation samples, the combined heat transfer is usually approximated as a diffusion process.

Due to the complexity associated with estimating radiative properties and the multiple orientations and sizes of fibers in which conduction takes place, models based on semi-empirical approaches are frequently used. At high temperatures, this technique has been applied successfully on silica (Marschall et al., 2001; Milandri et al., 2002; Nicolau et al., 1994), alumina (Daryabeigi, 2001, 2010; Zhang et al., 2007, 2008; Zhao, Zhang, & Du, 2009; Zhao, Zhang, & He, 2009; Zhao, Zhang, Du, et al., 2009) and zirconia (Daryabeigi et al., 2010; Matthews et al., 1984) based insulation systems as well as opacified fibrous insulation (*OFI*) (Daryabeigi et al., 2010; Mironov, Tomchani, et al., 2021). In these models the specific extinction coefficient is inferred from measurements of effective thermal conductivity and is valid as long as the fiber size distribution, fiber orientation, complex refractive index and fiber volume fraction remain the same.

From the point of view of insulation design, an interesting alternative is the calculation of radiative properties from the morphology characteristics of fibers. These properties can be estimated for a single fiber from the Lorenz-Mie theory assuming the fiber behaves as an infinitely long cylinder and then extended to a fibrous medium containing many fibers. This approach, known as predictive to differentiate it from semi-empirical, has shown promising results on silica-based insulation between 288 K and 1366 K (Carvajal et al., 2019; Daryabeigi et al., 2008, 2010; Jeandel et al., 1993; Lee & Cunnington, 1998b, 2000). Considering the lack of information about the properties required for predictive models, most of the studies have been carried out on silica which has extensive published radiative property data. Therefore,

further validation is necessary, considering other insulation materials capable of operating at higher temperatures, in order to address the needs of high-temperature industries and aerospace research.

In this research a predictive model for radiation heat transfer is implemented for an alumina paper insulation at high temperature. The model considers independently evaluated physical and morphological properties, and is validated by comparison with existing measurements of effective thermal conductivity for temperatures between 300 K to 1700 K under vacuum conditions.

1. Heat transfer in fibrous insulation

Thermal insulation is defined as a material or an assembly of materials with the capacity to reduce or provide resistance to heat flow (ASTM C168-22, 2022; International Organization for Standardization (ISO), 2007). Figure 1-1 illustrates the heat flow process though an insulator. The energy from the body at T_h is attenuated by an insulator; some part of the energy is absorbed at the surface, some part is transmitted to the zone at T_c and the rest of the heat is reflected to the zone T_h. The proportion between the energy absorbed, transmitted and reflected will depend on the physical and chemical properties of the insulator.

Figure 1-1: Heat flow through an insulator (Own work).

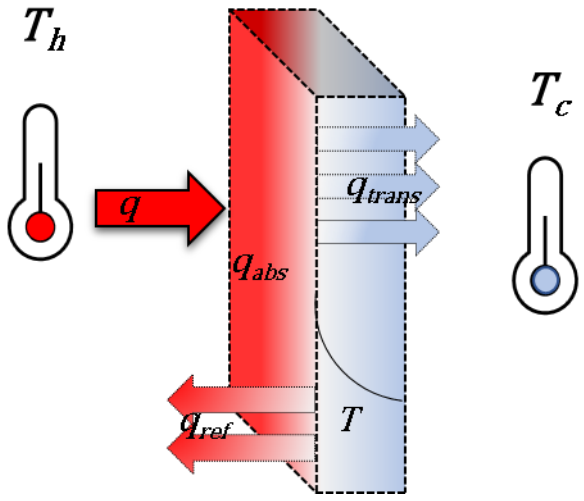

Thermal insulation is essential when it is needed to save energy, to maintain temperature at a desired level or to ensure thermal protection, and it is especially important at high temperatures because thermal losses increase rapidly with increasing temperature. In fact, energy losses to the surroundings represent a high percentage of energy consumption of

processes that involve heat exchange (Papadopoulos, 2005). The variety of applications of thermal insulation range from building, transportation and industrial process, where energy efficiency and process specification are of utmost importance (Tychanicz-Kwiecień et al., 2019), to aeronautics, where thermal protection systems are required to maintain safe conditions, since temperatures as high as 1700 K are found in reusable launch vehicles and hypersonic wave-riders due to re-entry aerodynamic heating (Rodriguez & Snapp, 2010; Vanmol & Anderson, 1992).

There are several classifications of insulation materials, but most of them can be grouped as presented in Table 1-1. The selection of the material type will depend on insulation requirements, temperature, mechanical stability, density, compressibility, durability, and costs.

Table 1-1: Classification of thermal insulation materials (Koval'chyuk et al., 1991; Okokpujie et al., 2022; Tychanicz-Kwiecień et al., 2019).

Type	Example	Approximate maximum temperature/ K
Inorganic-Fibrous	Silica glass, alumina, zirconia	~ 2000
Inorganic-Cellular	Perlite, vermiculite, calcium silicate	~1300
Organic-Fibrous	Cellulose based insulators, wood, cane	~500
Organic-Cellular	Polymeric foams such as: polystyrene, polyurethane, polyisocyanurate, polyethylene	~150
Multilayer Thermal Insulations	Metalized reflective membranes	~2000
Aerogel	Silica aerogel, Carbon composites, Alumina aerogel	~1200
Granular	Powders, diatomaceous earths	~1000

At room and moderate temperature, organic materials are widely used, given their relatively simple manufacturing processes. When weight is not a problem, granular and cellular

insulation are preferred, considering their structural stability. Aerogel insulation has received much attention recently due to its extremely low thermal conductivity and low density. However, the thermal insulation systems based on these materials are far more expensive than other types of systems and are inconvenient in real applications due to their fragility.

At high temperatures, fibrous materials are the most commonly used insulators due to their relatively inexpensive manufacturing process (in comparison with other insulation systems), their mechanical stability, their capability to reduce heat transfer, their non-toxicity, their resistance to thermal shock, and their suitability for fire protection. In industrial and aeronautic applications, low-density and temperature-stable materials with low thermal conductivities and low infrared transparency are preferred. Silica, alumina/silica, and alumina are suitable for temperatures below 2000 K. At higher temperatures, Yttria-stabilized zirconia is used due to its good resistance to erosion and thermal cycling (Fletcher, 1993). The internal structure and the modes of heat transfer in a fibrous insulator are presented in Figure 1-2 .

Figure 1-2: Scheme of a fibrous insulator (Own work).

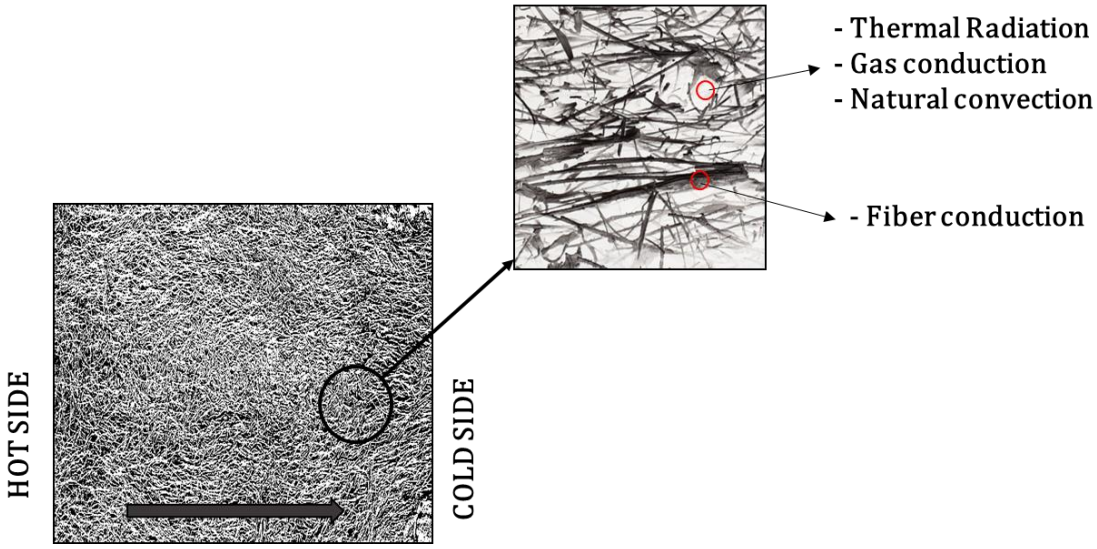

The phenomenological description of fibrous insulation has been profusely investigated. In these materials, the heat transfer is attenuated by fiber conduction, gas conduction, natural convection, and thermal radiation (Bankvall, 1974; Pelanne, 1977; Verschoor et al., 1952). The fiber conduction increases with density and is negligible for bulk densities lower than 40 kg

m^{-3}(porosity greater than 0.98) (Tong & Tien, 1980). Natural convection is negligible for bulk densities greater than approximately 20 kg m^{-3} (Bhattacharyya, 1980; Daryabeigi, 2002; Stark & Fricke, 1993). It means that gas conduction and radiation are the most relevant modes of heat transfer in low density fibrous insulation at high temperatures. Radiation increases with increasing temperature and is inversely proportional to density, while gas conduction increases with temperature and pressure. Often, reducing gas conduction is more challenging to implement than reducing radiation. Therefore, it is generally more practical to focus on improving fibrous insulation considering its radiative behavior (Kamdem & Baillis, 2010). In order to minimize the influence of gas conduction, thermal systems are typically studied under vacuum conditions, where this contribution is significantly reduced.

The overall steady-state heat transfer process for a fibrous insulator can be represented using the energy balance between two isothermal plates as shown in equations (1.1) to (1.3), where it is assumed that the fibrous material planar dimensions are large enough to mitigate heat transfer in y and z directions (see Figure 1-3), and that the natural convection and gas conduction modes of heat transfer are negligible, considering vacuum conditions (Howell et al., 2020)

$$\nabla \cdot (k\nabla T) - \frac{\partial q_R}{\partial x} = 0 \tag{1.1}$$

$$T(0) = T_0 \tag{1.2}$$

$$T(L) = T_L \tag{1.3}$$

Figure 1-3: Heat flow between isothermal plates (Own work).

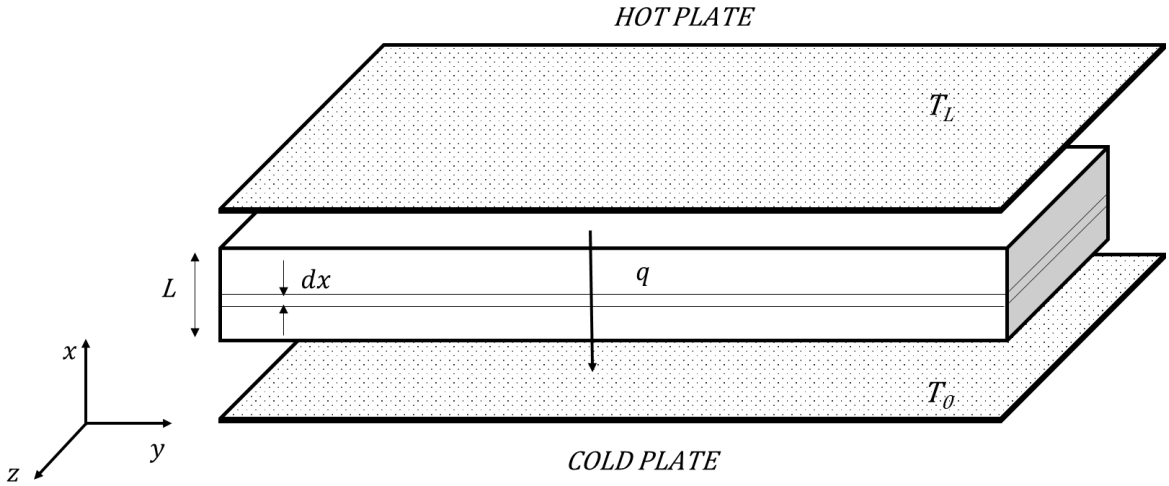

In equation (1.1), k is the thermal conductivity, T is temperature, x is the dimensional coordinate parallel to the heat flow, q_R is the radiative heat flux, L is the thickness of the material, and T_0 and T_L are the temperatures of the cold and the hot plates, respectively.

The main challenge to solve equation (1.1) is the computation of the radiative heat flux. The complexity comes from the integral nature of the radiative heat transfer (in contrast with the differential nature of conduction and convection), the spectral and directional dependence of radiation and the uncertainties associated with radiative properties (Howell et al., 2020).

1.1 Radiation

In general, the radiative heat flux for a medium with absorption and scattering can be represented according to equation (1.4) (Modest & Mazumder, 2021).

$$-\frac{\partial q_R}{dx} = -4\pi \int_0^\infty \kappa_\lambda(T) I_{\lambda b}(T)\, d\lambda + \int_0^\infty \kappa_\lambda(T) \left[\int_{\Omega_{i=0}}^{4\pi} I_\lambda(\Omega_i)\, d\Omega_i \right] d\lambda \tag{1.4}$$

Where κ is the absorption coeffcient, I is the radiant intensity, λ is the wavelength and Ω is the direction of propagation. The subscripts λ, b and i represent spectral dependence, blackbody and inicident direction, repectively. The radiant intensity in the previous equation can be calculated from the Radiative Transfer Equation (*RTE*) according to equation (1.5) (Modest & Mazumder, 2021).

$$\frac{\partial I_\lambda(S,\Omega)}{dS} = \kappa_\lambda I_{\lambda b}(S) - \beta_\lambda I_\lambda(S,\Omega) + \frac{1}{4\pi}\int_{\Omega_{i=0}}^{4\pi} I_\lambda(S,\Omega_i)\sigma_{s,\lambda}\Phi_\lambda(\Omega_i,\Omega)\,d\Omega_i \tag{1.5}$$

Where S is the path of radiation, β is the extinction coefficient, σ_s is the scattering coefficient and Φ is the scattering phase function which represents the probability that the radiation at incident direction will be scattered into other direction. For a one dimensional (1D) geometry (Figure 1-4), equation (1.5) can be expressed in terms of the optical thickness τ as:

$$-\cos\theta\frac{\partial I_\lambda(x,\theta)}{d\tau} = -(1-\varpi_\lambda)I_{\lambda b}(x) + I_\lambda(x,\theta) - \frac{1}{4\pi}\int_{\Omega_{i=0}}^{4\pi} I_\lambda(x,\Omega_i)\varpi_\lambda\Phi_\lambda(\Omega_i,\Omega)\,d\Omega_i \tag{1.6}$$

Figure 1-4: Geometry of 1D system. Adapted from (Howell et al., 2020).

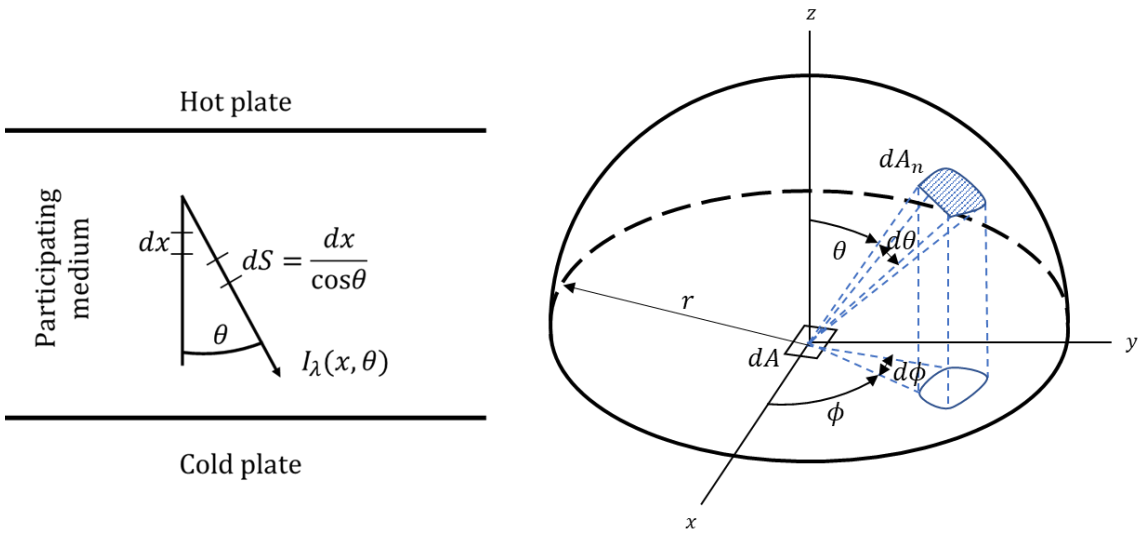

Where the scattering albedo ϖ_λ and the optical thickness τ are defined as:

$$\varpi_\lambda = \frac{\sigma_{s,\lambda}}{\beta_\lambda} \tag{1.7}$$

$$\tau = \int \beta_\lambda dS \tag{1.8}$$

Besides the complexity associated with the evaluation of the coupled integro-differential equations (1.1), (1.4)and (1.6), the modelling of the absorption and scattering coefficient as well as the scattering phase function in a medium of myriads of fibers with random orientation also constitutes an important limitation in the estimation of the radiation heat transfer in fibrous materials. Considering this, empirical and semi-empirical methods based on approximate solutions of the energy balance and the *RTE* are frequently used. In these methods, the physical and structural properties in the *RTE* are replaced by experimentally determined parameters. This technique is also known as inverse method (Alifanov, 2017; Alifanov et al., 2009; Baillis & Sacadura, 2000; Moura, 2011; Nenarokomov et al., 2019). Usually, the set of experimental data required to estimate the parameters of the models comes from spectral radiative measurements, such as transmittance and reflectance (both hemispherical and directional), or heat flux measurements, including effective thermal conductivity, thermal diffusivity, and thermal response (under steady-state or transient conditions). The main advantage of methods based on the latter approach is that the temperature dependence of the parameters can be directly obtained. However, unlike methods based on spectral radiative measurements, it is not possible to obtain wavelength dependence or anisotropic properties (Sacadura & Baillis, 2002). As pointed out by Sacadura, for most engineering applications, especially at high temperatures, where measurements of spectral dependence are difficult to implement, it is not necessary to use detailed properties (Sacadura, 2011). In such cases, heat flux measurements are sufficient for the intended purpose.

The main limitation of the empirical and semi-empirical methods is that the parameters of the model must be determined for each possible material and must be determined again, even for the same material, if the physical structure is modified i.e., if properties as fiber size or bulk density change. It is inconvenient for several reasons. Firstly, given the multiple conditions under which fibrous insulation is applied, it is a formidable task to experimentally measure all the possible combinations as temperature, pressure, sample density, fiber diameters etc.

Secondly, implementation can be particularly challenging for semi-empirical methods, considering the uncertainty in measurements and the correlation of parameters. Finally, from the point of view of insulation design, it is important to understand how the properties of the base material and the morphological arrangement of the insulation affect the heat transfer, given that it has been demonstrated that there exists an optimal fiber size (Arambakam et al., 2013, 2014; Du et al., 2009; Jeandel et al., 1993; Larkin & Churchill, 1959a; McKay et al., 1984; Yang et al., 2018) and the use of additives that modify the optical properties significantly improve the insulation properties (Reiss et al., 1987; Tong et al., 1987; Wang & Tien, 1983).

Alternatively, the radiative properties can be calculated from first-principles electromagnetic interactions, considering the complex refractive index, size, and orientation distribution of the fibers. This approach, outlined in section 2, will be referred to as the predictive method to differentiate it from empirical and semi-empirical methods. The approximate solutions of the coupled energy balance and *RTE* will be described in section 3.

1.2 Conduction

Even though at high temperatures solid conduction accounts for less than 5 % of the overall heat transfer in vacuum, its computation is required for a precise evaluation of the model. The quantification of this term in a randomly oriented medium is a very complicated task given the multiple paths, unions and shape and size distribution of the fibers. One of the first attempts to estimate the fiber conduction component was proposed by Verschoor et al.(Verschoor et al., 1952) based on the thermal network concept and semi-empirical relations as shown in equation (1.9)

$$k_c = f^m k_s \tag{1.9}$$

Where k_c is the solid conduction and it represents the thermal conductivity associated with the fiber conduction, f is the volume fraction, k_s is the thermal conductivity of material used to draw fibers from and m is an empirical parameter which depends on the orientation and number of fibers (Daryabeigi et al., 2008; Williams & Curry, 1993). The model has been evaluated for loose alumina fibrous materials, multilayer insulation and alumina/silica

insulations with m values ranged from 1 to 3 (Daryabeigi, 1999b, 2003; Hager & Steere, 1967). An analogous approach has been presented by Lee et al. and Daryabeigi et al. as shown in equation (1.10) (Daryabeigi et al., 2010; Lee & Cunnington, 1998b). Here, F is an empirical temperature-independent parameter that accounts for the conduction through the fibers.

$$k_c = F f^m k_s \tag{1.10}$$

Recently, Curran and Porter proposed a tortuosity-weighted model to incorporate solid conduction in ceramic fibrous insulation using tomographic imaging. The main advantage of this model is its ability to account for the directional orientation of the fiber (Curran & Porter, 2020).

2. Radiative and optical properties

As discussed previously, for design and engineering considerations, it is advantageous to calculate the radiative properties from first-principles. In the case of the electromagnetic interaction between fibers and radiation, the Lorenz-Mie theory can be applied, assuming that the fibers behave as infinitely long cylinders. This approach can subsequently be extended to a fibrous medium containing many fibers by considering the appropriate coordinate system, orientation, fiber size distribution, and the strong anisotropy commonly found in fibrous insulation.

This section presents the theory for estimating the radiative properties in thermal insulators. First, the single cylinder case is described, followed by the extension to a medium composed of randomly oriented fibers. Finally, various methods for estimating the optical properties, necessary for the radiative properties models, are presented and compared with reported data.

2.1 Single cylinder

The electromagnetic interaction between a single infinite cylinder and radiation is presented by Kerker, Lind, Greenberg and van de Hulst (Bohren & Huffman, 1983; Kerker, 1969; Lind & Greenberg, 1966; van de Hulst, 1981). Considering the notation of Figure 2-1, the scattering and extinction cross sections per unit of length and the respective efficiencies are given by (Kerker, 1969):

Figure 2-1: Scattering of radiation by a single cylinder.

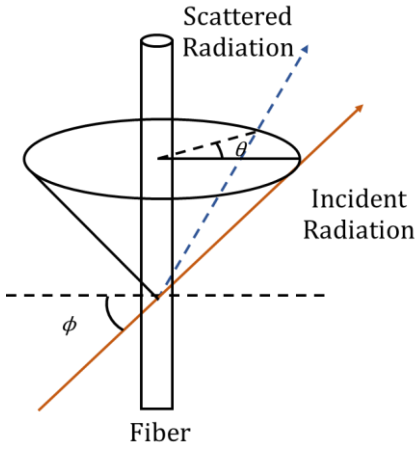

$$C_{e,\lambda}(r,\phi) = 2rQ_{e,\lambda}(r,\phi) = \frac{4}{k_0}\mathrm{Re}\left\{b_{0I} + a_{0II} + 2\sum_{n=1}^{\infty}(b_{nI} + a_{nII})\right\} \tag{2.1}$$

$$C_{s,\lambda}(r,\phi) = 2rQ_{s,\lambda}(r,\phi) = \frac{4}{k_0}\left\{|b_{0I}|^2 + |a_{0II}|^2 + 2\sum_{n=1}^{\infty}(|b_{nI}|^2 + |b_{nII}|^2 + |a_{nI}|^2 + |a_{nII}|^2)\right\} \tag{2.2}$$

Where θ is the azimuthal angle of the scattered radiation, ϕ is the incident angle of radiation, $C_{e\lambda}$ is the extinction cross section, $C_{s\lambda}$ is the scattering cross section, $Q_{e\lambda}$ is the extinction efficiency, $Q_{s\lambda}$ is the scattering efficiency, r is the radius of the cylinder, k_0 is the wavenumber in the outer medium, and a and b are coefficients that are functions of the complex index of refraction of the fiber, the incident angle, the radius of the cylinder and the wavelength. The scattering intensity is calculated as (Modest & Mazumder, 2021):

$$i_\lambda(r,\phi,\theta) = \frac{1}{2}(|T_{11}|^2 + |T_{11}|^2 + |T_{11}|^2 + |T_{11}|^2) \tag{2.3}$$

Where:

$$T_{11} = b_{0I} + 2\sum_{n=1}^{\infty} b_{nI}\cos(n\theta) \tag{2.4}$$

$$T_{12} = 2\sum_{n=1}^{\infty} a_{nI}\sin(n\theta) \tag{2.5}$$

$$T_{21} = 2\sum_{n=1}^{\infty} b_{nII}\sin(n\theta) \tag{2.6}$$

$$T_{22} = a_{0II} + 2\sum_{n=1}^{\infty} a_{nII}\cos(n\theta) \tag{2.7}$$

As shown by Cohen et al. the scattering of cylinders with aspect ratios greater than 100 is very similar to the scattering of infinite cylinders (Cohen et al., 1983). Since for most of the high temperature applications in fibrous insulation the aspect ratio exceeds 500, the infinite cylinder approximation can be applied safely (Lee & Cunnington, 1998c).

Figure 2-2 shows the extinction efficiency of a cylinder for a wavelength of 1.5 µm, which is the wavelength that produce the maximum radiant intensity at 1900 K. In order to simulate a silicate glass fiber, the refractive index was taken from Hsieh and Su (Hsieh & Su, 1979). The coefficients for the calculation of the scattering and extinction cross sections were computed from the calculation routine implemented by Schäfer (Schäfer, 2011; Schäfer et al., 2012). For the case of perpendicular incidence, the extinction paradox observed in spheres holds, as pointed out by Kerker (Kerker, 1969). When the angle tends to normal incidence, the extinction efficiency tends to higher values. In case of cylinders radiation scatters into limited angles, as shown in Figure 2-1, contrary to the case of spheres when the scattered radiation is independent of the incident angle.

Figure 2-2: Extinction efficiency for a single cylinder at several incidence angles.

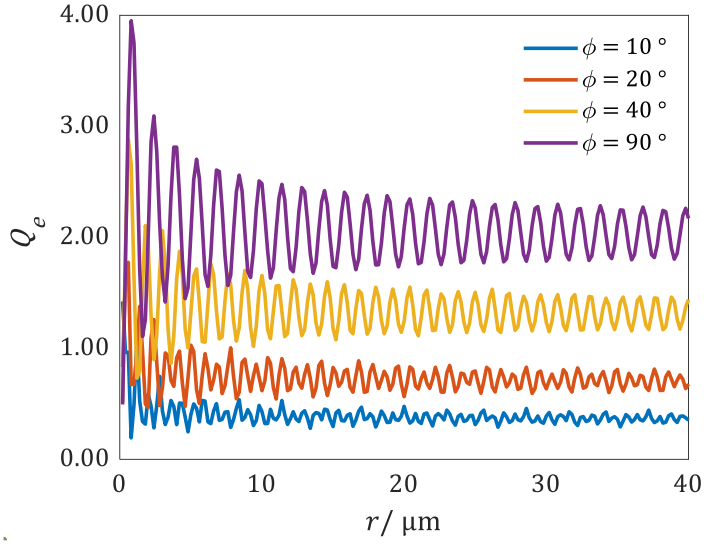

The phase function for an infinite cylinder was presented by Houston and Korpela (Houston & Korpela, 1982) as shown in equation (2.8) where a factor of two was applied by Lee considering the normalization condition of the phase function (Lee, 1986).

$$\Phi_\lambda(r,\phi,\theta) = \frac{\lambda}{\pi^2}\frac{i_\lambda(r,\phi,\theta)}{C_{s,\lambda}(r,\phi)} \tag{2.8}$$

Figure 2-3 shows the phase function at several incident angles for a glass fiber of 1 μm radius and a wavelength of 1.5 μm. In the non-absorbing region of glass, the phase function tends to be flat when the incident radiation tends to be perpendicular.

Figure 2-3: Phase function for a single cylinder.

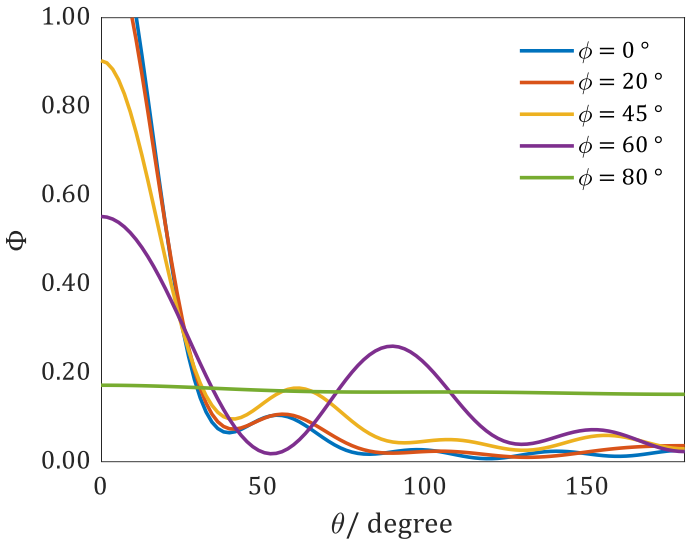

2.2 Medium of fibers

Once the radiative properties of a single fiber are determined, the extension to a medium of fibers with a given size distribution can be assessed. At this point it is convenient to differentiate between independent and dependent scattering regimes. Although the terms "independent" and "dependent" are questionable from the point of view of the first-principles analysis of the Maxwell equations (Mishchenko, 2018), in the context of fibrous materials it is appropriate to outline the difference between them. In the first case, the radiative properties of a medium are equal to the sum of those for the isolated scatterers (Deirmendjian, 1969) and it is usually found in high porosity mediums (low density materials) where the distance between the fibers is much greater that the incident wavelength (Kaviany, 1995). In the dependent regime, the additive rule is no longer valid, and both the near-field and far-field effects must be considered (Lee, 1992).

In the case of low-density fiber insulation, the conditions for independent scattering are usually fulfilled. Quantitatively, when the ratio of the distance between fibers to fiber diameter is greater than 0.4 and the distance between fibers is greater than 0.3 wavelength, independent

scattering is adequate to describe the properties of the medium assuming uniformly distributed fibers (Hottel et al., 1970). Figure 2-4 shows the demarcation between independent and dependent regimes according to the analysis presented by Lee based on a rigorous solution of the Maxwell's equations in parallel fibers, considering refractive index, size parameter ($\alpha = 2\pi r/\lambda$) and volume fraction (Lee, 1994). As expected, low density commercial thermal insulators for use at high temperatures are usually in the independent scattering zone.

Figure 2-4: Scattering regimes for fibrous insulators. Adapted from (Lee, 1994).

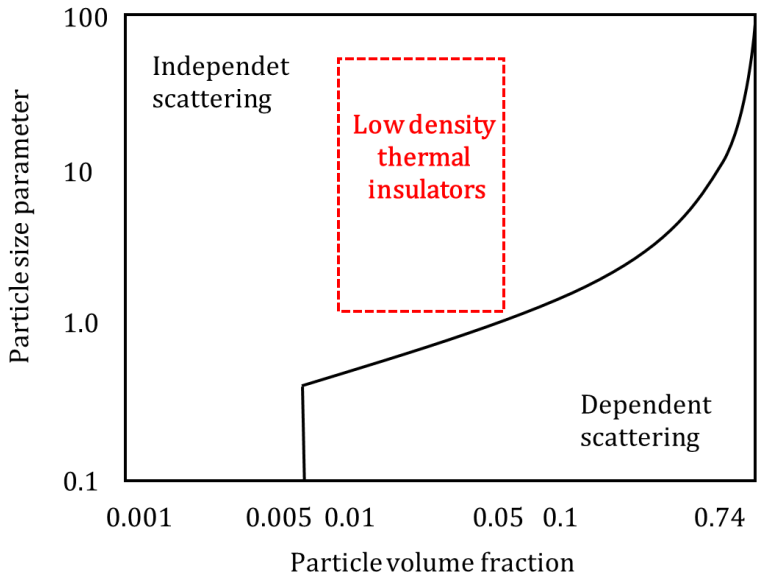

Considering independent scattering and randomly oriented fibers, the scattering and absorption cross sections averaged over all incident angles for a fibrous material with a distribution function $f_L(r)$, based on the length of the fiber, were derived initially by Houston (Houston, 1980) according to equations (2.9) to (2.10).

$$\bar{C}_{e,\lambda} = \int_0^{\infty} \int_0^{\frac{\pi}{2}} C_{e,\lambda}(r,\phi)\cos\phi f_L(r) d\phi dr \tag{2.9}$$

$$\bar{C}_{s,\lambda} = \int_0^{\infty} \int_0^{\frac{\pi}{2}} C_{s,\lambda}(r,\phi)\cos\phi f_L(r) d\phi dr \tag{2.10}$$

In equations (2.9) and (2.10) the distribution function $f_L(r)$ represents the fraction of total fiber length having radii between r and $r + dr$ and must be evaluated from the fiber size distribution considering the length of the fibers. The extinction and scattering efficiencies of the medium can be written as:

$$\bar{Q}_{e,\lambda} = \int_0^{\infty} \int_0^{\frac{\pi}{2}} \frac{C_{e,\lambda}(r,\phi)}{2r}\cos\phi f_L(r) d\phi dr \tag{2.11}$$

$$\bar{Q}_{s,\lambda} = \int_0^{\infty} \int_0^{\frac{\pi}{2}} \frac{C_{s,\lambda}(r,\phi)}{2r}\cos\phi f_L(r) d\phi dr \tag{2.12}$$

Figure 2-5 presents the extinction efficiency calculated for several size distributions of glass fibers from equation (2.11) at a wavelength of 1.5 μm for a medium of randomly oriented glass fibers. The x axis represents the mean radius of a normal size distribution considering a standard deviation of 5 %. Comparing figures 2-2 and 2-5, it is noted that equations (2.11) and (2.12) represent an average over all incident directions. When the mean radius increases, the extinction efficiency tends to a fixed value, as in the case of a single fiber, but the former is almost half of the value of the latter for perpendicular incidence.

Figure 2-5: Scattering efficiency of a silicate glass fibrous insulator for randomly oriented fibers.

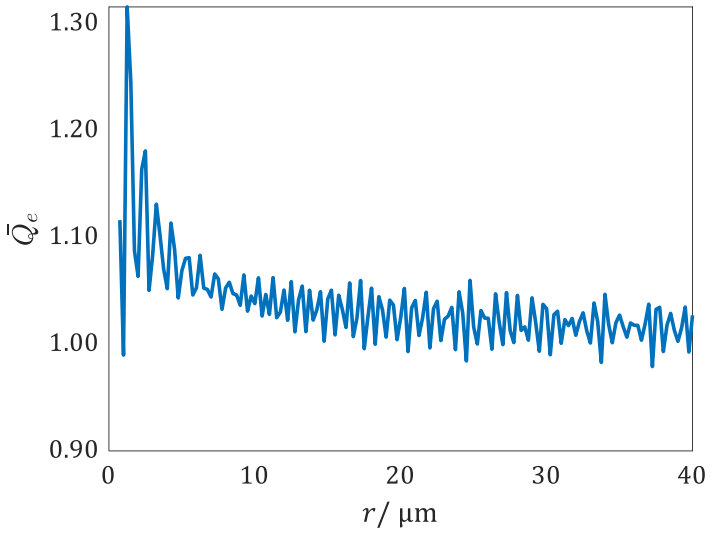

The corresponding extinction and scattering coefficients can be calculated from equations (2.13) and (2.14) as presented by Lee (Lee, 1986).

$$\beta_\lambda = \int_0^\infty \int_0^{\frac{\pi}{2}} C_{e,\lambda}(r,\phi)\cos\phi N(r) d\phi dr \tag{2.13}$$

$$\sigma_{s,\lambda} = \int_0^\infty \int_0^{\frac{\pi}{2}} C_{s,\lambda}(r,\phi)\cos\phi N(r) d\phi dr \tag{2.14}$$

Where $N(r)$ is the distribution of number of fibers having radii between r and $r + dr$. Figure 2-6 shows the extinction and scattering coefficients for a medium of glass fibers with $N(r)$ normally distributed, a mean radius of 1 µm and a standard deviation of 5 %.

Figure 2-6: Extinction and scattering coefficients of a silicate glass fibrous insulator for randomly oriented fibers.

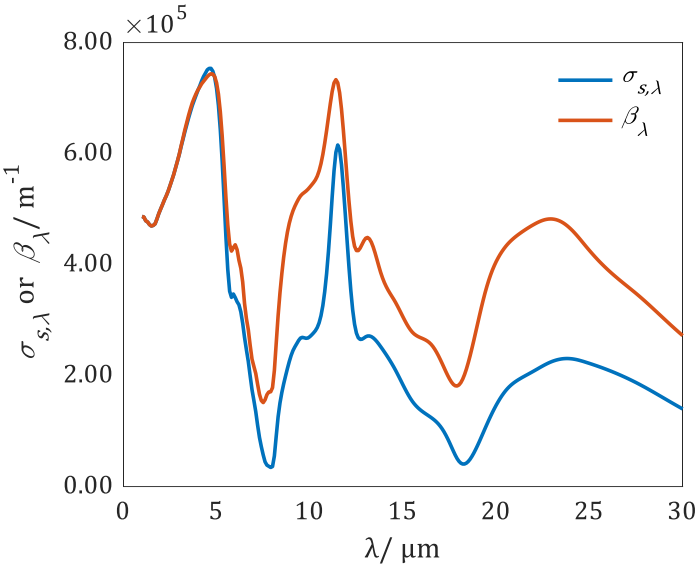

Given the ambiguity associated with radiative transfer calculation when the direction of the fiber in a medium is described according to Figure 2-1, Lee proposed to describe the phase function in terms of a global coordinate system as shown in Figure 2-7 (Lee, 1986).

Figure 2-7: Global coordinate system for a fiber oriented in space.

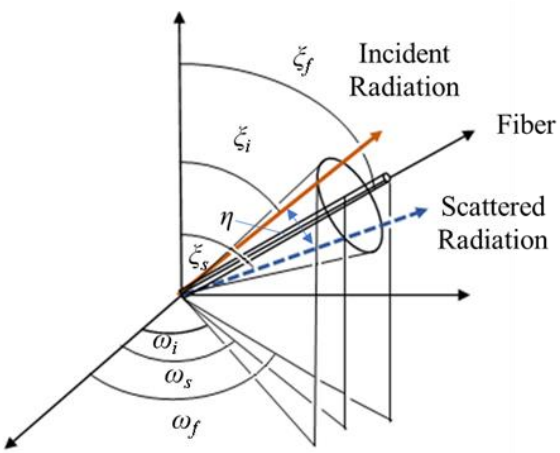

The relations between the coordinate systems of Figure 2-1 and Figure 2-7 are given by:

$$\cos\theta = \frac{\cos\eta - \sin^2\phi}{\cos^2\phi} \tag{2.15}$$

$$\cos\eta = \mu_i\mu_s + \left[(1-\mu_i^2)(1-\mu_s^2)\right]^{1/2}\cos\left(\omega_i - \omega_s\right) \tag{2.16}$$

Where η is the scattering angle, μ_i and μ_s are the incident and scattering cosine directions ($\mu_n = cos\xi_n$), and ω_i and ω_s are the corresponding azimuthal angles. This transformation allows to extend the formulation of radiative properties to medium of fibers randomly oriented in a plane, medium with aligned fibers (Lee, 1986), medium with fibers in preferential polar orientation and randomly oriented in azimuthal direction (Lee, 1989, 1990) and mixture of fibers in random and aligned orientation (Lee & Cunnington, 1998a).

For a single fiber, the phase function in equation (2.8) can be expressed in terms of the scattering angle as (Lee, 1986):

$$\Phi_\lambda(r,\phi,\eta) = \frac{4\lambda}{\pi^2}\frac{i_\lambda(r,\phi,\eta)}{C_{s,\lambda}(r,\phi)\sin\theta\cos\phi^2} \tag{2.17}$$

The phase function for medium of randomly oriented fibers can be calculated by integration over the incident angles and the fiber radius for a given size distribution, as shown in equation (2.18) (Lee, 1990).

$$\bar{\Phi}_\lambda(\eta) = \frac{\int_0^\infty \int_0^{\frac{\pi}{2}} \Phi_\lambda(r,\phi,\eta) C_{s,\lambda}(r,\phi) \cos\phi N(r) d\phi dr}{\int_0^\infty \int_0^{\frac{\pi}{2}} C_{s,\lambda}(r,\phi) \cos\phi N(r) d\phi dr} \tag{2.18}$$

Figure 2-8 shows the phase function at several wavelengths. The phase function shows a smooth dependance on the scattering angle except at small values of scattering angle, where a high forwardness is presented at all wavelengths.

Figure 2-8: Phase function for a medium of randomly oriented fibers.

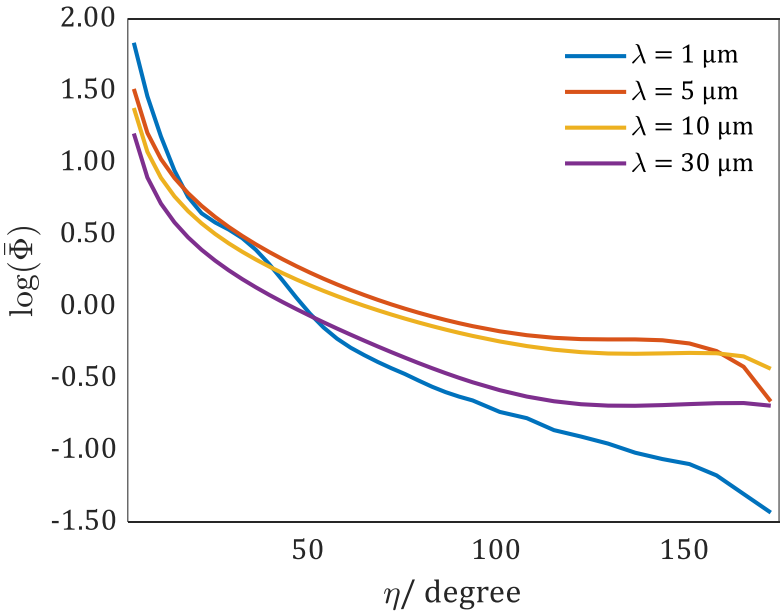

Once the extinction, scattering and absorption coefficients and the phase function of the medium are defined, the *RTE* could be solved. However, the strong forward scattering of the phase function makes the numerical implementation challenging. In order to overcome these computational issues, the so-called "isotropic scaling" method is generally employed. This

procedure involves transforming an anisotropic scattering problem into an equivalent isotropic problem through scaling transformation parameters (Kamdem & Baillis, 2005). To achieve this, the phase function is expressed in terms of isotropic and forward scattering components as (Stamnes et al., 2017):

$$\Phi_\lambda(\Omega_i,\Omega) = (1-g) + 2g\delta(\Omega_i,\Omega) \tag{2.19}$$

Where δ is the Dirac delta function and g is known as the asymmetry factor and is defined as

$$g = \frac{1}{4\pi}\int_{\Omega=0}^{4\pi}\Phi_\lambda(\Omega_i,\Omega)\cos\theta d\,\Omega_i \tag{2.20}$$

Considering Figure 1-4, $d\Omega_i = dA_n/r^2 = rd\theta r\sin\theta d\phi/r^2 = 2\pi\sin\theta d\theta$, the asymmetry factor can be expressed as:

$$g_\lambda = \frac{1}{2}\int_0^{\pi}\Phi_\lambda(\Omega_i,\Omega)\cos\theta\sin\theta d\theta \tag{2.21}$$

Replacing equations (2.19) and (2.21) in (1.6) leads to

$$-\cos\theta\frac{\partial I_\lambda(x,\theta)}{d\tau^*} = -(1-\varpi_\lambda^*)I_{\lambda b}(x) + I_\lambda(x,\theta) - \frac{1}{4\pi}\int_{\Omega_{i=0}}^{4\pi} I_\lambda(x,\Omega_i)\varpi_\lambda^*\,d\Omega_i \tag{2.22}$$

Which is equivalent to the RTE for isotropic case ($\Phi_\lambda = 1$). This formulation is also known as the transport approximation and was developed initially in neutron diffusion theory (Dombrovskii, 1996). The scaling parameters in equation (2.22) are defined as following:

$$\varpi_\lambda^* = \frac{\varpi_\lambda(1-g_\lambda)}{1-\varpi_\lambda g_\lambda} \tag{2.23}$$

$$\beta_\lambda^* = \beta_\lambda(1-\varpi_\lambda g_\lambda) \tag{2.24}$$

$$\tau^* = \tau(1-\varpi_\lambda g_\lambda) \tag{2.25}$$

Following a similar approach, Lee and Cunnington proposed a modified extinction coefficient $\bar{\beta}_\lambda$ based on an asymmetry scattering factor G_λ (Cunnington et al., 1997; Lee & Cunnington, 1998b, 1998a):

$$\bar{\beta}_\lambda = \beta_\lambda(1 - G_\lambda) \tag{2.26}$$

Where G_λ accounts for the scattered fraction of radiation produced by incident radiation in the heat flow direction, and is calculated from equations (2.27) and (2.28).

$$G_\lambda = \frac{1}{\beta_\lambda}\int_0^1 \int_{-1}^1 \sigma_{s,\lambda}\bar{\Phi}_\lambda(\mu_i, \mu_s)\mu_i d\mu_i d\mu_s \tag{2.27}$$

$$\sigma_{s,\lambda}\bar{\Phi}_\lambda(\mu_i, \mu_s) = \frac{1}{2\pi}\int_0^{2\pi} \sigma_{s,\lambda}\bar{\Phi}_\lambda(\eta) d\omega_i \tag{2.28}$$

As pointed out by Lee (Lee, 1988b), for radiation heat transfer applications it is more convenient to directly compute the product of the scattering coefficient and the phase function by combining equations (2.14), (2.17) and (2.18):

$$\sigma_{s,\lambda}\bar{\Phi}_\lambda(\eta) = \int_0^\infty \int_0^{\pi/2} \frac{i_\lambda(r, \theta, \eta)}{\sin\theta\cos\phi} N(r) d\phi dr \tag{2.29}$$

Alternative scaling procedures for fibrous insulation have been proposed by Cherepanov et al (Cherepanov et al., 2016; Cherepanov & Alifanov, 2017), Marschall and Milos (Marschall & Milos, 1997) and Kamdem and Baillis (Kamdem & Baillis, 2005, 2010). In section 3, the performance of these methods in accounting for anisotropy will be discussed in the context of fibrous insulation.

2.3 Optical properties

To calculate the properties presented in sections 2.1 and 2.2 besides the distribution of number of fibers, size and orientation, it is necessary to know the complex index of refraction and its temperature and wavelength dependence.

The complex index of refraction represents how a particle interacts with an electromagnetic wave through a medium and is defined as $\bar{n} = n - ik$. The real part, known as refractive index, quantifies the degree of bending or refraction of a wave in a medium. The complex part, known as absorption index, represents the attenuation of the wave due to absorption and scattering. For electric insulation materials, typically used in thermal insulation, the refraction index is partially explained by fundamental lattice vibration (one phonon) and electronic transitions, while the index of absorption (complex part of the index of refraction) requires additionally, a higher order phonon process (multiphonon) (Thomas, 1991).

2.3.1 Refractive index

The dependence of refractive index on wavelength and temperature can be explained by changes in electric susceptibility using the oscillator model (Rolt, 2020):

$$n^2(\nu, T) = 1 + \sum_i \frac{\Delta\epsilon_i(T)\nu_i^2(T)}{\nu_i^2(T) - \nu^2} \tag{2.30}$$

Where ν is the wavenumber and ν_i and $\Delta\epsilon_i$ are terms related to each vibrational frecuency of the material. This expresion is known as the Sellmeier equation and it is valid in the transparency region. The temperature dependence of ν_i and $\Delta\epsilon_i$ is given by (Thomas, 2006):

$$\nu_i(T) = \nu_i(T_0) + a1_i(T - T_0) + a2_i(T - T_0)^2 \tag{2.31}$$

$$\Delta\epsilon_i(T) = \Delta\epsilon_i(T_0) + b1_i(T - T_0) + b2_i(T - T_0)^2 \tag{2.32}$$

The parameters of the model for some refractory ceramic materials used for high temperature insulation are presented in Table 2-1.

Table 2-1: Parameters for oscillator model (Thomas, 2006).

Material	Mode	ν_i/ cm^{-1}	$\Delta\epsilon_i$	$a1_i$/ cm^{-1}/K	$b1_i$/ K^{-1}
SiO_2	1	394	0.33	0	0
	2	450	0.82	0	0
	3	697	2.00E-02	0	0
	4	797	0.11	0	0
	5	1072	0.67	0	0
	6	1163	1.00E-02	0	0
	7	1227	9.40E-03	0	0
	8	128	6.00E-04	0	0
	9	84034	0.176	0	0
	10	94340	0.518	0	0
	11	166666	0.663	0	0
Al_2O_3	1	384	0.33	-6.30E-03	7.16E-05
	2	439	2.77	-7.20E-03	3.36E-04
	3	568.1	2.99	-1.10E-02	2.03E-04
	4	633	0.145	-1.40E-02	3.03E-04
	5	805.9	1.85E-02	-1.90E-02	1.65E-04
	6	83805.3	0.65	0	3.40E-05
	7	137621.4	1.43	0	0
Y_2O_3: ZrO_2	1	411	9.45	0	0
	2	59974	2.12	0	0
	3	159890	1.35	0	0

Thomas et. al compared the oscillator and multiphonon models with refractive index data of alumina from several authors between 250 K and 2000 K. It was found that the model is not satisfactory for an accurate representation of the data, and additional corrections are needed (Thomas et al., 1998). Similarly, the temperature dependence of silica and yttria-zirconia

materials is not appropriately described by the oscillator model, as their temperature coefficients are zero, which contradicts the experimental evidence (Wood & Nassau, 1982; Wray & Neu, 1969). Notwithstanding the above, the oscillator model has a functional form that can be accurately fitted to experimental data for most of cases in a wide range of temperatures (Ghosh, 1994, 1997; Ghosh et al., 1994; Kim & Lines, 1993; Leviton & Frey, 2006; Matsuoka et al., 1991; Tan & Arndt, 2001).

2.3.2 Absorption index

The absorption coefficient is accurately described by the multiphonon theory. A multiphonon process can be represented using the Morse interatomic potential to solve the steady-state Schrödinger equation. The model to calculate the absorption coefficient is represented by equations (2.33) to (2.41) as shown by Thomas et al.(Thomas, 2006; Thomas & Joseph, 1988).

$$\kappa(\nu,T) = K\tanh\left(\frac{hc\nu}{2k_BT}\right)\sum_{n=1}^{m_{max}}\frac{\rho_\nu(\nu)+\rho_\nu(-\nu)}{n^2Q'(T)}\sum_{m=0}^{m_{max}-n}\frac{(m+n)!}{m!}\frac{\exp\left(-\frac{hc\nu M}{k_BTN}\right)}{j'^{(n-1)}} \tag{2.33}$$

$$J = \frac{4D_0}{\hbar\omega_0} \tag{2.34}$$

$$m_{max} \leq \frac{1}{2}(J-1) \tag{2.35}$$

$$M = m\left(1-\frac{1}{J}\right)-\frac{m^2}{J} \tag{2.36}$$

$$Q'(T) = \sum_{m=0}^{m_{max}}\exp\left(-\frac{hc\nu M}{k_BTN}\right) \tag{2.37}$$

$$j'(\nu) = \frac{2D_0 n}{hc\nu}\left[1 + \sqrt{1 - \frac{hc\nu(n+1)}{nD_0}}\right] \tag{2.38}$$

$$\rho_n(\nu) = \frac{1}{\sigma'_n\sqrt{2\pi}}\left[1 - \frac{\alpha_3}{\sqrt{n}}(3x - x^3)\right]\exp\left(-\frac{x^2}{2}\right) \tag{2.39}$$

$$x = \frac{\nu - n\alpha_1\nu_{max}}{\sigma'_n} \tag{2.40}$$

$$\sigma'_n = \alpha_2\nu_{max}\sqrt{n} \tag{2.41}$$

Where κ is the absorption coeffcient, ν is the wavenumber, h is the Planck Constant, c is the velocity of light in vacuum, k_B is the Boltzman constant. The other parameters of the model are presented in Table 2-2 for some refractory ceramic materials used for high temperature insulation.

Table 2-2: Parameters for multiphonon absorption model (Thomas, 2006).

Parameter	Al_2O_3	Y_2O_3	Y_2O_3: ZrO_2
α_1	0.5370		
α_2	0.1530		
α_3	0.0520		
ν_{max}/ cm^{-1}	914	620	668
D_0/ cm^{-1}	14000	12000	9700
K/cm^{-2}	1.463E7	2.250E7	6.000E7

The absorption index k is related to the absorption coefficient through equation (2.42)

$$\kappa = \frac{4\pi k}{\lambda} \tag{2.42}$$

For the case of alumina, the model was compared with measurements from Thomas (Thomas et al., 1988) and reported data from Palik and Dobrovinskaya (Dobrovinskaya et al., 2009; Palik, 1998) as shown in Figure 2-9, where the vertical bars represents the estimated uncertainty.

Figure 2-9: Comparison of Multiphonon model with measurement at several wavelengths.

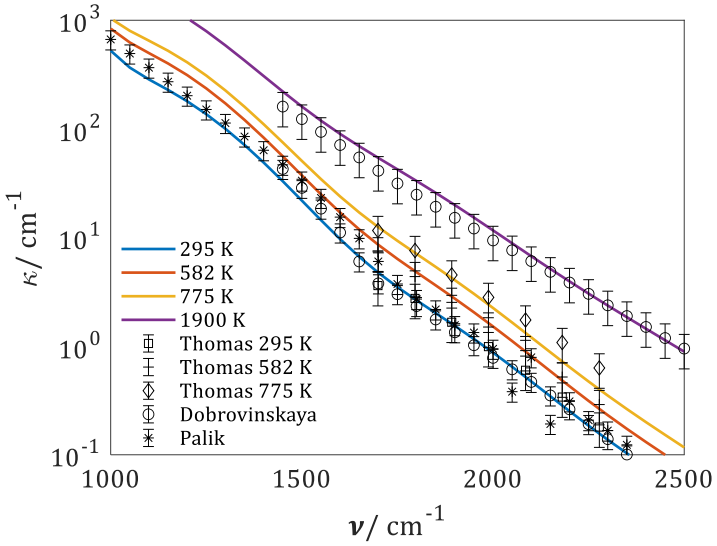

Figure 2-10 shows the comparison of the model with the data reported by Billard et al.(Billard et al., 1976) , Deutsch et al. (Deutsch, 1973) and Thomas et al.(Thomas et al., 1988)

Figure 2-10: Comparison of Multiphonon model with measurement at several temperatures.

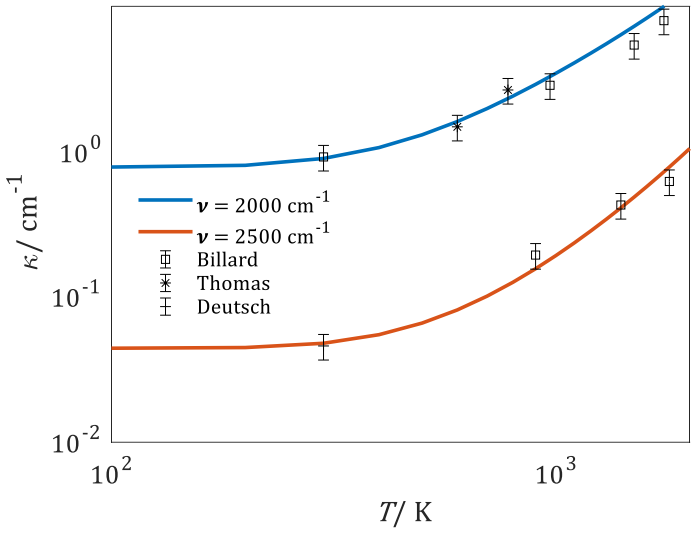

Except for two data points from Palik at room temperature and wavenumbers of 2150 cm^{-1} and 2050 cm^{-1}, as well as one point at 1500 K and a wavenumber of 2000 cm^{-1}, the model predicts data within an uncertainty of 35%. Therefore, it proves to be useful for interpolation at various wavelengths and temperatures.

3. Approximate solution of the *RTE*

The *RTE* depends nonlinearly on temperature, wavelength, position and direction, therefore, only under very special circumstances analytical solutions can be found. The simplest approach is the diffusion approximation, which allows to express radiation as a conduction term. This fact was used by several authors to present closed form analytical solutions of the energy balance equations. The main limitation is that these models require the experimental determination of a parameter, that combines several properties, which will vary with the material, bulk density, and fiber size distribution (Tong & Tien, 1983). Given the formulation of a single parameter, effects such as fiber size and optical properties are not accounted individually, then the conclusions are restricted primarily to the individual insulation tested. This approach is usually designated as empirical method.

It was not until Larkin and Churchill laid the foundation for modeling radiative transfer in fibrous media that more elaborate models emerged. They described the complexity of coupled radiation and conduction modeling in porous insulation and demonstrated that radiative heat transfer can be predicted using electromagnetic wave theory and optical properties (Larkin & Churchill, 1959a, 1959b). This approach allows to study the theoretical effects of fiber size and optical properties on fibrous insulation. Since the agreement with measurements was mainly qualitative, measurements of the materials are still required, but individual contributions can be accounted for separately. This approach will be designated as semi-empirical, given that is based closely in theoretical basis.

Given the improvement of computational capabilities and theoretical considerations, nowadays it is possible to quantify with acceptable accuracy the radiation heat transfer in fibrous insulation from the rigorous solution of the Maxwell-Equation, the *RTE*, and the energy conservation equation. This approach will be called predictive in the context of this research.

In this section, the main approximations used for modelling heat transfer in fibrous insulation are presented. For each approach, the main assumptions are highlighted, and the relevant studies for fibrous insulation are analyzed, considering whether they are predictive or semi-empirical methods.

3.1 Diffusion approximation

For an optically thick medium ($\tau \gg 1$) with isotropic intensity, equations (1.4) and (1.6) reduce to (Howell et al., 2020):

$$q_R = -\frac{16\sigma T^3}{3\beta_R}\frac{\partial T}{\partial x} \tag{3.1}$$

where σ is the Steffan-Boltzman constant and β_R is the extinction coefficient averaged over all wavelengths, which is known as the Rosseland mean and is given by equations (3.2) and (3.3) (Howell et al., 2020):

$$\frac{1}{\beta_R} = \frac{\pi}{2}\frac{C_1 C_2}{\sigma T^5}\int_0^\infty \left(\frac{1}{\beta_\lambda}\right)\left(\frac{\exp\left(C_2/\lambda T\right)}{\lambda^6(\exp(C_2/\lambda T)-1)^2}\right)d\lambda \tag{3.2}$$

$$\beta_\lambda = \sigma_{s,\lambda} + \kappa_\lambda \tag{3.3}$$

It is important to note that the Rosseland mean is valid for high optical thicknesses, such as those found in semitransparent materials like Al_2O_3 or SiO_2, and should be avoided when boundary effects are significant, especially under transient conditions (Modest & Mazumder, 2021). Equation (3.1) has a simple form and is suitable to express the coupled conduction and radiation as an overall thermal conductivity term. From 1950's several researchers used empirical methods based on this approximation to quantify the heat transfer in fibrous insulation used in building applications. A comprehensive review was presented by Tong and Tien (Tong & Tien, 1980).

At room and moderate temperatures, several authors have extensively used the diffusion approximation in conjunction with semi-empirical methods to determine the optical properties and radiative thermal conductivity of various fibrous insulations, including polymeric synthetic fibers (McKay et al., 1984; Yang et al., 2016), ceramic fibers (Zuev & Prosuntsov, 2014), recycled textile fiber (Tilioua et al., 2018) and mineral wools (Veiseh et al., 2009). In general, the results are very good when densities are low. Fractal theory has been also proposed to quantify and optimize the radiation and conduction in fibrous materials at room temperature (Song & Yu, 2012; Xiao et al., 2017). Song and Yu evaluated a model based on the diffusion approximation along with a box-counting method on fibers with diameters ranging from 9 μm to 21 μm. The results were compared with effective thermal conductivity measurements and reported formulations, demonstrating good agreement(Song & Yu, 2012).

At high temperature, most of the fibrous insulation are based on ceramic fibers. Table 3-1 shows chronologically some relevant studies carried on using semi-empirical methods based on diffusion approximation and steady state measurements.

Table 3-1: Results from semi-empirical methods based on diffusion approximation and steady state measurements.

Material	Density / kg m^{-3}	Fiber diameter / µm	Temperature / K	Deviation / %	Reference
SiO_2 Al_2O_3	34-128	2.2	320-1270	10	(Kamiuto et al., 1982)
SiO_2 Al_2O_3 (Kaowool[1])	190	2.6-5.1	500-1100	30	(Kamiuto, 1991)
SiO_2 Al_2O_3	128	1 - 9	300-973	14.7	(Zhao, Zhang, & He, 2009)
SiO_2 Al_2O_3	128	1 - 9	300-973	9.8	(Zhao, Zhang, & Du, 2009)
Al_2O_3 (Saffil[2])	24 -144	4.5	290-1360	6.3	(Daryabeigi, 2010; Daryabeigi et al., 2010)
Al_2O_3 (*APA*[3])	107	4.5	290-1100	6.4	(Daryabeigi et al., 2010)
Y_2O_3 ZrO_2 (ZYF[4])	267	6.0	290-1360	<10	(Daryabeigi et al., 2010)
Al_2O_3 (OFI[5])	202	-	290-1360	<10	
SiO_2 Al_2O_3 (Rigid insulation)	130-260	-	300-1360	11	(Daryabeigi et al., 2013)
SiO_2 TZM-23M	392	9	300-1373	~10	(Mironov, Gaidenko, et al., 2021)
SiO_2 TZMK-10M	139	1	300-1373	~10	

Kamiuto et al. used the effective thermal conductivity measurements to determine the extinction coefficient and a parameter that accounts for the tortuosity and heat paths for solid conduction on an aluminosilicate insulation for porosities ranging from 0.93 to 0.97 and temperature from 320 K to 1270 K (Kamiuto et al., 1982). The model was also tested on a

[1] Morgan Thermal Ceramics
[2] Thermal Ceramics Inc
[3] Zircar Ceramics Inc
[4] Zircar Zirconia Inc
[5] S. D. Miller & Associates Research Foundation/CDP

commercial insulation sample with 47.3 % Al_2O_3 and 52.3 % SiO_2 resulting in an accuracy of 30 % (Kamiuto, 1991).

Petrov calculated the transient response in the silica-based fibrous insulation used in Space Shuttle between 300 K and 1500 K (Petrov, 1997). The results agree well with the data reported in (Williams & Curry, 1977). A similar approach was evaluated by Zverev et al. on fibrous quartz insulation, and demonstrated good accuracy for fire protection applications (Zverev et al., 2008).

Zhang et al. used spectral transmittance measurements in the wavelength range of 2.5 μm to 25 μm to estimate the extinction coefficient and the Rosseland mean of a high-alumina fibrous insulation with a density of 128 kg m^{-3} and fiber diameters ranging from 1 μm to 9 μm (Zhang et al., 2007). The estimated radiative properties were used, along with the diffusion approximation, to compute the total heat flow including solid conduction. The calculations were compared with measurements of effective thermal conductivity at pressures ranging from 10^{-2} Pa to 10^{-5} Pa and temperatures ranging from 300 K to 973 K, resultin(S. Zhao, Zhang, & He, 2009)7 %(Zhao, Zhang, & He, 2009)

Daryabeigi et al. used the diffusion approximation along with effective thermal conductivity data to determine the specific extinction coefficient of alumina, silica, yttria-stabilized zirconia and *OFI* fibrous insulation systems at high temperatures. Once the temperature-dependent specific extinction coefficient is obtained, it is used with equations (1.1) and (3.1) to determine the effective thermal conductivity assuming a solid conduction model (Daryabeigi, 2010; Daryabeigi et al., 2010, 2013). For all the insulation types modeled, the results matched test data within the experimental uncertainty range.

Lumley et al. reviewed the use of the diffusion approximation on several alumina and silica-based insulators (including the samples from Daryabeigi and Zhao included in Table 3-1) considering the solid conduction and convection. In general, at high temperatures, diffusion seems to be appropriate to describe the heat transfer along with semi-empirical methods (Lumley et al., 2015).

In order to avoid the use of fitting parameters, Caps et al. proposed a predictive model that accounts for anisotropy considering the transport approximation described in section 2.2. The Rosseland mean was theoretically calculated using equation (3.2) but instead of β_λ, the scaled extinction coefficient defined in equation (2.24) was used. The model was evaluated between 400 K and 700 K using a glass-fiber insulation with fiber diameters ranging from 0.5 μm to 0.7 μm, density of 280 kg m^{-3} and porosity of 0.9. Even though solid conduction was assumed temperature independent, fiber orientation was not accounted for explicitly and the effect of the fiber diameter distribution was not included in the formulation (which is acceptable given the narrow range of fiber diameters), the results are in very good agreement with measurements from *GHPA* (Guarded hot plate apparatus), and reflectance and transmittance measurements (Caps et al., 1984). Mathes and Blumenberg extended the formulation of Caps accounting for the fiber orientation in randomly oriented medium (Mathes et al., 1990). A further validation of this model was presented by Dombrovsky (Dombrovsky, 1996) using the data reported in (Nicolau et al., 1994) for a silica-based insulation. Mironov et al. used a similar approach to evaluate two types of silica-based insulation for temperatures ranging from 300 K to 1373 K finding deviation of the order of 10 % (Mironov, Gaidenko, et al., 2021). An analogous model used in the design of *TPS* was validated by Alifanov et al. using thermal measurements under unsteady state conditions at ~ 0.01 Pa and temperatures ranging from 297 K to 1273 K (Alifanov et al., 2023). Another scaling procedure used with the diffusion approximation was presented by Marschall and Milos based on an equivalent cartesian fiber network (Marschall & Milos, 1997). The procedure was evaluated with exact solutions available for silica and alumina insulations showing that the scaling procedure has an intrinsic average error less than 5 %.

Lee and Cunnington proposed the use of an asymmetry scattering factor to correct the effect of anisotropy on the diffusion approximation (as shown in section 2.2) (Cunnington et al., 1997; Lee & Cunnington, 1998b, 1998a). Similarly to Caps et al., the Rosseland mean was calculated using the modified extinction coefficient defined in equation (2.26). The method was evaluated with certified values of the Standard Reference Material (*SRM*) 1450C produced by *NIST* (Zarr, 1997). The maximum error found was 5 % between 280 K and 340 K and densities between 150 kg m^{-3} and 165 kg m^{-3} (Carvajal et al., 2019). At higher temperatures, the model was evaluated using the well characterized LI900 insulation (a bonded silica-based insulation (Banas & Cunnington, 1974)) between 400 K and 1366 K (Lee & Cunnington, 1998b, 2000). In

general, the predictions are within the experimental uncertainty, however, the error seems to increase with increasing thermal conductivity. Daryabeigi et al. validated the model on an unbounded silica insulation with densities ranging from 48.6 kg m^{-3} to 95.6 kg m^{-3} and temperatures from 360 K to 1360 K from measurements of effective thermal conductivity by means of a Heat Flow Meter Apparatus (*HFMA*). The predictions and measurements had a maximum deviation of 6.2 % while the uncertainty of the model ranged from 8 % to 12 % (Daryabeigi et al., 2008, 2010).

Recently, Curran and Porter employed the diffusion approximation, along with tomographic imaging, to model soda lime glass-based insulation with shot particles composition ranging from 25 % to 35 %, fiber diameters between 1 μm and 25 μm, and temperatures ranging from 300 K to 1673 K. The model accurately predicts the effective thermal conductivity when heat transfer is perpendicular to the layers of fibers (Curran & Porter, 2020).

3.2 Milne-Eddington approximation

For isotropic scattering and considering the first and second moments of the radiant intensity, equations (1.4) and (1.6) reduce to (Howell et al., 2020):

$$\frac{\partial^2 q_R}{\partial x^2} - 3\kappa_\lambda \beta_\lambda q_R = 4\pi\kappa_\lambda \frac{dI_b}{dx} \tag{3.4}$$

Marschall et al. (Marschall et al., 2001) used a semiempirical method to estimate the thermal response of the LI900 insulation by employing a scaling technique to account for anisotropy. As before, the extinction coefficient in equation (3.4) was replaced by the scaled version. The Milne Eddington approximation was used to compute the radiative flux and the transient temperature measurements reported in (Williams & Curry, 1992).

Zhang et al., as in the case of diffusion model described previously (Zhang et al., 2007; Zhao, Zhang, & He, 2009), used spectral transmittance measurements to estimate the extinction coefficient and the Rosseland mean. As above, they employed the transport approximation to

account for anisotropy. These estimated properties were then used in conjunction with the Milne-Eddington approximation to compute the anisotropy factor, scattering albedo, and solid-gas conduction through an inverse technique. The transient response and the effective thermal conductivity estimated by the model were compared with measurements, resulting in an average error of 17.6 %(Zhao, Zhang, Du, et al., 2009).

3.3 Two-flux approximation

For isotropic scattering and considering the radiant intensity composed of forward and backward directions, equations (1.4) and (1.6) reduce to (Modest & Mazumder, 2021):

$$\frac{\partial^2 q_R}{\partial x^2} - 4\kappa_\lambda \beta_\lambda q_R = 4\pi\kappa_\lambda \frac{dI_b}{dx} \tag{3.5}$$

Equation (3.5) is quite similar to the Milne-Eddington model since both have similar assumptions. The difference is a factor of $4/3$ in the radiative heat flux. Larkin and Churchill used this model to estimate the radiative heat transfer in commercial silica-based insulation between 366 K and 700 K (Larkin & Churchill, 1959a). The radiative properties were approximated using transmission measurements in a blackbody source and a thermopile detector. The main conclusions highlight that there exists an optimal fiber size that minimize the radiative heat transfer and the predominant influence of the scattering in fibrous insulation.

Posteriorly, Tong and Tien developed a radiation model considering this approximation and linear anisotropic scattering (Tong et al., 1983; Tong & Tien, 1980, 1983). They evaluated the validity of the model with measurements of the extinction coefficient and the heat flux in commercial lightweight fibrous insulation by means of transmission and *GHPA* measurements under vacuum. As in the work of Larkin and Churchill, just qualitative agreement was obtained. The error found was about 20 % to 40 % and it was attributed to the nongray behavior of the fibers, inhomogeneity of the tested insulation and the miscalculation of the orientation of the fibers. Another important limitation of this model was the fact that the forward and backward

directions in the two-flux model were inconsistent with the fiber orientation as pointed out by Lee (Lee, 1986). Despite that, the model was able to highlight the importance of radiation in relation to the heat transfer in lightweight fibrous insulation even at room temperatures (Tong et al., 1985).

Daryabeigi used the two-flux method to estimate the specific extinction coefficient and the scattering albedo based on effective thermal conductivity measurements in an alumina-based insulation for re-entry aerodynamic heating conditions. The resulting model was used to optimize the design of high temperature multilayer insulation (Daryabeigi, 2001).

Zhao et al. employed the same inverse analysis as described in the case of diffusion (Zhang et al., 2007; Zhao, Zhang, & He, 2009) but replaced it with the two-flux approximation. Since the only variation was the radiation model, the results are useful for model comparison. The resulting error was 13.5 % (Zhang et al., 2008). This represents a reduction in error of 1.2 % compared to the diffusion approximation.

Mathews et al. developed an inverse method based on a modified formulation of the two-flux approximation that considers non-isotropic scattering as formulated by Domoto and Wang (Domoto & Wang, 1974). This method was used to estimate the radiative properties of a zirconia-based insulator under transient conditions between 350 K and 1600 K (Matthews et al., 1984). The estimations of the model are in agreement with the data reported in the literature. A similar approach was implemented by Daryabeigi for modelling radiation heat transfer in high density alumina fibrous insulation between 300 K and 1300 K (Daryabeigi, 2002, 2003) and multilayer insulations with alumina spacers (Daryabeigi et al., 2007). The relevant radiative properties were evaluated from measurement of effective thermal conductivity. The maximum difference found was 1.6 % for alumina insulation and 12.7 % for multilayer insulation.

Ji et al. used the simplified the model proposed by Larkin and Churchill to model the radiative heat transfer in ceramic fiberboard samples, which mainly contained alumina and silica fibers (50 % SiO_2-48 % Al_2O_3) with an average fiber diameter of 4.4 μm. The model, which also considers conduction through a random structure model, was compared with *GHPA* measurements at temperatures ranging from 288 K to 358 K and densities ranging from 30 kg

m^{-3} to 211 kg m^{-3}, resulting in an error of approximately 2 % (Ji e(Hussain & Tao, 2018)n and Tao (Hussain & Tao, 2018) evaluated a model for effective thermal conductivity based on the two-flux approximation for radiation, using the lattice Boltzmann method and the data reported in (Ji et al., 2014). They found a maximum error of 10 %.

3.4 Discrete ordinated method

The main limitation of the previous approximations is related to the assumption of isotropic scattering. In fact, in fibrous insulation a high degree of anisotropy is excepted due to the random orientation and asymmetry of the fibers. One of the most popular approximations to include this effect is the method of discrete ordinates, where the integral in equation (1.5) is replaced by weighted sums (Howell et al., 2020):

$$-\frac{\partial I_\lambda(S,\Omega)}{dS} = \kappa_\lambda I_{\lambda b}(S) - \beta_\lambda I_\lambda(S,\Omega) + \frac{1}{4\pi}\sum_{m'} w_{m'} I_{m'}(S)\,\sigma_{s,\lambda}\Phi_{m'm}(S) \tag{3.6}$$

Once the radiant intensity is determined for any given number of ordinate directions m, the radiative heat flux can be calculated from equation (1.4). Houston and Korpela used this method to estimate the coupled conduction-radiation heat transfer in silica based fibrous insulation with a mean diameter of 7.45 μm and a density of 8.82 kg m^{-3} (Houston & Korpela, 1982). Similarly as the transport approximation, the phase function was expressed using two terms, which leads to similar expression as (2.23), (2.24) and (2.25). This model was evaluated between 308.8 K and 392.7 K against measurement in a *GHPA* obtaining errors of about 4 %. Besides the *RTE* model, the difference with the work of Tong and Tien was the inclusion of the term $\cos\phi$ to account for the fiber orientation.

Yeh and Roux used measurements of reflectance and the discrete ordinates method to estimate the extinction and absorption coefficient of a commercial pink fiberglass with density of 10.9 kg m^{-3}, and mean diameter of 9 μm for wavelengths between 4 μm and 80 μm (Yeh & Roux, 1988).

Lee and Cunnington compared the measured reflectance and transmittance of bonded silica fiber insulations with values estimated by solving equation (3.6) (Cunnington & Lee, 1996)cidence(Cunnington & Lee, 1996). The model enables accurate prediction of the reflectance and transmittance peaks of the samples. Kurosaki and Yamada used a similar setup to the one presented above using an aluminosilicate-based insulation, but they included the effective fiber length in their estimation of the radiative properties. The reflected and most of the transmitted flux agreed well with the measurements (Kurosaki & Yamada, 1991).

Kamdem and Baillis evaluated three insulation samples composed mostly of SiO_2, with a fiber diameter of 1.85 μm, porosities greater than 98 %, and densities ranging from 11.25 kg m^{-3} to 50 kg m^{-3} at room temperature. The radiative properties were calculated using different scaling procedures, also called reduced models. The coupled conduction and radiation equations were solved using the discrete ordinates method. The results indicate that the reduced models are appropriate for modeling the effective thermal conductivity (Kamdem & Baillis, 2005, 2010) .

Zhao et al. applied the semi-empirical method to the sample described previously (Zhao, Zhang, Du, et al., 2009) using the transport approximation and the discrete ordinates method. In this case, the results were compared with measurements under both steady-state and transient conditions. The resulting average error was 3.1 % for transient conditions and 9.8 % for steady-state conditions (Zhao, Zhang, & Du, 2009)

Other approaches based on angular, space and spectral discretization have been proposed by Boulet et al. and Asllanaj et al. (Asllanaj et al., 2001, 2002; Boulet et al., 1993). The models predict the increasing curvature in the temperature profile as the radiation term becomes dominant, as well as the existence of a density and fiber diameter that minimize heat transfer. Although a quantitative comparison with experimental data is not explicitly presented, the models appear to agree well with data from *GHPA* measurements on a medium composed of silica fibers with a density of 10 kg m^{-3} and a fiber diameter of 7 μm. Asllanaj et al. extended their model to transient scenarios, obtaining results comparable with available test cases (Asllanaj et al., 2004, 2007). More recently, discrete ordinates method has been used to simulate 2D and 3D heat transfer in fibrous insulation (Arambakam, 2013; Arambakam et al., 2013, 2014; Mishra et al., 2011).

3.5 Other approaches

Yuen et al. proposed a model base on the zonal method to evaluate steady state and transient responses of the LI900 insulation at high temperatures (W. Yuen et al., 2003; W. W. Yuen & Cunnington, 2007). The predictions are within the experimental uncertainty; however, the error seems to increase with increasing temperature as in the modified diffusion approximation applied to the same material (Lee & Cunnington, 1998b, 2000).

Monte Carlo Ray Trace Method (*MCRT*) has been (Sacadura & Baillis, 2002)ysis (Sacadura & Baillis, 2002) or to predict directly radiative properties (Randrianalisoa et al., 2017) or heat fluxes (Veiseh & Hakkaki-Fard, 2009)

4. Validation of the model

The diffusion model presented in section 3.1, along with the radiative and optical properties models described in section 2, were solved for an alumina-based insulation selected to validate the model. This material was chosen due to its use at higher temperatures (compared with silica), the availability of properties and similar studies conducted on it.

In section 4.1, the morphological and optical characteristics of the material are presented. Section 4.2 shows the numerical method implemented and the solution of the model. Finally, the accuracy of the model is obtained by comparison with effective thermal conductivity measurements as shown in section 4.3.

4.1 Sample description

Alumina is a mineral with exceptional hardness, chemical and thermal stability, optical transparency, resistance to corrosion and oxidation and excellent thermal and electric conductivity properties. Its main drawback is the high brittleness. Alumina is prepared from bauxite, a sedimentary rock that contains several crystalline forms of aluminum hydroxide as Gibbsite, Bayerite, Diaspore, etc. (Figure 4-1), by high temperature treatment (Hudson et al., 2000).

Figure 4-1: Crystalline form of aluminum hydroxides. Adapted from (Hudson et al., 2000).

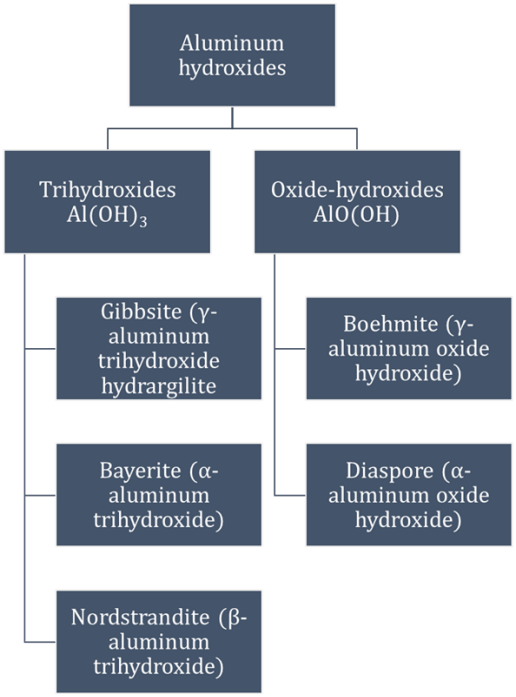

Under heating and ambient pressure, independently of the type of aluminum hydroxide, all crystalline forms are converted to α-Al_2O_3, also called corundum. It is the stable form at all temperatures and pressures until 78 GPa, as shown in Figure 4-2. In the single crystal form, corundum is also known as sapphire, which has a hexagonal closed-pack structure (Doremus, 2008). Silica is usually added to alumina as a reinforcement method and also to facilitate its processing into fibers and to increase its tensile strength (Seydibeyoglu et al., 2017).

Figure 4-2: Preparation of α-Al_2O_3. Adapted from (Hudson et al., 2000).

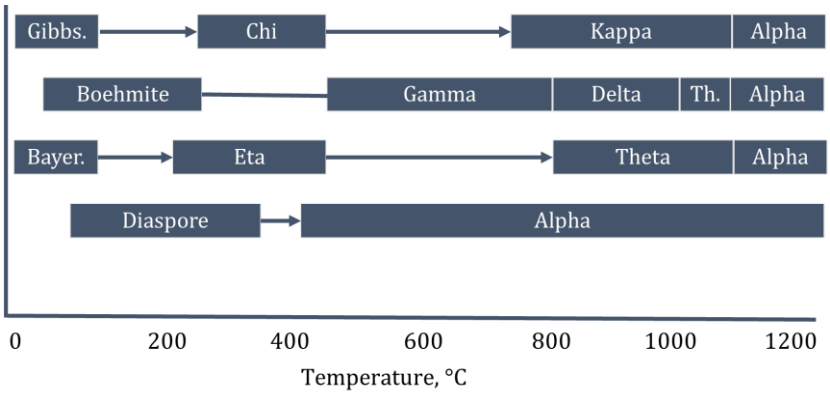

An alumina-based fibrous insulation was used to validate the model. The sample used was a commercially available alumina paper (*APA*™[6]) insulation built from polycrystalline alumina fibers, designed to operate at a maximum temperature of 1923 K. The sample has a nominal weight-based composition of 86% Al_2O_3, 10% SiO_2, and 4% other oxides. The measured density is 98.4 kg m^{-3}, and the density of the fiber base material at 298.15 K is 3200 kg m^{-3} (Bunsell. A, 2006), resulting in a fiber volume fraction of 0.0308. Some properties are presented in Table 4-1. The thermal stability of the sample was assessed by measuring the mass loss after a total of 40 hours of exposure at 1923 K, resulting in a total mass loss of 1.2%.

[6] Manufactured by Zircar Ceramics Inc

Table 4-1: Physical properties of *APA* sample (ZIRCAR Ceramics, 2020).

Nominal thickness/ mm	1.04
Weight, g m^{-2}	126
Nominal density, kg m^{-3}	120
Type of binder	None
Form	Semiflexible
Maximum temperature/ K	1923
Color	White

4.1.1 Fiber distribution

In order to estimate the distribution of number of fibers $N(r_i)$ with radius r_i, a series of scanning electron microscopy (*SEM*) images were taken at different positions of the *APA* sample. Four different areas designated as A2, A3, A4 and A5 were evaluated, each at magnifications of 50x, 100x and 1000x as shown in figures 4-3 and 4-4.

Figure 4-3: *SEM* of *APA* sample at magnification of 50x and 100x.

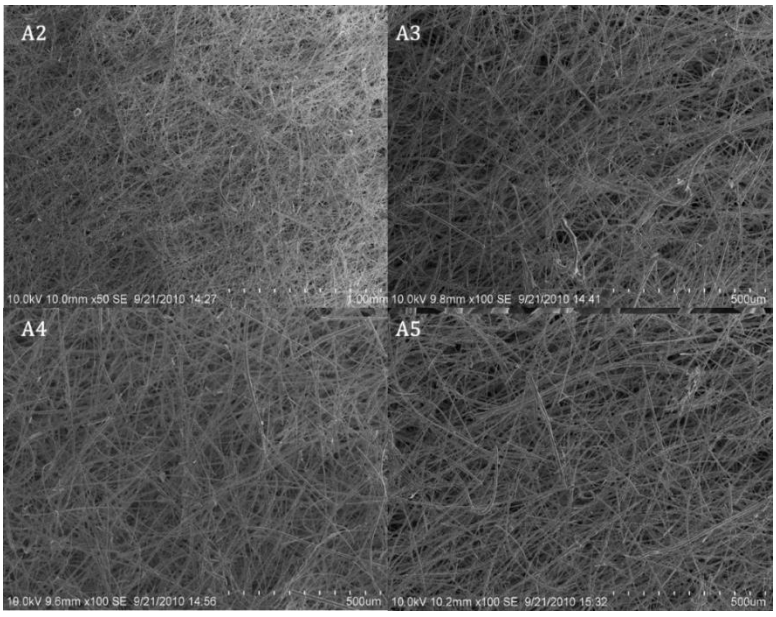

Figure 4-4: *SEM* of *APA* sample at magnification of 1000x.

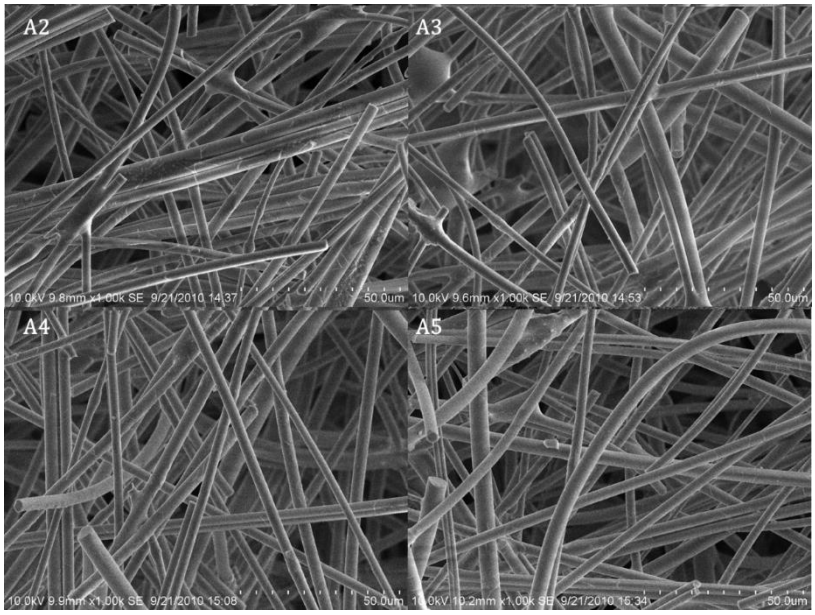

The *SEM* images reveal that there is not a preferred fiber orientation and the length of the fibers are several orders of magnitude greater than the fiber diameter, therefore, the randomly oriented infinite cylinder approximation is justifiable. As seen in Figure 4-4 the average distance between fibers is several times greater than the mean fiber diameter (3.2 μm), therefore the independent scattering criteria from Hottel can be applied(Hottel et al., 1970). In the same way, the size parameter ($\alpha = 2\pi r/\lambda$) for the wavelengths of interest ranges from 2 to 50 and considering the volume fraction of 0.0308, according to Figure 2-4 the independent scattering assumption for this case is verified.

The number of fiber distribution $N(r)$, can be conveniently expressed in terms of the fractional fiber volume $v(r)$ as:

$$v(r) = N(r)\pi r^2 L_f \tag{4.1}$$

Where L_f is the length of the fibers. The differential density of the sample can be expressed as:

$$d\rho_b = \rho_s N(r) dr \tag{4.2}$$

Where ρ_b is the density of the sample and ρ_s is the density of the parent material of the fibers. Combining equations (4.1) and (4.2), integrating and solving gives:

$$f = \int \frac{v(r)}{\pi r^2 L_f} dr \tag{4.3}$$

Where f is the fiber volume fraction and is estimated as the ratio ρ_b/ρ_s. The fractional fiber volume must be evaluated from the fiber size distribution and the length of the fibers. The process consists of building a histogram, as in typical fiber size distribution, but the relative frequency is replaced by the normalized length of the fiber. It is important to note that fiber breakage during the preparation of the sample will not affect the fiber distribution (Houston, 1980). To obtain the fractional fiber volume, the normalized volume is replaced by the normalized length. The fiber diameter distribution was estimated using the software ImageJ (Schneider et al., 2012) by counting 200 fibers of Figure 4-4. The details about the measurements are presented in Annex A. The resulting fiber diameter distribution and fractional fiber volume of the sample, are presented in figures 4-5 and 4-6, respectively.

Figure 4-5: Fiber diameter distribution for *APA.*

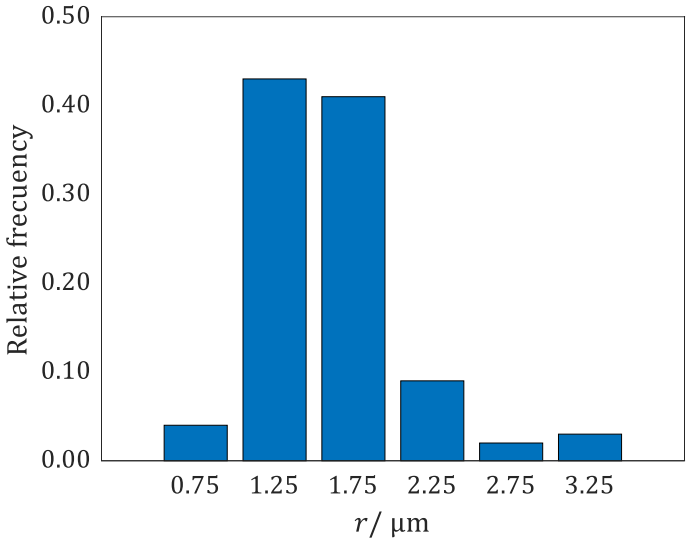

Figure 4-6: Fractional fiber volume for *APA.*

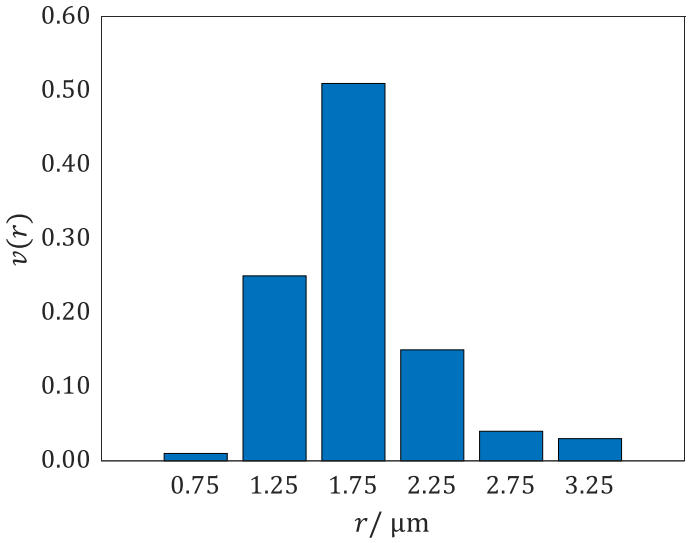

4.1.2 Optical properties

The complex refractive index of alumina is shown in Figures 4-7 and 4-8. The refractive index was obtained from the data reported by Dobrovinskaya (Dobrovinskaya et al., 2009). The absorptive index was also obtained from Dobrovinskaya's data, which covered wavelengths between 0.5 μm and 7 μm. For the remaining wavelengths, the absorptive index was estimated using the multiphonon model presented in section 2.3.2.

Figure 4-7: Wavelength and temperature dependence of real part of refractive index for alumina.

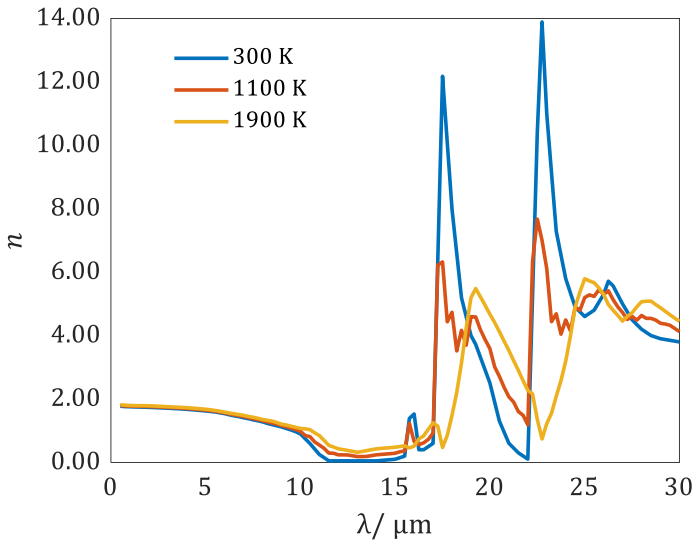

Figure 4-8: Wavelength and temperature dependence of complex part of refractive index for alumina.

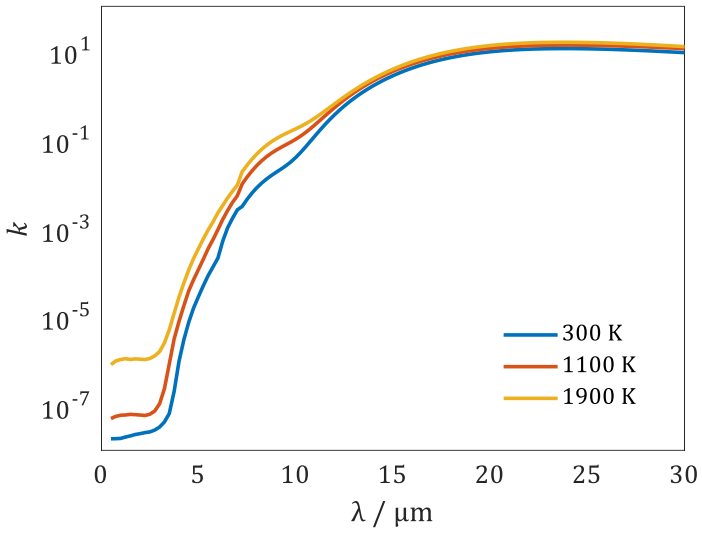

It is important to note that the refractive index was estimated assuming pure alumina, however, the refractive index is not expected to have a significant variation with chemical composition as pointed out in (Wang & Tien, 1983). The same assumption was made for the complex part of the refractive index. In this case, a significant variation is expected due to the presence of defects and impurities introduced during the fabrication process, which can affect the absorption coefficient by several orders of magnitude, even for materials with similar compositions(Daoût et al., 2023; Li et al., 2021).

4.2 Solution of the model

Given that the optical thickness of the *APA* sample is about 20 for a sample thickness of 25.4 mm (Daryabeigi et al., 2010), the diffusion model can be used. This approximation is preferred due to its simplicity and the comparable results it provides when compared to other models. The quantity determined experimentally is the effective (or apparent) thermal conductivity, which includes heat transfer by conduction, convection and radiation (Zarr, 2001). In order to

determine the error, the effective thermal conductivity predicted by the model $k_{eff,model}$ can be obtained by combining equations (1.1) and (3.1):

$$\frac{\partial}{\partial x}\left(k_{eff,model}\frac{\partial T}{\partial x}\right) = 0 \tag{4.4}$$

Where:

$$k_{eff,model} = k_r + k_c \tag{4.5}$$

$$k_r = \frac{16\sigma T^3}{3\beta_R} \tag{4.6}$$

k_r represents the thermal conductivity due to radiation and it will be calculated in section 4.2.1. k_c represent the thermal conductivity due to solid conduction and it will be calculated in section. 4.2.2 Tests used for validation were conducted in vacuum, so the gas conduction mode of heat transfer is negligible, and not considered here.

4.2.1 Radiation model

To calculate the radiative thermal conductivity, the Rosseland mean defined in equation (3.2) was calculated using the modified extinction coefficient $\bar{\beta}_\lambda$ calculated through equations (2.13), (2.26), (2.27), (2.28) and (2.29). This model includes anisotropy effects and has shown very good results in silica insulation (see section 3.1).

Considering that usually the fiber distribution is presented as a discrete fractional fiber volume function, equations (2.13) and (2.29) can be expressed as (Cunnington et al., 1998; Cunnington & Lee, 1996; Lee, 1986):

$$\beta_\lambda = \frac{f}{\pi}\sum_{i=1}^{N}\frac{v(r_i)}{r_i^2}\int_0^{\pi/2} C_{e,\lambda}\cos\phi\, d\phi \tag{4.7}$$

$$\sigma_{s\lambda}\bar{\Phi}_\lambda(\eta) = \frac{4f\lambda}{\pi^3}\sum_{i=1}^{N}\frac{v(r_i)}{r_i^2}\int_0^1 \frac{i(\eta,\phi)}{\sqrt{(1-\cos\eta)(1+\cos\eta-2\sin^2\phi)}}d(\sin\phi) \tag{4.8}$$

Given that radiation in a single cylinder is confined to a cone, the integration region in equation (4.8) must be limited to the incident angles defined in equations (4.9) and (4.10) (Lee, 1990).

$$\phi_{c,inf} = arccos\left(\sqrt{\frac{cos\,\eta+1}{2}}\right) \tag{4.9}$$

$$\phi_{c,sup} = \pi - \phi_{inf} \tag{4.10}$$

Where $\phi_c = |\pi/2 - \phi|$. The calculation procedure of the Rosseland mean is presented diagrammatically in Figure 4-9. The integrals were solved using the trapezoidal method. A sensitivity analysis for the number of discrete steps for each integral is presented in Annex B.

Figure 4-9: Flow chart for the calculation of the Rosseland mean in the Lee and Cunnington model.

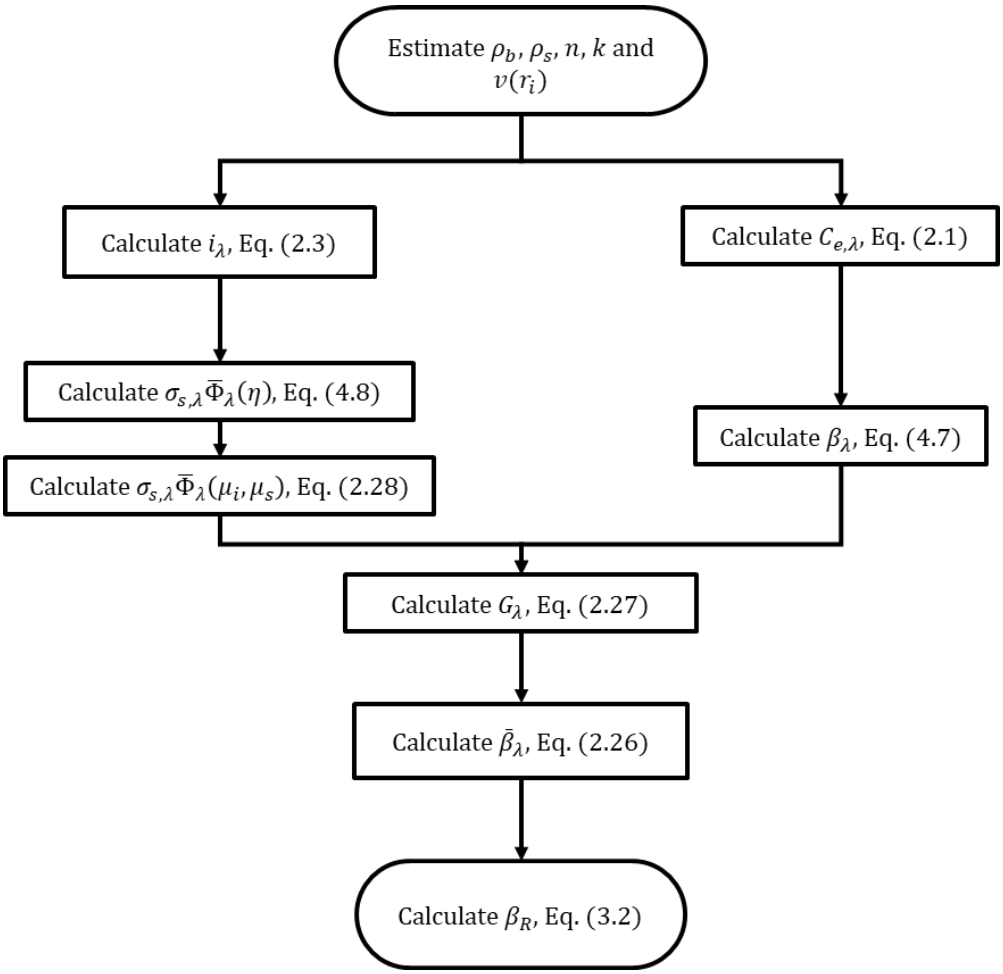

The grid for the estimation of the integrals is summarized in Table 4-2. These step sizes ensure that the variation is less than 3 % with each subsequent reduction. The modified extinction coefficient between 300 K and 1700 K calculated from equation (2.26) is presented in figures 4-10 and 4-11.

Table 4-2: Step size for the finite difference method.

Variable	Equation	Step size
ϕ	(4.7)	$\Delta\phi = \pi/20$
ϕ	(4.8)	$\Delta\phi = \pi/500$
ω_i	(2.28)	$\Delta\omega_i = \pi/100$
μ_i	(2.27)	$\Delta\mu_i = 0.1$
μ_s	(2.27)	$\Delta\mu_i = 0.02$

Figure 4-10: Roseland mean between 1000 K and 1700 K.

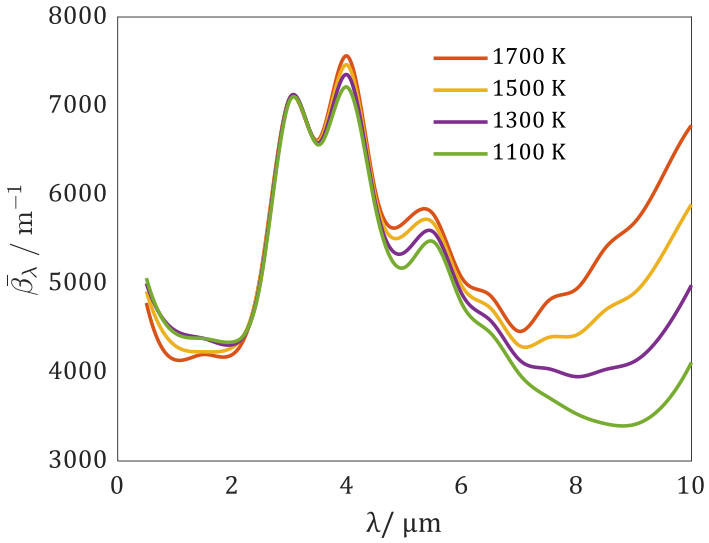

Figure 4-11: Roseland mean between 300 K and 900 K.

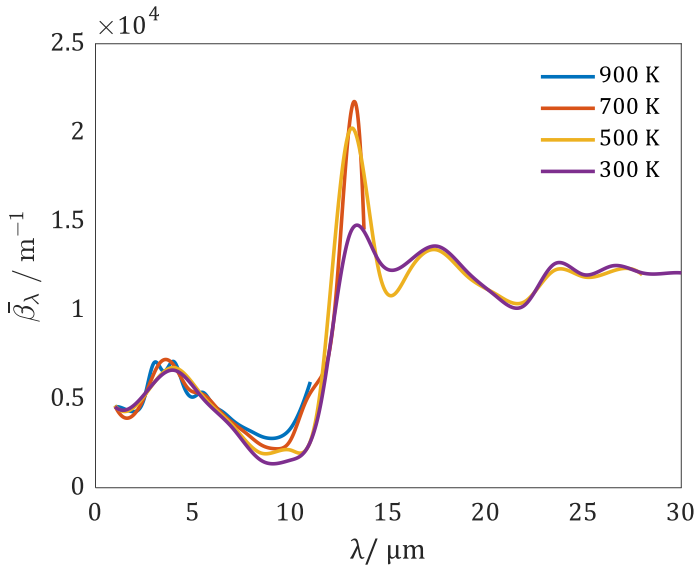

In the transparency region of alumina (0.5 μm – 6 μm), the modified extinction coefficient is slightly affected by temperature and shows a maximum value around 4 μm, as seen in Figure 4-10. This peak is due to scattering, given that the absorption index below this wavelength is negligible, as shown in Figure 4-8. At higher wavelengths, the temperature has a marked effect in the extinction coefficient, however this dependence vanishes beyond 15 μm, as seen in Figure 4-11.

The Rosseland mean calculated from equation (3.2) was integrated in a spectral range that accounts for about 90% of the blackbody emissive power at each temperature, considering the variation of the complex refractive index according to figures 4-7 and 4-8. The results are presented in Table 4-3.

Table 4-3: Rosseland mean.

T/ K	β_R/ m^{-1}	T/ K	β_R/ m^{-1}
300	3434.4	1100	5325.0
400	3739.1	1200	5251.6
500	4214.6	1300	5145.9
600	4752.4	1400	5026.2
700	5109.6	1500	4910.0
800	5274.7	1600	4812.3
900	5374.9	1700	4711.9
1000	5403.3	-	-

4.2.2 Conduction model

The conduction contribution was estimated according to the semi-empirical model presented in equation (1.10) based on cryogenic measurements. The scale parameter F was estimated from the thermal conductivity and density of the fiber parent material and the thermal conductivity of the *APA* sample measured at cryogenic temperatures in vacuum, where radiation, gas conduction, and convection contributions are reduced significantly (Daryabeigi et al., 2010).

At cryogenic temperatures, the thermal conductivity of insulation materials such as alumina, depends dramatically on impurities, given that the energy is transmitted by crystal lattice vibrations (phonons) (Tritt, 2006). The data reported for 92% and 96 % α-Al_2O_3 (Kita et al., 2015; Xie et al., 2011) show that that the deviation from pure alumina increases as the temperature decreases until the vicinity of 110 K. Unfortunately, there is no data reported at low temperatures for base materials with the specific composition of the *APA* sample. Considering the above, the recommended thermal conductivity data for 99.5% polycrystalline alumina reported by Touloukian et al. (Touloukian et al., 1971) were used, with the note that the values should be lower. The data may be represented using equation (4.11) as shown in

Figure 4-12. The uncertainty of the reported data is 6 % between 500 K to 1000 K and 10 % at other temperatures. In equation (4.11) k_s has units of W m^{-1} K^{-1} and T of K.

$$k_s(T) = -4.39873 + \frac{12832.79}{T} \tag{4.11}$$

Figure 4-12: Thermal conductivity of alumina.

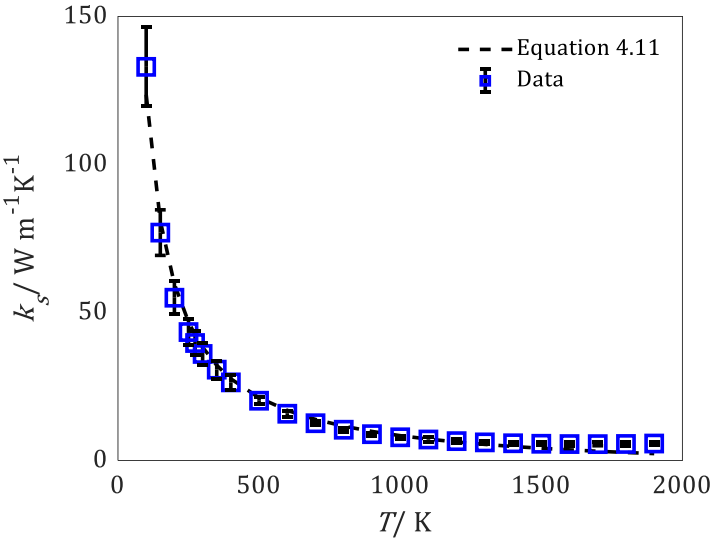

The thermal conductivity of the *APA* sample at cryogenic temperature and vacuum was estimated from previous measurements of thermal diffusivity α, density ρ_b and specific heat C_p, according to equation (4.12) (Incropera et al., 2006).

$$k_c = \rho_b C_p \alpha \tag{4.12}$$

Thermal diffusivity was measured using the step heat method, which is a modification of the standard laser flash method (ASTM E1461-13, 2022) useful in large heterogeneous materials (Bittle & Taylor, 1984). The method involves the constant application of a uniform heat flux to one face of an insulating disk-shaped sample and recording the associated temperature rise on the other face and halfway through the sample thickness. The thermal diffusivity can be

calculated from the transient temperature response, and then thermal conductivity can be calculated using equation 4.12 along with measured or known specific heat and density of sample (Vozár & Srámková, 1997). The measurements were performed by TPRL, Inc. at 0.005 torr using a 2-inch diameter electrical heating element as a heat source for temperatures below room temperature and a 60 W lamp at other temperatures. As pretreatment, the sample was dried for sufficient time in a vacuum chamber to remove moisture. Then the chamber was filled with N_2 gas at pressure of 0.005 torr. The relative expanded uncertainty with a coverage factor of 2 was estimated to be 8 % (Gembarovic et al., 2010; Gembarovic & Taylor, 2007). At high temperature the uncertainty increases due to radiation component. All measured quantities are directly traceable to *NIST* Standards. The results are presented in Table 4-4.

Table 4-4: Thermal diffusivity of *APA* at cryogenic temperatures and vacuum.

Temperature/ K	Thermal diffusivity/ $m^2 s^{-1}$
130	3.06E-08
180	2.57E-08
223	2.60E-08
273	2.98E-08
300	3.26E-08

Bulk density of the sample used in the thermal diffusivity measurements was determined from the geometry and mass of the sample, giving an estimate of 111.8 kg m^{-3}. The measurement of the thickness is especially challenging given the compressibility and heterogeneity of the material.

Specific heat was measured through a Differential Scanning Calorimeter (Perkin-Elmer Model DSC-2) based on (ASTM E1269-11, 2011) with sapphire as the reference material. All measured quantities are directly traceable to *NIST* Standards. The estimated uncertainty was 4%. The results are presented in Table 4-5.

Table 4-5: Specific heat of *APA* at cryogenic temperatures.

Temperature/ K	Specific heat/ J $kg^{-1}K^{-1}$
130	291
180	480
223	610
273	729
300	788
500	1040
700	1140
900	1210
1100	1243

The thermal conductivity at cryogenic temperatures and vacuum calculated from measurements of thermal diffusivity, specific heat and density is presented in Table 4-6. The estimated uncertainty is 12 % (Gembarovic et al., 2010).

Table 4-6: Thermal conductivity of *APA* at cryogenic temperatures and vacuum.

Temperature/ K	Thermal conductivity/ mW $m^{-1}K^{-1}$
130.16	0.996
180.16	1.379
223.16	1.773
273.16	2.429
300.16	2.872

The scale parameter F was estimated from equation (1.10), using k_c at 180.16 K (assuming that radiation accounts for 5% of the thermal conductivity at this temperature) from Table 4-6, $f = \frac{111.8}{3200} = 0.0349$, $m = 1$ and k_s at 180.16 K from equation (4.11). The lower temperature measured in Table 4-6 was not used because the conduction model does not consider the superconductivity peak of alumina close to 110 K. The scale parameter was

determined to be 5.6114 x 10^{-4}. The resulting temperature-dependent model for solid conduction for *APA* sample with $f = \frac{98.4}{3200} = 0.0308$ is presented in equation (4.13).

$$k_c(T) = -7.6023 \times 10^{-5} + \frac{0.22179}{T} \tag{4.13}$$

4.3 Effective thermal conductivity

The effective thermal conductivity of the sample had been previously measured using the Heat Flow Meter thermal conductivity test setup at *NASA* Langley Research Center(Daryabeigi, 1999a, 1999b). The test setup has been slightly modified compared to previously published reports to increase testing capability to 1900 K from 1400 K. The overall system and measurement methodology are documented elsewhere, but are presented here for completeness. The measurement system is presented in Figure 4-13. The experimental integrated thermal conductivity is calculated from measurements of heat flux, hot and cold plates temperatures and sample thickness according to equation (4.14).

$$k_{int,exp} = \frac{L}{\frac{T_h - T_c}{q}} \tag{4.14}$$

Where q is the heat flux, T_h is the temperature of the hot plate (septum plate), T_c is the temperature of the cold plate (water-cooled plate) and L is the thickness of the sample.

Figure 4-13: Schematic of thermal conductivity apparatus (Daryabeigi, 1999a).

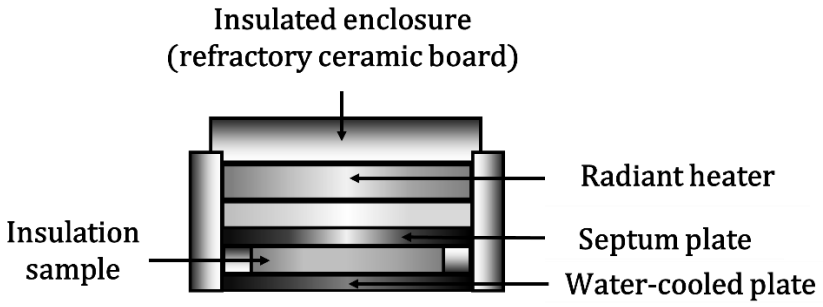

The heat flux is measured using nine thermopile thin film heat flux gages on the water-cooled plate located according to Figure 4-14. The temperature on the cold side is calculated from nine type T thermocouples embedded in the thin film heat flux gages. The average value of the measurements of the five heat flux gages and their corresponding type T thermocouples located within the central 15.24 cm × 15.24 cm metered region are used for the calculation of q and T_c, respectively.

Figure 4-14: A) Cold plate in the thermal conductivity apparatus. B) Photo of water-cooled plate with 9 heat flux gages (surface was painted black after assembly) (Courtesy of Kamran Daryabeigi).

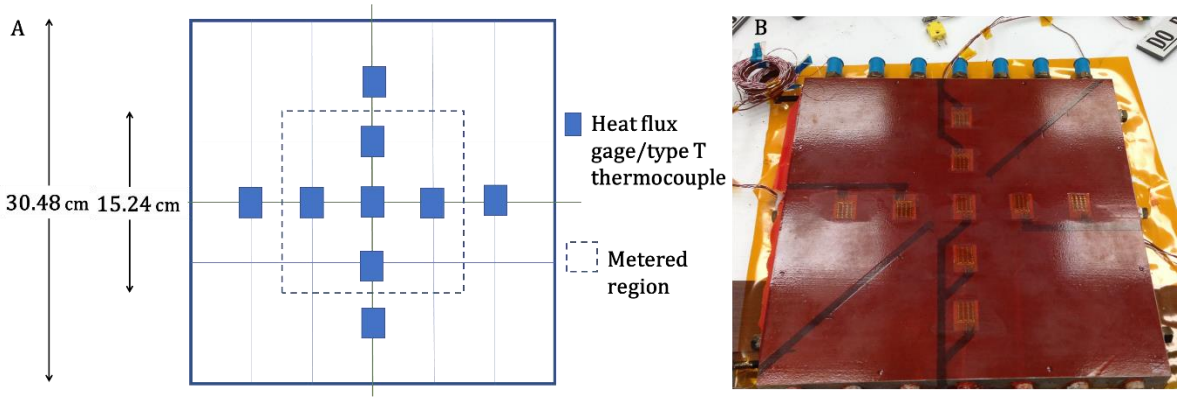

The temperature on the hot side is typically calculated from four type C thermocouples embedded in a graphite septum plate so that they are flush mounted on the surface as shown in Figure 4-15, to provide temperature measurements at the interface of septum plate and test sample. The average value of the measurements of the four type C thermocouples located within the central 15.24 cm × 15.24 cm metered region are used for the calculation of T_h.

Figure 4-15: A) Septum plate (hot plate) in the thermal conductivity apparatus. B) Type C thermocouples mounted on septum plate (side facing sample). (Courtesy of Kamran Daryabeigi).

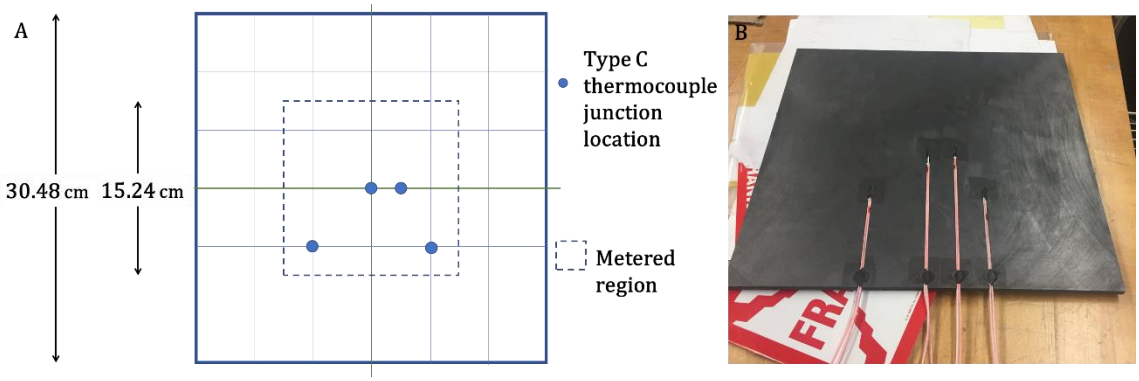

To estimate the effective thermal conductivity at several temperatures and low pressure, the measurement system is typically set in a vacuum chamber at 0.001 torr and various thermocouples are placed at different location throughout the sample thickness across the heat flux direction as shown in Figure 4-16. Under this configuration, the measured integrated thermal conductivity is determined as:

$$k_{int,exp} = \frac{L_i q}{T_i - T_c} \tag{4.15}$$

Figure 4-16: A) Measurement system set in a vacuum chamber. B) Thermometers configuration (Daryabeigi, 1999a).

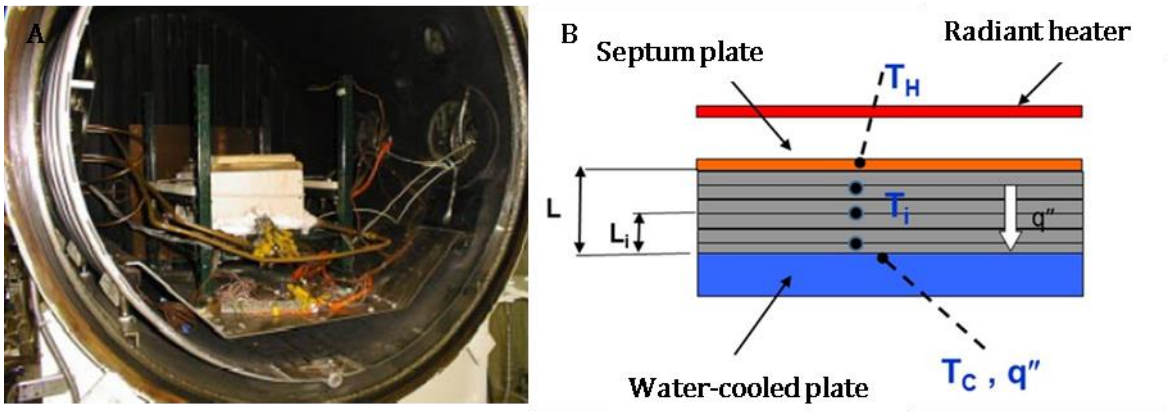

Where $k_{int,exp}$ is the calculated integrated thermal conductivity between T_i and T_c calculated from equation (4.16), q is the average measured heat flux, L_i is the height at which thermometer i is placed with respect to the water-cooled plate, T_i is the temperature of the thermometer i (which also includes T_c) and T_c is the average temperature of the water-cooled plate. The relation between effective and integrated thermal conductivity at 0.001 torr is given by:

$$k_{int,exp}(T_i, T_C, P) = \frac{1}{T_i - T_C} \int_{T_C}^{T_i} k_{eff,LP}\,(T, P)\partial T \tag{4.16}$$

$k_{eff,LP}$ can be assumed as a 3rd order polynomial of temperature as shown in equation (4.17)

$$k_{eff,LP} = a_0 + a_1 T + a_2 T^2 + a_3 T^3 \tag{4.17}$$

Combining equations (4.16) and (4.17):

$$k_{int,exp}(T_i, T_C, P) = a_0 + \frac{a_1}{2}(T_i - T_c) + \frac{a_2}{3}\left(T_i^2 + T_i T_c + T_c^2\right) + \frac{a_3}{4}(T_i + T_c)\left(T_i^2 + T_c^2\right) \tag{4.18}$$

The coefficients a_i are estimated from the measured T_i and T_c, and corresponding calculated values of $k_{int,exp}$ using the least squares technique. Once coefficients a_i are known, the effective thermal conductivity of insulation in vacuum, which consists of the contributions of radiation and solid conductions, is known according to equation (4.18).

Unfortunately, the 0.001 torr measurements on the *APA* sample had some errors, so the data at 0.1 torr were utilized, and then corrected by subtracting contributions of gas conduction at this higher pressure, to obtain the vacuum effective thermal conductivity needed here. The procedure followed is explained here for completeness. The tests on *APA* were performed by stacking 21 layers to form a specimen with a thickness of 2.54 cm. Three internal thermocouples were located within the insulator on top, 15th, 10th and 5th layer to obtain T_i, corresponding to, $T_{0.714}$, $T_{0.476}$ and $T_{0.238}$ as shown in Figure 4-17, with the subscripts referring to the non-dimensional height of each internal thermocouple with respect to total sample thickness. T_1 corresponds to average septum plate temperature T_h.

The water-cooled temperature, T_c, changed slightly with increasing septum plate temperature, T_h. For T_1 of 831.3 K, T_c was kept at 283.1 K, for T_1 of 1369.3 K, T_c was kept at 288.3 K and for T_1 of 1648.5 K, T_c was kept at 291.4 K. Equations (4.18) and (4.19) were used to develop the third order polynomial curve fit for effective thermal conductivity with temperature for *APA* sample at 0.1 torr. Given that at 0.1 torr there is some contribution due to gas conduction, the gas conduction thermal conductivity contributions at 0.1 torr inside *APA* (with its typical effective pore size for gas conduction) were calculated used the model presented in (Daryabeigi, 2010) and subsequently subtracted from effective thermal conductivity at 0.1 torr. The results were then curve fitted using a third order polynomial of temperature. The value of unknown coefficients a_i for effective thermal conductivity of *APA* in vacuum for the entire range of 300 to 1700 K according to equation (4.18) are shown in Table 4-7.

Figure 4-17: Measured integrated thermal conductivity.

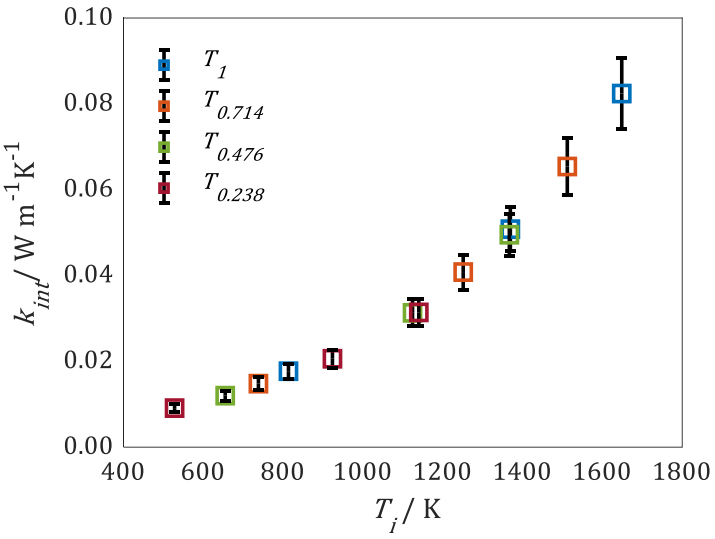

Table 4-7: Coefficients for effective thermal conductivity of *APA* in vacuum.

a_0 / W m^{-1}·K^{-1}	a_1 / W m^{-1}·K^{-2}	a_2 / W m^{-1}·K^{-3}	a_3 / W m^{-1}·K^{-4}
-1.180×10^{-2}	7.466×10^{-5}	-1.034×10^{-7}	9.867×10^{-11}

The uncertainty of the measurement system is about 10 % (Daryabeigi, 1999a). Considering the relatively low thermal conductivity at moderate temperatures, the uncertainty due to measurement system resolution of 0.001 W m^{-1}K^{-1}, was quadratically combined, as show in equation (4.19).

$$U(k_{eff,LP}) = \sqrt{(0.1k_{eff,LP})^2 + \left(0.001/\sqrt{3}\right)^2} \tag{4.19}$$

The relative error of the model is calculated as the relative difference between $k_{eff,LP}$ and $k_{eff,model}$ for temperatures between 300 K and 1700 K as shown in Table 4-8. The radiation and conduction contribution of the model are also presented in the table. The contribution of

conduction to the model is less than 5 % above 500 K. At 300 K and 400 K the conduction contribution is 22 % and 8 % respectively. The comparison between the thermal conductivity measured and predicted by the model is presented in Figure 4-18.

Table 4-8: Relative error of the model.

T/ K	k_r/ W m^{-1}·K^{-1}	k_c/ W m^{-1}·K^{-1}	$k_{eff,model}$/ W m^{-1}·K^{-1}	$k_{eff,LP}$/| W m^{-1}·K^{-1}	Relative error/ %
300	0.0024	6.63E-04	0.0030	0.0040	24.0
400	0.0052	4.78E-04	0.0057	0.0079	28.4
500	0.0090	3.68E-04	0.0093	0.0120	22.2
600	0.0137	2.94E-04	0.0140	0.0171	17.9
700	0.0203	2.41E-04	0.0205	0.0237	13.3
800	0.0294	2.01E-04	0.0296	0.0323	8.5
900	0.0410	1.70E-04	0.0412	0.0436	5.5
1000	0.0560	1.46E-04	0.0561	0.0581	3.4
1100	0.0756	1.26E-04	0.0757	0.0766	1.2
1200	0.0995	1.09E-04	0.0996	0.0994	-0.2
1300	0.1291	9.46E-05	0.1292	0.1273	-1.5
1400	0.1651	8.24E-05	0.1652	0.1608	-2.7
1500	0.2079	7.18E-05	0.2079	0.2006	-3.7
1600	0.2574	6.26E-05	0.2575	0.2471	-4.2
1700	0.3153	5.44E-05	0.3154	0.3011	-4.7

Figure 4-18: Comparison between measured and predicted thermal conductivities.

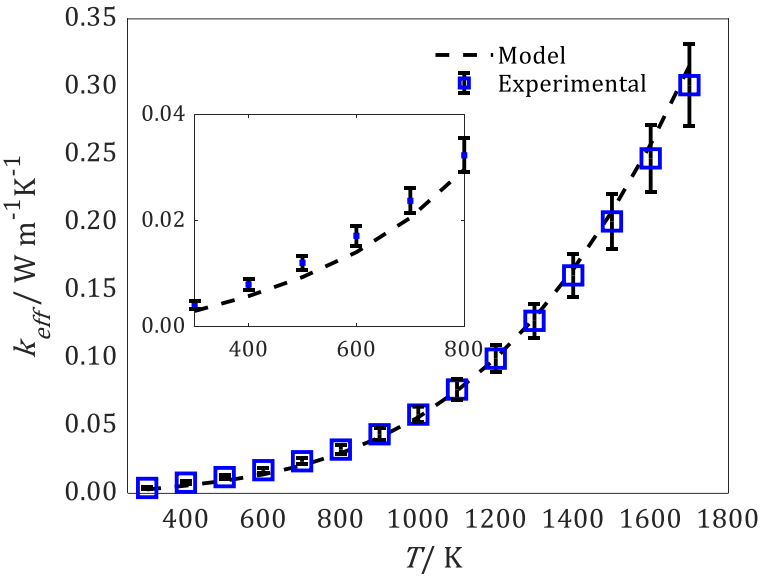

From 800 K to 1700 K, the predictions of the model are within the measurement uncertainty while the relative error ranged from -4.7 % to 8.5 %. These values are consistent with the estimations reported by several authors in similar insulation materials using semi-empirical methods (Daryabeigi, 2010; Daryabeigi et al., 2010, 2013; Kamiuto et al., 1982; Zhang et al., 2008; Zhao, Zhang, & He, 2009). Above 1100 K, all errors are negative, indicating a positive bias in the radiation model. Within this range, the absolute error tends to increase until 1700 K.

Based on the observed close agreement between model predictions and test data, it can be concluded that the current model appropriately corrects the isotropy assumption of the classical diffusion approximation by introducing the modified extinction coefficient. The correction factor $(1 - G_\lambda)$, formulated by Lee and Cunnington, computes the average reduction of radiation in a randomly oriented medium. It considers that in the case of cylinders, the radiation is scattered in two dimensions, which is limited to a cone, as shown in Figure 2-1 and defined in equations (4.9) and (4.10).

The larger errors are found at moderate temperatures (300 K to 700 K), where conduction becomes influential in the heat transfer. Therefore, the biases in k_s, F and ρ_b strongly impact the estimations of the model. This effect is accentuated by the steep slope observed in Figure 4-12 at cryogenic temperatures.

5. Uncertainty of the model

Given the uncertainty in the input variables of the radiation model, it is necessary to estimate this effect on the final calculation. This can be done using the law of propagation of uncertainties or by the Monte Carlo method. Considering the nature of the model, a hybrid technique was used.

The first section describes the uncertainty associated with the input quantities. In the second section, the uncertainty of the model is calculated by combining the input quantities. Finally, the predictions of the model are compared with the measurements, taking into account both the experimental and model uncertainties, by means of the normalized error.

5.1 Uncertainty propagation

The international recommended guideline for the estimation of uncertainty was proposed by the Bureau International des Poids et Measures (*BIPM)* in the Guide to the Expression of Uncertainty in Measurement *(GUM)* (BIPM et al., 2008a). This methodology consists of the use of the law of propagation of uncertainties, which is based on the expansion of the measurement equation using Taylor series, where the derivatives of the model with respect to the input quantities (known as sensitivity coefficients) must be evaluated. In general, it is applicable when the central limit theorem condition holds. An alternative method is to generate an estimate of the input quantities from random numbers associated with their probability distribution and then estimate the output distribution(BIPM et al., 2008b). This method is useful when the conditions for the *GUM* approach are not met or when its evaluation is impractical.

For the mathematical model represented by equations (3.2), (2.26), (2.27), (2.28), (4.5), (4.6), (4.7), (4.8) and (4.13), the use of a single method to propagate the uncertainty is inconvenient. In the factors associated with the estimation of G_λ, the *GUM* approach is easier to apply, given the computational times demanded. In the case of the Rosseland mean, where the derivatives are hard to estimate, the Monte Carlo method is the best alternative.

Considering the above, the uncertainty in the effective thermal conductivity can be estimated from equation (5.1). The description of each term is presented in the next sections.

$$u^2\left(k_{eff,model}\right) = u^2(k_c) + u^2(k_r) \tag{5.1}$$

5.2 Input quantities

5.2.1 Conduction model

The uncertainty on the thermal conductivity due to conduction (first terms of the right side in equation (5.1)) can be estimated from equations (5.2) and (5.3).

$$u^2(k_c) = (k_s f)^2 u^2(F) + (k_s F)^2 u^2(f) + (Ff)^2 u^2(k_s) \tag{5.2}$$

$$\begin{aligned} u^2(F) = {} & \left(\frac{1}{f_c k_s(180\ \mathrm{K})}\right)^2 u^2(k_c(180\ \mathrm{K})) + \left(-\frac{k_c(180\ \mathrm{K})}{f_c^2 k_s(180\ \mathrm{K})}\right)^2 u^2(f_c) \\ & + \left(-\frac{k_c(180\ \mathrm{K})}{f_c k_s^2(180\ \mathrm{K})}\right)^2 u^2(k_s(180\ \mathrm{K})) \end{aligned} \tag{5.3}$$

The uncertainty of k_c and k_s at 180 K are 0.17 mW m^{-1} K^{-1} and 6.68 W m^{-1} K^{-1}, respectively, as described in section 4.2.2. In equation (5.3) f_c is the fiber volume fraction estimated for the sample used in cryogenic measurements, i.e. $f_c = \frac{111.8}{3200} = 0.0349$. The density of the fiber parent material depends mainly on material composition, porosity, crystallinity and fiber processing method. Given that this information is not provided by the manufacturer and the wide range of densities reported in the literature (Berger & Bunsell, 1999; Bunsell. A, 2006;

Kostikov et al., 1995; Rauch et al., 1968; Wilson, 2018), a conservative uncertainty of 5% was assumed. A summary of the uncertainty estimation at 300 K, 1100 K and 1700 K is presented in Table 5-1, where c represents the sensitivity coefficient. More details can be found in annex C.

Table 5-1: Uncertainty on thermal conductivity due to conduction.

Temperature/ K	Uncertainty Component	u		c	$c \cdot u$	%
300	F	5.3E-05	-	1.2E+00	6.3E-05	66.5
	k_s	2.2E+00	W m^{-1} K^{-1}	2.0E-05	3.8E-05	24.5
	f	1.1E-03	-	2.4E-02	2.3E-05	9.1
	k_c	7.7E-05	W m^{-1} K^{-1}	-		
1100	F	5.3E-05	-	2.2E-01	1.2E-05	66.5
	k_s	4.2E-01	W m^{-1} K^{-1}	1.7E-05	7.2E-06	24.5
	f	1.1E-03	-	4.1E-03	4.4E-06	9.1
	k_c	1.5E-05	W m^{-1} K^{-1}	-		
1700	F	5.3E-05	-	9.7E-02	5.2E-06	66.5
	k_s	1.8E-01	W m^{-1} K^{-1}	1.7E-05	3.1E-06	24.5
	f	1.1E-03	-	1.8E-03	1.9E-06	9.1
	k_c	6.3E-06	W m^{-1} K^{-1}	-		

The relative uncertainty, considering a coverage factor of 2 (equivalent to a coverage probability of 95.45 % for a t-student probability distribution), is 23 % and roughly independent of temperature. The most relevant contribution comes for the estimation of the parameter F which depends on the estimation of thermal conductivity at cryogenic temperatures.

5.2.2 Radiation model

The uncertainty on the thermal conductivity due to radiation (second terms of the right hand side in equation (5.1)) can be estimated from equation (5.4).

$$u^2(k_r) = \left(\frac{16\sigma T^3}{3{\beta_R}^2}\right)^2 u^2(\beta_R) \tag{5.4}$$

Given that the Roseland mean is an integral function of wavelength, it is more convenient to estimate the uncertainty using the Monte Carlo method as described by Cordero et al.(Cordero et al., 2007). For this purpose, β_R can be expressed as a function of a series of points $\lambda_i, \bar{\beta}_{\lambda_i}$

$$\beta_R = f\left(\lambda_i, \bar{\beta}_{\lambda_i}\right) \tag{5.5}$$

The uncertainty will be estimated by generating M series of random numbers of $\bar{\beta}_{\lambda_i}$ for each wavelength λ_i and then calculating the standard deviation of the resulting distribution of β_R.

The uncertainty of $\bar{\beta}_\lambda$ at a particular wavelength can be estimated as:

$$\begin{aligned} u^2\left(\bar{\beta}_\lambda\right) = &\sum_{i=1}^{N}\left(\frac{\partial\bar{\beta}_\lambda(r_i)}{\partial v(r_i)}\right)^2 u^2(v(r_i)) + \sum_{i=1}^{N}\left(\frac{\partial\bar{\beta}_\lambda(r_i)}{\partial r_i}\right)^2 u^2(r_i) + \left(\frac{\partial\bar{\beta}_\lambda}{\partial n}\right)^2 u^2(n) \\ &+ \left(\frac{\partial\bar{\beta}_\lambda}{\partial k}\right)^2 u^2(k) + \left(\frac{\partial\bar{\beta}_\lambda}{\partial f}\right)^2 u^2(f) \end{aligned} \tag{5.6}$$

To estimate the uncertainty in $v(r)$, it is important to note that in a counting experiment, each bin can be represented by a binomial distribution, then for the case of relative frequency, the standard deviation can be estimated as (Caria, 2000):

$$u(v(r_i)) = \frac{\sqrt{N_{total}v(r_i)(1-v(r_i))}}{N_{total}} \tag{5.7}$$

Where N_{total} is the total number of elements counted. The sensitivity coefficient for $v(r_i)$ is given by:

$$\frac{\partial\bar{\beta}_\lambda(r_i)}{\partial v(r_i)} = \frac{\bar{\beta}_\lambda(r_i)}{v(r_i)} \tag{5.8}$$

The uncertainty of the measured diameter was assumed to be 2.5 %, considering the state of art methodologies, equipment and standard reference materials (Crouzier et al., 2019; Fu et al., 1994). The sensitivity coefficient for r_i was estimated numerically as $\Delta\bar{\beta}_\lambda/\Delta r$ for a variation of 1 % in r.

Between 0.5 μm and 6 μm, i.e., the transmission range of alumina, the available data for the refractive index are based on high precision spectrometer measurements, the uncertainty using this method is about 2×10^{-5} (Malitson et al., 1958; Rodney & Spindler, 1953). At other wavelengths most of the data available are based on reflectivity measurements (Barker, 1963; Gervais & Piriou, 1974; Querry, 1985; Worrell, 1986). The uncertainty for this method is usually below 2×10^{-2} at 295 K, while at higher temperatures the uncertainty seems to be lowered according to Gervais and Piriou (Gervais & Piriou, 1974). For estimation purposes, a moderate value of 2×10^{-2} was used. The sensitivity coefficient for the refractive index was estimated numerically as $\Delta\bar{\beta}_\lambda/\Delta n$ for a variation of 1 % in n.

The uncertainty for absorption index was calculated from the uncertainty reported in the absorption coefficient and assuming that the uncertainty in the determination of wavelength is negligible. Considering equation (2.42), it leads to

$$u^2(k) = \left(\frac{\lambda}{4\pi}\right)^2 u^2(\kappa) \tag{5.9}$$

In the transparency region at high temperatures, the data are based on transmittance measurements with uncertainties between 1.5 % and 3 %, depending on temperature. However, at transmittance lower than 0.5 % the absolute uncertainty is about 1×10^{-3} according to Billard and Piriou (Billard & Piriou, 1974). Also, at high temperature and low absorption coefficients ($\kappa < 0.01$ cm^{-1}), Gryvnak and Burch pointed out that the uncertainty can be as high as 30 %. At higher absorption coefficients they suggest an uncertainty between 10 % and 15 % (Gryvnak & Burch, 1965). At higher wavelengths, the multiphonon model presented in section 2.3.2 was used with a maximum uncertainty of 35 % at 1700 K. As in the case of the refractive index, the sensitivity coefficient was estimated numerically as $\Delta\bar{\beta}_\lambda/\Delta k$ for a variation of 1 % in k.

The uncertainty of f can be estimated from equation (5.10), where the uncertainties on ρ_b and ρ_s were estimated as 4 % (Gembarovic et al., 2010) and 5 % (See section 5.2.1), respectively. The sensitivity coefficient for f is given by equation (5.11).

$$u^2(f) = \left(\frac{1}{\rho_s}\right)^2 u^2(\rho_b) + \left(-\frac{\rho_b}{\rho_s^2}\right)^2 u^2(\rho_s) \tag{5.10}$$

$$\frac{\partial \bar{\beta}_\lambda}{\partial f} = \frac{\bar{\beta}_\lambda}{f} \tag{5.11}$$

A summary of the input quantities of the radiation model and their respective uncertainty estimations are presented in Table 5-2.

Table 5-2: Uncertainty of the input quantities.

Quantity	Estimated value		Uncertainty	
ρ_b	98.4	kg/m³	4	%
ρ_f	3200	kg/m³	5	%
n	Figure 4-7	-	2E-5 (λ between 0.5 µm and 6 µm)	-
			0.02 (λ between 6 µm to 30 µm)	
k	Figure 4-8	-	30 ($k < 5E-7$ and λ between 0.5 µm and 7 µm	%
			15 ($k > 5E-7$ and λ between 0.5 µm and 7 µm	
			35 (λ between 7 µm and 30 µm)	
r	Figure 4-6	µm	5	%
$v(r)$	Figure 4-6	-	Equation (5.7)	-

An example of the uncertainty estimation of the modified extinction coefficient for a wavelength of 0.5 µm at 1700 K is presented in Table 5-3. The uncertainty for all wavelengths is detailed in Annex C.

Table 5-3: Uncertainty of modified extinction coefficient at 0.5 μm and 1700 K.

Uncertainty component	Estimated value		Type	D	U	u	c	$c \cdot u$	ν_i	%
$v(r_1)$	0.01	-	A	B	7.0E-03	7.0E-03	1.1E+04	7.6E+01	200	4
$v(r_2)$	0.25		A	B	3.1E-02	3.1E-02	5.3E+03	1.6E+02	200	20
$v(r_3)$	0.51		A	B	3.5E-02	3.5E-02	4.8E+03	1.7E+02	200	22
$v(r_4)$	0.15		A	B	2.5E-02	2.5E-02	4.0E+03	1.0E+02	200	8
$v(r_5)$	0.04		A	B	1.5E-02	1.5E-02	3.2E+03	4.6E+01	200	2
$v(r_6)$	0.03		A	B	1.3E-02	1.3E-02	3.4E+03	4.3E+01	200	1
r_1	7.5E-07	m	A	N	1.9E-08	9.4E-09	-8.4E+08	-7.9E+00	200	0
r_2	1.3E-06		A	N	3.1E-08	1.6E-08	-6.5E+09	-1.0E+02	200	8
r_3	1.8E-06		A	N	4.4E-08	2.2E-08	-2.1E+09	-4.5E+01	200	2
r_4	2.3E-06		A	N	5.6E-08	2.8E-08	4.4E+09	1.2E+02	200	12
r_5	2.8E-06		A	N	6.9E-08	3.4E-08	2.7E+08	9.4E+00	200	0
r_6	3.3E-06		A	N	8.1E-08	4.1E-08	-2.6E+08	-1.1E+01	200	0
n	1.8178	-	B	R	2.0E-05	1.2E-05	3.6E+02	4.2E-03	200	0
k	3.42E-07	-	B	R	1.0E-07	5.9E-08	4.6E+05	2.7E-02	200	0
f	3.08E-02	-	A	N	2.2E-03	1.1E-03	1.6E+05	1.7E+02	356	21

	Estimated value		U_{rel}	D	U	u	k_{ex}	ν_{eff}
$\bar{\beta}_{0.5\ \mu m}$	4766	m^{-1}	15%	N	726	363	2.0	1396

The relative uncertainty, considering a coverage factor of 2 (equivalent to a coverage probability of 95.45 % for a t-student probability distribution), is 15 % at 0.5 μm. At this wavelength the uncertainty due to the estimation of the fractional fiber volume represents the major contribution. At higher wavelengths, the contribution due to the estimation of the absorption coefficient becomes dominant.

The relative uncertainty of the modified extinction coefficient is presented in Table 5-4 at 1700 K, 1100 K and 300 K.

Table 5-4: Relative uncertainty of the modified extinction.

Wavelength/ µm	U_{rel}(1700 K)/ %	U_{rel}(1100 K)/ %	Wavelength/ µm	U_{rel}(300 K)/ %
0.5	15	17	1.0	14
1.0	16	26	2.5	17
1.5	18	20	4.0	14
2.0	19	17	5.5	14
2.5	20	17	7.0	16
3.0	19	17	8.5	25
3.5	14	14	10.0	38
4.0	14	14	11.5	18
4.5	14	15	13.0	131
5.0	15	16	14.5	24
5.5	15	15	16.0	17
6.0	15	15	17.5	15
6.5	15	16	19.0	16
7.0	15	15	20.5	14
7.5	18	17	22.0	15
8.0	22	21	23.5	16
8.5	24	27	25.0	15
9.0	28	33	26.5	16
9.5	29	37	28.0	14
10.0	30	37	29.5	15
-	-	-	30.0	14

Considering the pair of data $\lambda_i, \bar{\beta}_{\lambda_i}$ and the uncertainties in Table 5-4, 1 x 10^6 realizations of the Rosseland mean were performed using the Monte Carlo method, from normally distributed random numbers. It is important to mention that given the high relative uncertainties in $\bar{\beta}_{\lambda_i}$, the outliers generated in the random numbers were removed using the Grubbs's test (Kaptein & van den Heuvel, 2022). Figures 5-1 to 5-3 present the resulting histogram at 1700 K, 1100 K

and 300 K, respectively. The estimated relative uncertainty between 300 K and 1700 K, calculated as standard deviation, is presented in Table 5-5.

Figure 5-1: Histogram of the Rosseland mean using the Monte Carlo method at 1700 K.

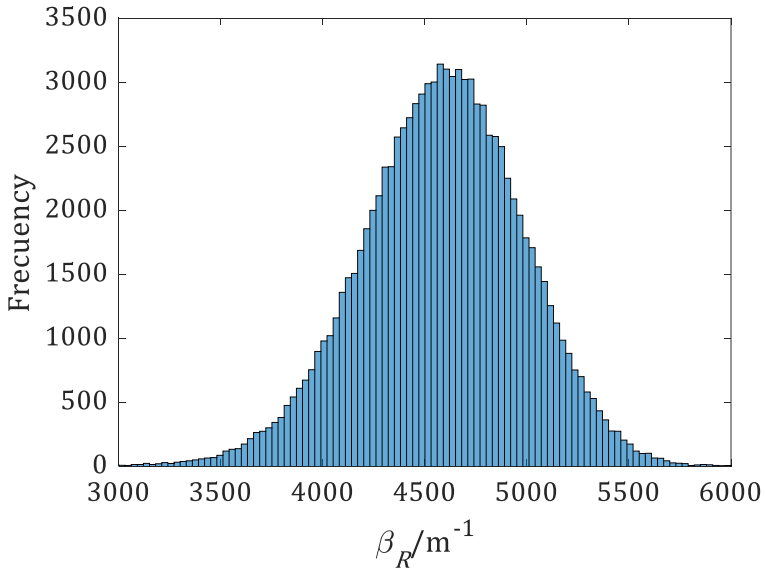

Figure 5-2: Histogram of the Rosseland mean using the Monte Carlo method at 1100 K.

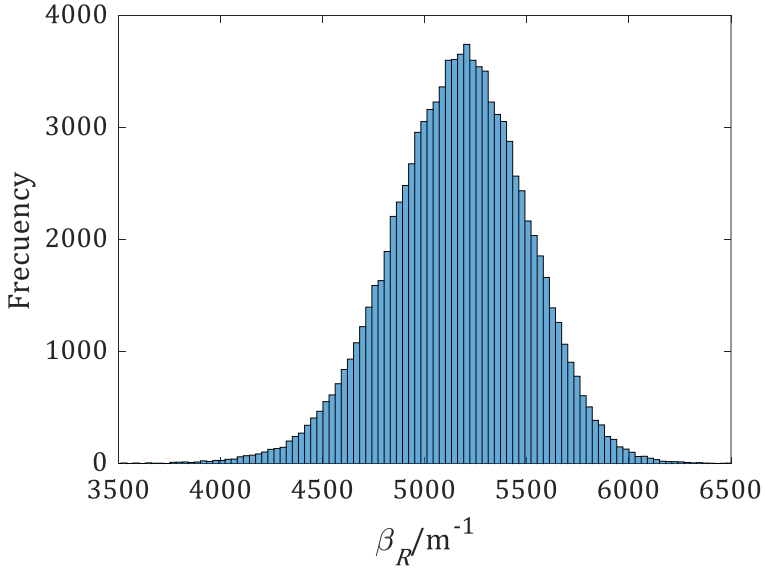

Figure 5-3: Histogram of the Rosseland mean using the Monte Carlo method at 300 K.

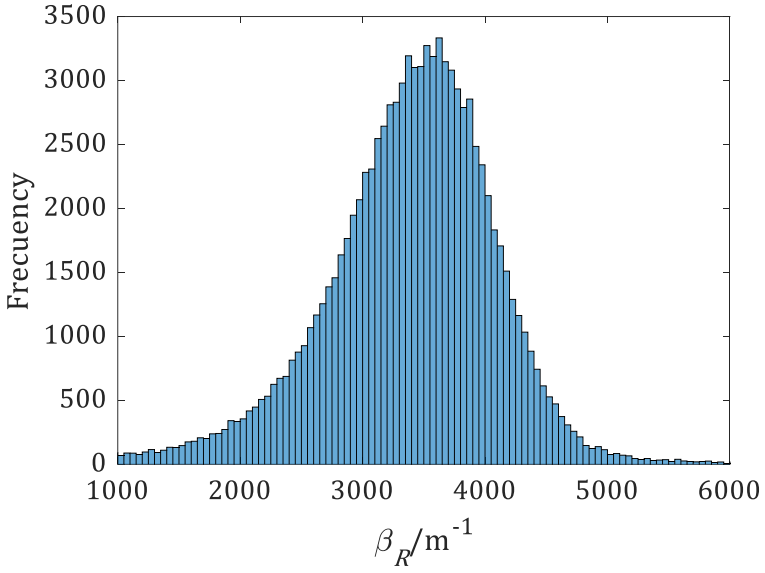

Table 5-5: Relative uncertainty of the Rosseland mean.

Temperature/ K	β_R/ m^{-1}	$u_{rel}(\beta_R)$/ %
1700	4711.9	9
1600	4812.3	8
1500	4910.0	8
1400	5026.2	8
1300	5145.9	7
1200	5251.6	7
1100	5325.0	7
1000	5403.3	9
900	5374.9	10
800	5274.7	12
700	5109.6	14
600	4752.4	16
500	4214.6	18
400	3739.1	20
300	3434.4	22

5.3 Performance of the model

The uncertainty in the predicted effective thermal conductivity considering the results from sections 5.2.1 and 5.2.2 and equations (5.1) and (5.4) is presented in Table 5-6, for a coverage factor of 2.

Table 5-6: Relative uncertainty and normalized error of the effective thermal conductivity predicted and measured.

Temperature/ K	$U_{rel}(k_c)$/ %	$U_{rel}(k_r)$/ %	$U_{rel}(k_{eff,model})$/ %	$U_{rel}(k_{eff,LP})$/ %	E_n
300	23	45	35	18	0.74
400	23	41	37	13	0.96
500	23	37	35	11	0.75
600	23	33	32	11	0.63
700	23	29	29	10	0.50
800	23	25	25	10	0.34
900	23	21	21	10	0.25
1000	23	17	17	10	0.18
1100	23	13	13	10	0.07
1200	23	14	14	10	-0.01
1300	23	14	14	10	-0.08
1400	23	15	15	10	-0.15
1500	23	16	16	10	-0.19
1600	23	17	17	10	-0.21
1700	23	17	17	10	-0.23

The comparison of the predictions of the model and the measurements taking into account the uncertainties is presented in Figure 5-4, where the blue region represents the uncertainty range of the model.

Figure 5-4: Uncertainty of the model.

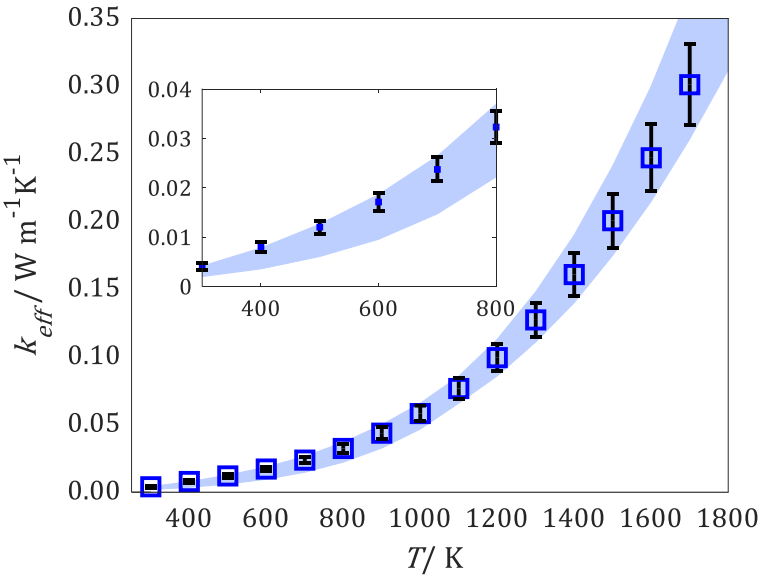

In order to check the compatibility of the errors with the uncertainties, the normalized error was calculated according to equation (5.12) (International Organization for Standardization (ISO), 2015)

$$E_n = \frac{k_{eff,exp} - k_{eff,model}}{\sqrt{U^2\left(k_{eff,exp}\right) + U^2\left(k_{eff,model}\right)}} \tag{5.12}$$

The numerator in equation (5.12) represents the bias of the model and the denominator the uncertainty of the comparison, which combines quadratically the uncertainties of the model and the measurements. The interval $|E_n| \leq 1.0$ can be interpreted as a region of acceptance, where values inside this interval represent that the two quantities being compared are compatible. Conversely, values outside this interval indicate estimation issues of the model or miss estimated uncertainties. The last column of Table 5-6 shows the normalized error of the model. Considering that the values are inside the acceptance region, it can be concluded that the model and the measurement are compatible for temperatures between 300 K and 1700 K.

6. Conclusions and Recommendations

6.1 Conclusions

A predictive radiation model based on a modified diffusion approximation applicable to low density fibrous materials at high temperatures was evaluated. The model was validated using previous measurements of effective thermal conductivity on a low-density alumina-based fibrous insulation at temperatures as high as 1700 K. The inputs of the model are size distribution, fiber volume fraction, and the complex index of refraction. These properties were measured or estimated independently of heat transfer measurements. The size distribution was estimated by considering the diameter and length of the fibers using scanning electron microscopy (*SEM*). The fiber volume fraction was estimated from the density of the sample and the density of the fiber parent material. The complex index of refraction was estimated through a combination of literature data and the multiphonon model. The solid conduction component of the model was evaluated using a semi-empirical method estimated from measurements in vacuum at cryogenic temperatures.

For the sample under study, the uncertainty of the model ranged from 13 % to 37 % and was estimated from the law of propagation of errors and the Monte Carlo method. The higher uncertainties are observed at moderate temperatures, which are related to the solid conduction uncertainties due to the particular behavior of alumina at cryogenic temperatures in the presence of mineral oxides impurities and the uncertainty associated with the estimation of the absorption coefficient. At high temperatures, the main sources of uncertainty are related to the estimation of size distribution and volume fraction.

The proposed model agreed well with the measured values of thermal conductivity for temperatures ranging from 300 K to 1700 K. The relative errors obtained with the model are

consistent with the estimated uncertainties of both measurements and model and comparable to those obtained by semi-empirical methods. Given that at high temperatures, more than 95% of the heat transfer is due to radiation, the model can be considered successful. The main limitation of the classical diffusion approximation, when used in fibrous insulation, is the isotropic assumption. It was shown that the correction factor $(1 - G_\lambda)$ applied in the extinction coefficient, appropriately model the anisotropy in a randomly oriented media.

6.2 Recommendations

So far, the modified diffusion approximation has been successfully validated on silica and alumina insulation. The model could be applied to less studied materials, such as yttria-stabilized zirconia, and heterogeneous materials. The latter represents an important challenge in estimating the radiative properties. Although the linear mixing rule has been successfully applied to predict the extinction coefficients in aerogel/fiber composites, the physical basis of this approach seems questionable for *OFI* systems, given the complex electromagnetic, chemical, and mechanical interactions at the fiber/opacifier interface. For these materials, more elaborate approaches based on effective medium theories such as Maxwell-Garnett, Bruggeman, and Lorentz-Lorenz models are promising alternatives that have not yet been applied in the context of high-temperature thermal insulation.

To independently study the contribution of radiation, apart from conduction, a rigorous approach, such as the Discrete Ordinates Method (*DOM*), can be evaluated for further validation of the model using transmittance data.

Considering that, at high temperatures, most of the uncertainty in the model arises from the morphological properties of the material, novel techniques such as X-ray Computed Tomography can be a viable option. For instance, in estimating the fiber volume fraction, the method employed in this study is heavily influenced by the material's heterogeneity. Additionally, the fiber size distribution estimation has limitations as it relies on 2D cross-sections. Although radiation is the primary focus of this research, the solid conduction model could also be enhanced by incorporating X-ray Computed Tomography in conjunction with tortuosity-based models.

A. Annex: Fiber distribution from *SEM* measurements

The fiber size and fiber distribution of the *APA* sample were measured using the software ImageJ (Schneider et al., 2012). The identification of each fiber measured is presented in Figure A- 1. The diameter, length and angle of each fiber is presented in tables A- 1. A- 2. A- 3 and A- 4. The even fiber IDs were reserved for measuring the length of the fibers and they appear in the fourth column of the corresponding odd fiber ID.

Figure A- 1: *SEM* measurements using ImageJ.

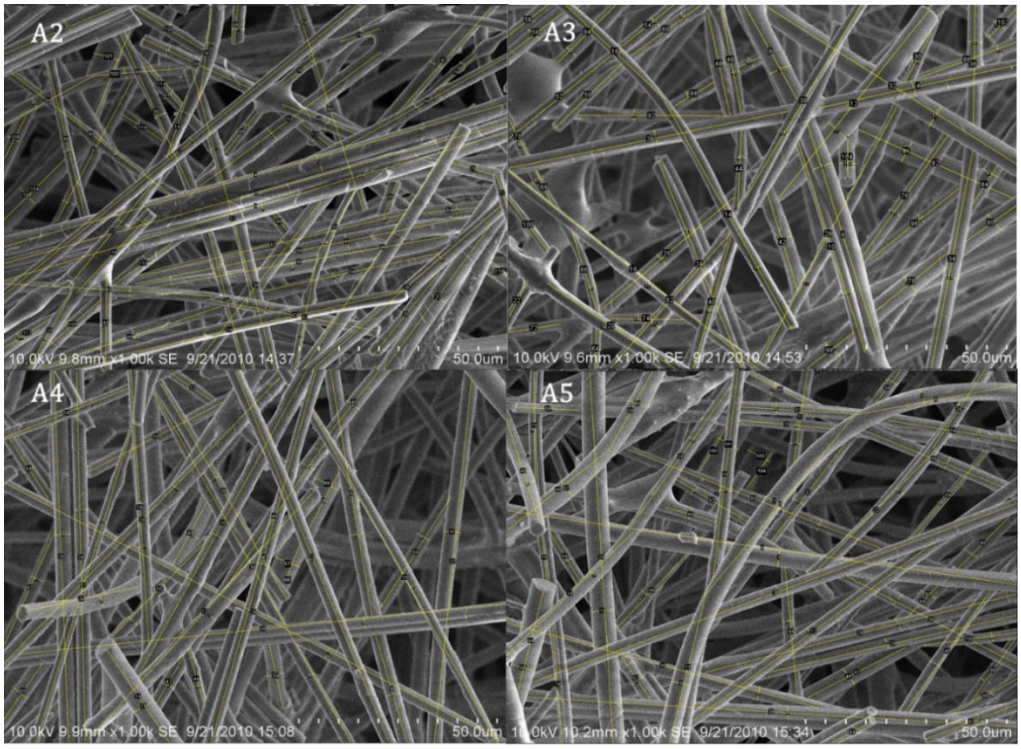

Table A- 1: Fiber measurements for A2.

Fiber ID	Angle/ degree	Diameter/ µm	Length/ µm	Fiber ID	Angle/ degree	Diameter/ µm	Length/ µm
1	-46.469	2.759	117.274	63	61.821	3.176	30.014
3	-68.875	4.005	133.216	65	62.650	3.265	20.223
5	-68.552	2.977	133.020	67	-31.430	2.110	13.682
7	-70.560	3.606	133.560	69	-106.189	3.228	11.360
9	-47.816	3.991	58.404	71	18.435	2.530	9.962
11	19.026	2.987	81.428	73	-41.186	2.126	14.375
13	-23.962	2.955	17.140	75	-46.637	2.476	10.871
15	-19.983	3.511	23.803	77	-67.166	1.972	10.784
17	-36.158	3.220	27.963	79	20.556	3.990	56.010
19	-28.072	3.400	22.825	81	-72.897	2.720	69.440
21	-35.311	2.941	33.812	83	-85.764	2.707	14.080
23	-68.962	2.786	91.885	85	36.027	2.720	5.685
25	-29.745	3.225	74.995	87	12.529	2.766	41.622
27	-47.203	3.680	64.577	89	48.814	2.126	51.476
29	-28.887	3.312	27.364	91	-22.989	3.585	41.639
31	-32.125	4.663	46.871	93	-62.650	3.265	25.973
33	15.255	3.421	36.963	95	-75.530	3.202	22.987
35	26.565	3.354	44.199	97	-1.685	3.401	10.448
37	-31.218	3.859	54.440	99	55.176	2.802	20.925
39	-90.000	2.800	53.003	101	-58.782	3.859	30.989
41	73.811	3.228	43.186	103	-47.231	4.901	22.346
43	4.086	2.807	24.501	105	-24.905	2.988	12.612
45	107.819	2.941	49.114	107	-47.603	2.993	19.817
47	-79.046	3.101	76.008	109	-45.000	2.992	18.920
49	-18.435	1.897	21.556	111	-54.689	2.941	13.868
51	-6.009	1.910	27.300	113	40.030	3.265	15.467
53	-72.897	2.720	46.532	115	53.973	2.720	12.592
55	-73.540	3.993	84.882	117	54.462	3.441	5.547

Fiber ID	Angle/ degree	Diameter/ µm	Length/ µm	Fiber ID	Angle/ degree	Diameter/ µm	Length/ µm
57	-18.435	3.162	9.025	119	43.727	3.183	9.079
59	-49.399	2.766	47.171	121	-15.255	6.841	23.937
61	-29.358	3.672	37.095	-	-	-	-

Table A- 2: Fiber measurements for A3.

Fiber ID	Angle/ degree	Diameter/ µm	Length/ µm	Fiber ID	Angle/ degree	Diameter/ µm	Length/ µm
1	-74.624	3.985	71.918	53	-40.815	2.907	17.273
3	-73.686	3.990	50.512	55	-38.660	3.842	17.367
5	19.885	4.357	60.133	57	-40.815	2.907	12.588
7	24.702	4.922	27.918	59	-51.340	2.561	22.000
9	14.931	2.991	57.222	61	-39.401	3.624	45.946
11	-45.000	4.940	61.386	63	-2.121	2.702	10.402
13	30.651	2.996	67.830	65	18.435	2.530	21.388
15	43.363	2.476	34.861	67	27.553	2.594	9.661
17	48.814	2.126	81.062	69	27.646	2.371	10.733
19	54.462	3.441	39.111	71	96.340	2.717	13.086
21	-37.304	2.640	9.259	73	92.291	2.502	19.002
23	22.932	2.823	57.494	75	-30.651	2.999	38.194
25	-50.599	3.624	44.995	77	-51.170	4.814	23.712
27	-27.408	2.982	74.647	79	-51.340	4.701	16.300
29	-17.103	2.720	14.536	81	62.592	5.043	42.730
31	59.199	5.040	74.722	83	-28.706	4.089	11.439
33	-12.680	3.982	57.351	85	-64.290	2.971	26.522
35	-3.013	3.805	31.903	87	-50.440	2.964	11.904
37	-22.932	2.823	58.521	89	-56.310	2.884	5.770
39	-10.886	2.648	35.399	91	-90.000	2.973	37.501
41	19.747	3.983	26.513	93	-46.219	3.324	21.217
43	-3.945	2.907	19.916	95	-46.548	2.617	29.039
45	13.496	2.571	28.497	97	-46.507	4.817	15.227
47	16.699	3.985	27.554	99	35.218	1.981	17.123
49	-33.690	2.884	23.900	101	-38.157	3.561	10.406
51	-41.009	2.982	33.636	103	1.332	3.990	10.700

Table A- 3: Fiber measurements for A4.

Fiber ID	Angle/ degree	Diameter/ µm	Length/ µm	Fiber ID	Angle/ degree	Diameter/ µm	Length/ µm
1	18.970	3.384	101.731	37	26.565	2.995	63.545
3	-16.189	3.228	98.296	39	-30.735	3.991	18.212
5	5.856	3.920	63.491	41	-27.979	3.624	13.000
7	12.200	3.785	28.036	43	17.745	2.625	15.096
9	27.553	2.594	95.808	45	-36.027	3.982	20.568
11	-41.186	3.987	83.398	47	-29.932	3.808	45.322
13	29.511	5.060	28.152	49	-53.130	2.974	38.331
15	-25.278	3.981	88.310	51	48.991	2.983	11.954
17	7.595	2.981	70.351	53	-66.801	2.285	33.890
19	-40.601	3.688	101.205	55	-43.781	3.324	34.155
21	-14.036	2.474	83.256	57	12.095	3.990	16.498
23	5.194	3.314	94.426	59	-38.290	4.141	17.171
25	-176.987	3.805	94.576	61	-19.440	3.606	31.557
27	-111.801	3.231	142.679	63	31.264	3.276	18.224
29	-80.838	2.999	124.350	65	-27.897	3.847	33.486
31	-6.483	3.993	92.678	67	-22.620	6.500	10.993
33	-75.530	3.202	29.676	69	-30.256	6.946	16.329
35	25.641	2.773	101.947	-	-	-	-

Table A- 4: Fiber measurements for A5.

Fiber ID	Angle/ degree	Diameter/ µm	Length/ µm	Fiber ID	Angle/ degree	Diameter/ µm	Length/ µm
1	-62.700	3.489	130.255	53	-100.620	3.256	32.748
3	83.797	3.995	128.992	55	64.231	3.220	37.792
5	-68.682	3.992	41.109	57	-26.565	1.565	28.581
7	-29.055	4.726	58.849	59	65.095	2.988	68.039
9	-10.840	4.085	39.366	61	34.160	3.384	13.257
11	-46.219	3.324	75.820	63	28.301	2.953	14.544
13	-43.831	3.466	44.548	65	67.380	2.600	12.940
15	-33.179	2.990	44.386	67	90.000	2.500	16.115
17	-6.911	3.324	53.163	69	-94.236	2.707	23.702
19	6.654	4.994	95.183	71	-3.814	2.976	23.646
21	-38.047	2.921	44.129	73	11.310	1.968	29.913
23	-20.772	2.990	23.409	75	10.008	1.726	15.000
25	-63.435	3.578	80.523	77	0.000	1.954	27.701
27	-72.181	2.941	63.478	79	63.435	2.995	17.671
29	51.340	3.842	48.130	81	-55.784	2.979	24.662
31	-31.264	3.276	31.380	83	-52.696	2.640	12.394
33	-24.305	3.401	10.700	85	-32.574	3.990	18.953
35	78.111	3.883	80.770	87	-27.121	3.993	11.669
37	-90.000	3.600	123.235	89	-51.340	2.561	18.212
39	-31.608	2.986	37.891	91	47.862	2.832	21.266
41	-55.670	4.265	27.507	93	-16.535	5.176	26.509
43	7.352	2.994	33.046	95	22.306	3.986	27.293
45	-35.134	3.302	25.187	97	-26.565	2.907	19.252
47	-50.856	4.935	32.641	99	-77.005	2.668	23.816
49	-17.745	4.781	22.730	101	149.349	6.277	13.137
51	-90.000	2.974	28.557	103	-28.124	6.576	11.150

B. Annex: Sensitivity analysis

The integrals in equations (2.13), (2.29), (2.26), (2.27) and (2.28) were solved using the trapezoidal rule. A sensitivity analysis for the number of discrete steps is presented for each integral.

The integrand in equation (4.7) of extinction coefficient as a function of ϕ at $\lambda = 1$ μm, $r = 1.6$ μm and $T = 1000$ K is presented in Figure B- 1 for several step sizes $\Delta\phi$. The spectral variation of the extinction coefficient according to equation (4.7) is presented in Figure B- 2. For a step $\Delta\phi \geq \pi/20$, the mean relative difference in the extinction coefficient evaluated over the spectral range is less than 0.1 %.

Figure B- 1: Integrand of equation (4.7).

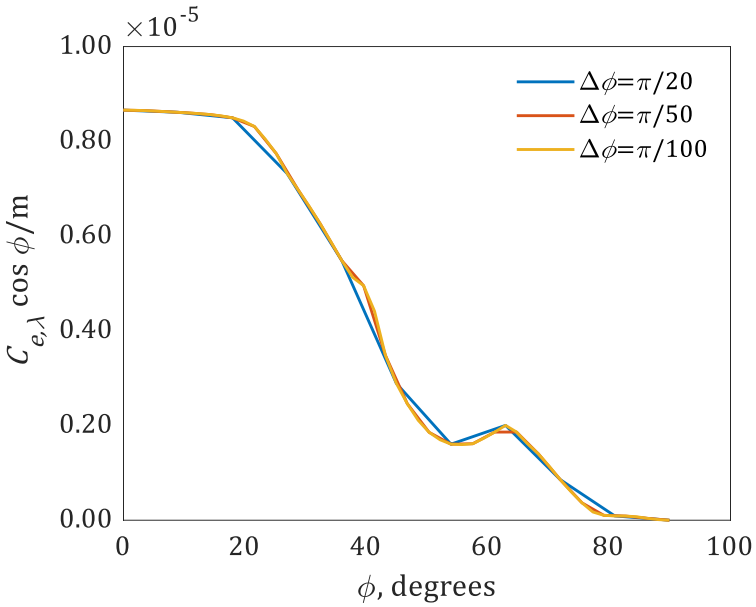

Figure B- 2: Spectral variation of the extinction coefficient.

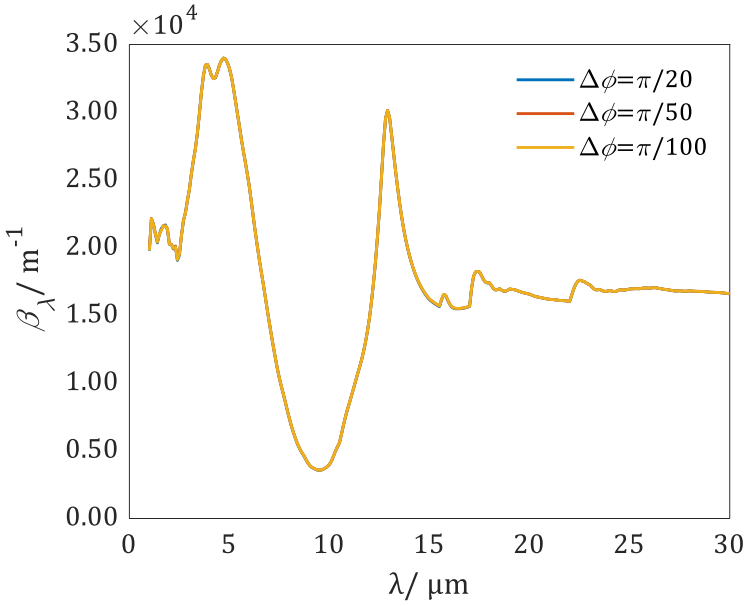

The integrand in equation (4.8) as a function of ϕ at $\lambda = 1$ μm, $r = 1.6$ μm, $\eta = \pi/4$ and $T = 1000$ K is presented in Figure B- 3 for several step sizes $\Delta\phi$.

Figure B- 3: Integrand of equation (4.8).

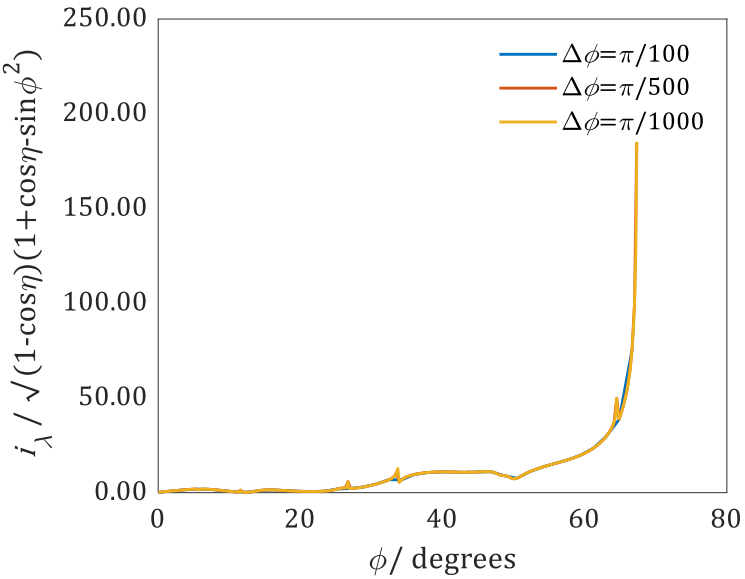

The spectral variation of the product of the scattering coefficient and the phase function according to equation (4.8) is presented in Figure B- 4. For a step $\Delta\phi \geq \pi/500$ the mean relative difference in the extinction coefficient evaluated over the spectral range is less than 0.5 %.

Figure B- 4: Spectral variation of the product of the scattering coefficient and phase function.

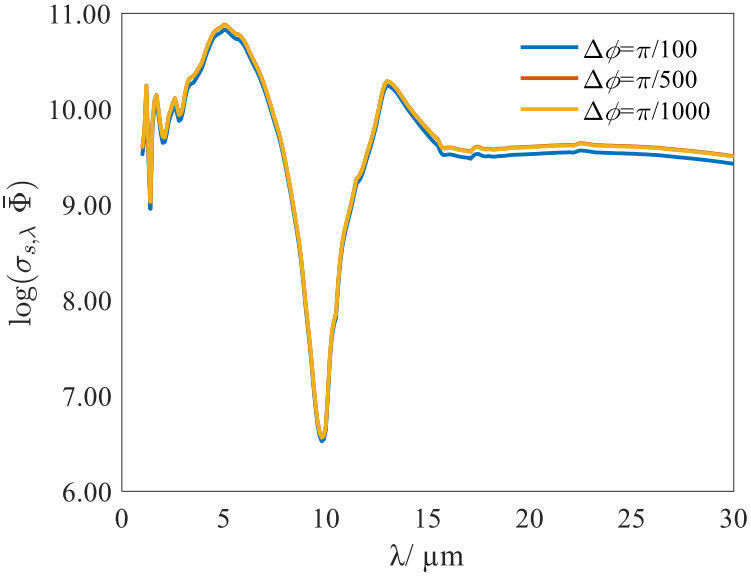

The integrand in equation (2.28) as a function of ω_i at $\lambda = 1$ µm, r = 1.6 µm, $\mu_i = 0.2$, $\mu_s = 0.1$ and $T = 1000$ K is presented in Figure B- 5 for several step sizes $\Delta\omega_i$. The spectral variation of the product of the scattering coefficient and the phase function as function of ω_i according to equation (2.28) is presented in Figure B- 6. For a step $\Delta\omega_i \geq \pi/100$ the mean relative difference evaluated over the spectral range is less than 0.5 %.

Figure B- 5: Integrand of equation (2.28).

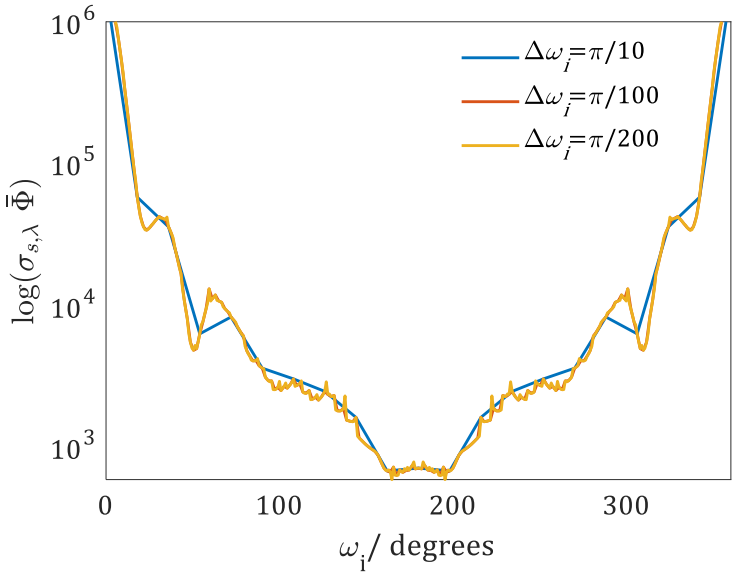

Figure B- 6: Spectral variation of the product of the scattering coefficient and phase function as function of ω_i.

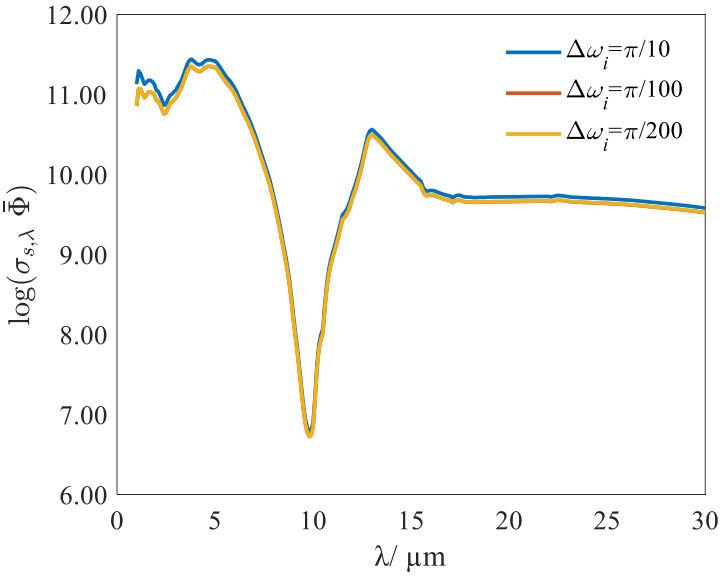

The first integrand in equation (2.27) as a function of μ_i at $\lambda = 1$ μm, $T = 1000$ K and $\mu_s = 0.1$ is presented in Figure B- 7 for several step sizes $\Delta\mu_i$. In the integration of equation (2.27) it is important to note that according with equation (2.16), when μ_s and μ_i are too close, η tends to zero and the phase function becomes discontinuous. In order to avoid the discontinuity, η is restricted to values greater than 1×10^{-2} radians.

Figure B- 7: First integrand of equation (2.27) at $\mu_s = 0.1$.

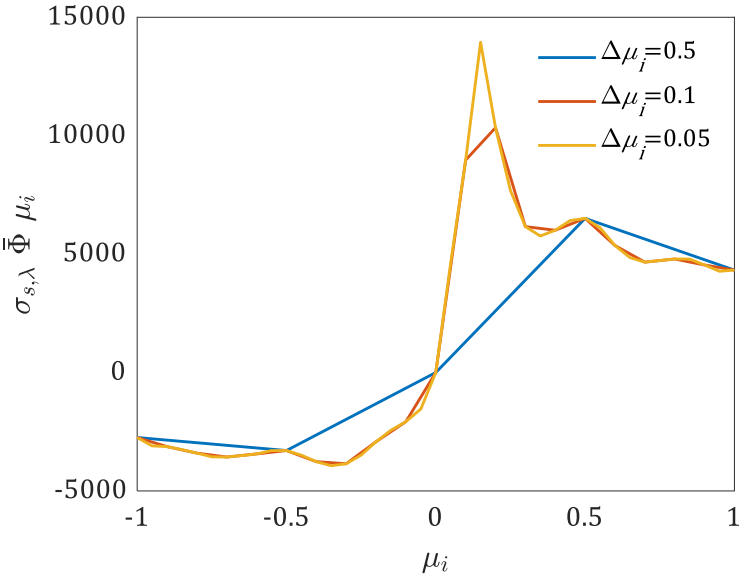

The spectral variation of the product of the scattering coefficient, the phase function and μ_i as function of μ_i according to equation (2.27) is presented in Figure B- 8. For a step $\Delta\mu_i \geq 0.1$ the mean relative difference evaluated over the spectral range is less than 3 %.

Figure B- 8: Spectral variation of the integral of the product of the scattering coefficient, phase function and μ_i.

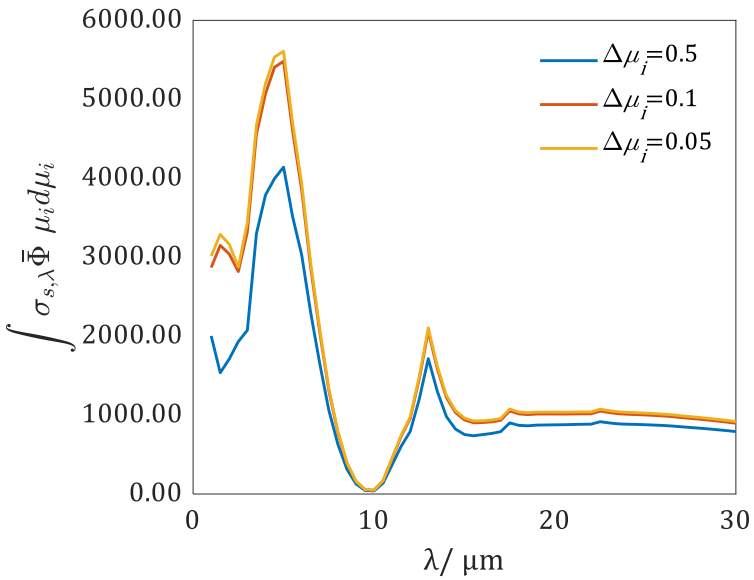

The second integrand in equation (2.27) as a function of μ_s at $\lambda = 1$ µm and $T = 1000$ K is presented in Figure B- 9 for several step sizes $\Delta\mu_s$. It is important to use a step of $\mu_s < 0.05$ in order to reproduce the oscillations of the curve. The spectral variation of the double integral; in equation (2.27) is presented in Figure B- 10. For a step $\Delta\mu_i \geq 0.02$ the mean relative difference evaluated over the spectral range is about 2 %.

Figure B- 9: Second integrand of equation (2.27).

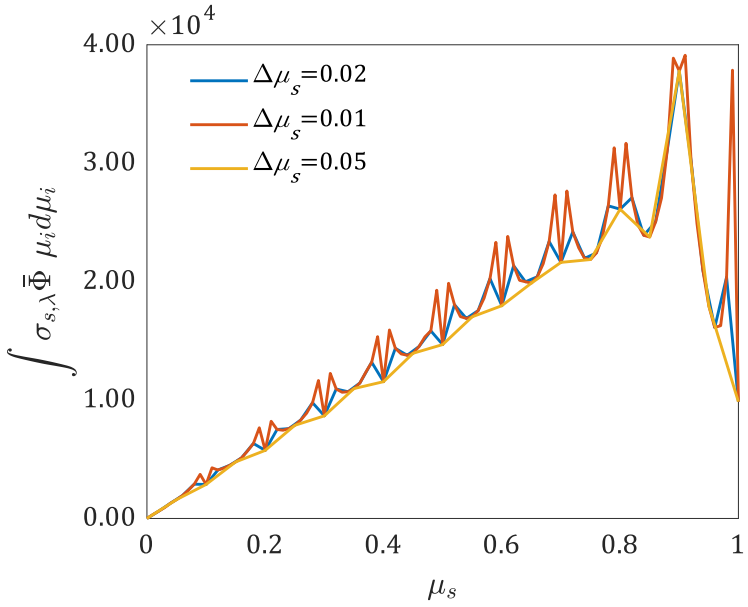

Figure B- 10: Spectral variation of the integral in equation (2.27).

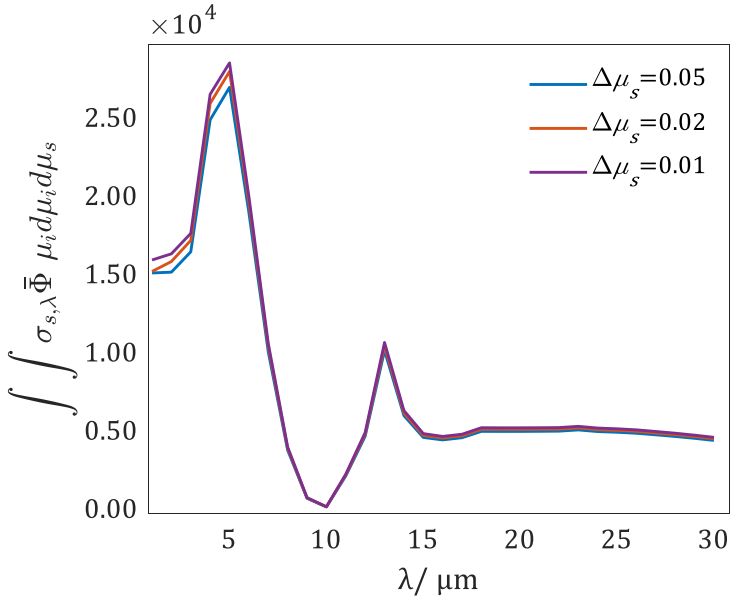

C.Annex: Uncertainty according to *GUM* method

Considering the measurand y defined by the input quantities $x_1 . x_2 . \ldots . x_n$ through the function f:

$$y = f(x_1 . x_2 . \ldots . x_n) \quad \text{(C. 1)}$$

According to *GUM* method, the combined uncertainty of y $u_c(y)$ can be estimated as:

$$u_c^2(y) = \sum_{i=1}^{N} \left(\frac{\partial f}{\partial x_i}\right)^2 u^2(x_i) = \sum_{i=1}^{N} c_i^2 u^2(x_i) \quad \text{(C. 2)}$$

In equation (C. 2) the correlations between the input quantities have been neglected. The terms $u(x_i)$ represents the uncertainty of the input quantity x_i and the terms c_i are known as the sensitivity coefficient of y to the respective x_i. The expanded uncertainty can be estimated as:

$$U(y) = k_{ex} \cdot u_c(y) \quad \text{(C. 3)}$$

If the requirements of the applicability of the central limit theorem are met approximately, the coverage factor k_{ex} can be calculated from the t-Student distribution for a particular coverage probability (usually 95 %) and the effective degrees of freedom ν_{eff}. This last quantity can be approximated using the Welch-Satterthwaite formula and the degrees of freedom of each input quantity ν_i as:

$$\frac{u_c^4(y)}{\nu_{eff}} = \sum_{i=1}^{N} \frac{(c_i u(x_i))^4}{\nu_i} \qquad \text{(C. 4)}$$

The *GUM* method applied to equations (3.2), (2.26), (2.27), (2.28), (4.5), (4.6), (4.7), (4.8) and (4.13), is presented in the following tables.

Table C- 1. Uncertainty on f.

Uncertainty component	Estimated value		Type	D	U	u	c	$c \cdot u$	ν_i	%
ρ_b	98.4	kg m^{-3}	A	N	3.9E+00	2.0E+00	3.1E-04	6.2E-04	200	32.4
ρ_s	3200	kg m^{-3}	B	R	1.6E+02	9.2E+01	9.6E-06	8.9E-04	200	67.6

	Estimated value		U_{rel}	D	U	u	k_{ex}	ν_{eff}
f	3.08E-02	-	7%	N	2.2E-03	1.1E-03	2.0	356

The uncertainty of f is consistent with the estimations from (Cunnington & Lee, 1996).

Table C- 2. Uncertainty on F.

Uncertainty component	Estimated value		Type	D	U	u	c	$c \cdot u$	ν_i	%
k_c(180 K)	0.0014	W m^{-1} K^{-1}	A	N	1.7E-04	8.3E-05	4.3E-01	3.5E-05	200	44.1
k_s(180 K)	66.84	W m^{-1} K^{-1}	B	R	6.7E+00	3.9E+00	8.8E-06	3.4E-05	200	40.8
f_c	0.0349	-	AB	N	2.5E-03	1.2E-03	1.7E-02	2.1E-05	356	15.1

	Estimated value		U_{rel}	D	U	u	k_{ex}	ν_{eff}
F	5.61E-04	-	19%	N	1.1E-04	5.3E-05	2.0	535

Table C- 3. Uncertainty on k_c at 1700 K.

Uncertainty component	Estimated value		Type	D	U	u	c	$c \cdot u$	ν_i	%
F	5.61E-04	-	AB	N	1.1E-04	5.3E-05	9.7E-02	5.2E-06	535	66.5
k_s(1700 K)	3.15	W m^{-1} K^{-1}	B	R	3.1E-01	1.8E-01	1.7E-05	3.1E-06	200	24.5
f	0.0308	-	AB	N	2.2E-03	1.1E-03	1.8E-03	1.9E-06	356	9.1

	Estimated value		U_{rel}	D	U	u	k_{ex}	ν_{eff}
k_c(1700 K)	5.43E-05	W m^{-1} K^{-1}	23%	N	1.3E-05	6.3E-06	2.0	871

Table C- 4. Uncertainty on k_c at 1100 K.

Uncertainty component	Estimated value		Type	D	U	u	c	$c \cdot u$	ν_i	%
F	5.61E-04	-	AB	N	1.1E-04	5.3E-05	2.2E-01	1.2E-05	535	66.5
k_s(1100 K)	7.27	W m^{-1} K^{-1}	B	R	7.3E-01	4.2E-01	1.7E-05	7.2E-06	200	24.5
f	0.0308	-	AB	N	2.2E-03	1.1E-03	4.1E-03	4.4E-06	356	9.1

	Estimated value		U_{rel}	D	U	u	k_{ex}	ν_{eff}
k_c(1100 K)	1.25E-04	W m^{-1} K^{-1}	23%	N	2.9E-05	1.5E-05	2.0	871

Table C- 5. Uncertainty on k_c at 300 K.

Uncertainty component	Estimated value		Type	D	U	u	c	$c \cdot u$	ν_i	%
F	5.61E-04	-	AB	N	1.1E-04	5.3E-05	1.2E+00	6.3E-05	535	66.5
k_s(300 K)	38.36	W m^{-1} K^{-1}	B	R	3.8E+00	2.2E+00	1.7E-05	3.8E-05	200	24.5
f	0.0308	-	AB	N	2.2E-03	1.1E-03	2.2E-02	2.3E-05	356	9.1

	Estimated value		U_{rel}	D	U	u	k_{ex}	ν_{eff}
k_c(300 K)	6.62E-04	W m^{-1} K^{-1}	23%	N	1.5E-04	7.7E-05	2.0	871

Table C- 6. Uncertainty on the modified extinction coefficient at 1700 K.

Uncertainty component	$c \cdot u$/ m^{-1}						
$v(r_1)$	7.65E+01	5.59E+01	1.28E+02	1.01E+02	1.16E+02	1.29E+02	1.30E+02
$v(r_2)$	1.63E+02	1.66E+02	1.45E+02	1.73E+02	3.32E+02	3.49E+02	2.25E+02
$v(r_3)$	1.70E+02	1.31E+02	1.44E+02	1.29E+02	1.15E+02	2.43E+02	2.72E+02
$v(r_4)$	1.02E+02	1.00E+02	9.52E+01	9.57E+01	7.35E+01	5.96E+01	8.73E+01
$v(r_5)$	4.63E+01	4.06E+01	3.18E+01	3.73E+01	3.45E+01	3.12E+01	2.24E+01
$v(r_6)$	4.33E+01	2.73E+01	2.92E+01	3.11E+01	1.89E+01	2.97E+01	2.22E+01
r_1	-7.88E+00	-7.88E+00	5.24E+00	1.43E+00	-8.61E+00	-6.52E+00	-9.38E-01
r_2	-1.01E+02	-1.01E+02	1.94E+02	8.40E+01	8.06E+01	9.14E+01	-8.55E+00
r_3	-4.55E+01	-4.55E+01	-1.00E+02	2.41E+02	-2.99E+02	-4.46E+02	-7.18E+01
r_4	1.23E+02	1.23E+02	-6.58E+01	-4.75E+01	-1.05E+01	1.10E+01	-2.20E+01
r_5	9.39E+00	9.39E+00	-6.56E+00	-1.22E+01	8.88E+00	8.64E+00	6.36E+00
r_6	-1.06E+01	-1.06E+01	6.35E+00	-6.01E+00	-2.00E+00	-1.37E+01	5.58E+00
n	4.15E-03	-1.08E-01	9.39E-02	2.70E-01	-1.09E-01	-1.20E-01	4.26E-02
k	2.74E-02	3.35E-02	2.02E-02	9.88E-03	5.96E-03	6.61E-03	3.01E-02
f	1.68E+02	1.45E+02	1.48E+02	1.48E+02	1.80E+02	2.49E+02	2.33E+02

λ/ m	5.00E-07	1.00E-06	1.50E-06	2.00E-06	2.50E-06	3.00E-06	3.50E-06
U_{rel}	15%	16%	18%	19%	20%	19%	14%
U/m^{-1}	7.26E+02	6.61E+02	7.57E+02	7.95E+02	1.05E+03	1.38E+03	9.18E+02
u/m^{-1}	3.63E+02	3.30E+02	3.78E+02	3.97E+02	5.22E+02	6.87E+02	4.58E+02
k_{ex}	2.0	2.0	2.0	2.0	2.0	2.0	2.0
v_{eff}	1396	1354	1353	983	701	738	877

Uncertainty component	$c \cdot u$/ m^{-1}						
$v(r_1)$	1.13E+02	1.05E+02	9.70E+01	8.36E+01	6.38E+01	4.56E+01	3.31E+01
$v(r_2)$	2.54E+02	2.61E+02	2.94E+02	2.74E+02	2.35E+02	2.08E+02	1.87E+02
$v(r_3)$	2.90E+02	1.81E+02	1.39E+02	1.77E+02	1.70E+02	1.77E+02	1.64E+02
$v(r_4)$	1.65E+02	1.48E+02	1.41E+02	8.96E+01	5.74E+01	6.29E+01	6.87E+01
$v(r_5)$	3.09E+01	5.26E+01	6.79E+01	6.04E+01	4.23E+01	2.60E+01	1.68E+01
$v(r_6)$	1.54E+01	2.14E+01	3.13E+01	4.85E+01	4.14E+01	2.96E+01	1.96E+01
r_1	-9.92E-01	-1.59E+00	-9.32E-01	1.50E-01	9.03E-01	9.90E-01	8.12E-01
r_2	-1.38E+02	6.27E+01	-5.30E+01	-1.60E+01	-1.56E+01	-1.88E+01	-1.25E+01
r_3	4.73E+01	2.21E+01	5.36E+01	-1.04E+02	-1.18E+02	-5.63E+01	-2.79E+01
r_4	-4.51E+01	-3.91E+00	1.68E+01	6.59E+00	1.47E+01	-1.60E+01	-2.20E+01
r_5	-4.05E-01	-1.13E+01	-2.12E+00	-2.61E+00	2.55E+00	1.48E+00	-2.69E+00
r_6	5.70E+00	2.42E+00	-4.61E-01	9.57E-01	-7.37E-01	1.90E+00	9.93E-01
n	1.43E-01	2.28E-01	2.19E-01	1.60E-01	1.26E-01	1.46E+02	1.38E+02
k	1.31E-01	6.39E-01	1.76E+00	3.77E+00	9.86E+00	1.89E+01	3.54E+01
f	2.66E+02	2.11E+02	2.00E+02	2.03E+02	1.78E+02	1.71E+02	1.57E+02

λ/ m	4.00E-06	4.50E-06	5.00E-06	5.50E-06	6.00E-06	6.50E-06	7.00E-06
U_{rel}	14%	14%	15%	15%	15%	15%	15%
U/m^{-1}	1.07E+03	8.65E+02	8.65E+02	8.50E+02	7.52E+02	7.41E+02	6.78E+02
u/m^{-1}	5.33E+02	4.32E+02	4.32E+02	4.24E+02	3.76E+02	3.70E+02	3.39E+02
k_{ex}	2.0	2.0	2.0	2.0	2.0	2.0	2.0
ν_{eff}	1051	929	753	824	852	982	984

Uncertainty component	$c \cdot u$/ m^{-1}					
$v(r_1)$	3.23E+01	3.35E+01	3.97E+01	4.61E+01	5.41E+01	7.01E+01
$v(r_2)$	1.82E+02	1.74E+02	1.86E+02	1.96E+02	2.18E+02	2.71E+02
$v(r_3)$	1.74E+02	1.80E+02	1.96E+02	2.04E+02	2.21E+02	2.69E+02
$v(r_4)$	9.64E+01	1.08E+02	1.21E+02	1.28E+02	1.38E+02	1.65E+02
$v(r_5)$	3.29E+01	4.44E+01	5.32E+01	5.79E+01	6.22E+01	7.41E+01
$v(r_6)$	2.33E+01	3.02E+01	3.85E+01	4.34E+01	4.68E+01	5.54E+01
r_1	5.45E-01	3.28E-01	1.92E-01	3.24E-02	-6.75E-02	-1.67E-01
r_2	-3.93E+00	4.49E-02	-1.17E+00	-3.97E+00	-6.75E+00	-9.61E+00
r_3	-2.40E+01	-2.05E+01	-1.87E+01	-1.79E+01	-2.13E+01	-2.56E+01
r_4	-1.25E+01	-7.90E+00	-7.00E+00	-6.49E+00	-7.21E+00	-8.22E+00
r_5	-2.75E+00	-2.66E+00	-2.21E+00	-1.93E+00	-2.06E+00	-2.28E+00
r_6	3.71E-01	-1.34E+00	-1.57E+00	-1.47E+00	-1.56E+00	-1.69E+00
n	1.29E+02	1.13E+02	9.76E+01	7.38E+01	5.63E+01	4.07E+01
k	2.61E+02	4.02E+02	5.41E+02	6.76E+02	7.76E+02	8.67E+02
f	1.68E+02	1.73E+02	1.90E+02	1.99E+02	2.18E+02	2.38E+02

λ/ m	7.50E-06	8.00E-06	8.50E-06	9.00E-06	9.50E-06	1.00E-05
U_{rel}	18%	22%	24%	28%	29%	30%
U/m^{-1}	8.71E+02	1.07E+03	1.32E+03	1.56E+03	1.77E+03	2.01E+03
u/m^{-1}	4.35E+02	5.32E+02	6.57E+02	7.78E+02	8.82E+02	9.99E+02
k_{ex}	2.0	2.0	2.0	2.0	2.0	2.0
ν_{eff}	957	556	418	345	328	344

Table C- 7. Uncertainty on the modified extinction coefficient at 1100 K.

Uncertainty component	$c \cdot u/\ \mathrm{m^{-1}}$						
$v(r_1)$	8.15E+01	5.52E+01	1.27E+02	9.54E+01	1.14E+02	1.25E+02	1.24E+02
$v(r_2)$	1.62E+02	1.62E+02	1.43E+02	1.87E+02	3.32E+02	3.10E+02	2.13E+02
$v(r_3)$	1.94E+02	1.58E+02	1.65E+02	1.31E+02	1.11E+02	2.66E+02	2.74E+02
$v(r_4)$	9.42E+01	9.53E+01	7.98E+01	1.04E+02	6.57E+01	5.45E+01	9.34E+01
$v(r_5)$	4.68E+01	3.49E+01	3.20E+01	2.78E+01	3.47E+01	2.92E+01	2.06E+01
$v(r_6)$	3.76E+01	2.32E+01	2.51E+01	3.09E+01	2.34E+01	2.94E+01	1.94E+01
r_1	-1.18E+01	-9.17E+00	3.07E+00	4.29E-01	-7.01E+00	-5.02E+00	-7.76E-01
r_2	-8.88E+01	8.01E+01	-2.70E+01	-5.02E+01	-3.64E+01	1.06E+02	-3.79E+00
r_3	-2.42E+02	-4.73E+02	-3.08E+02	-1.72E+02	8.41E+01	-2.82E+02	-9.11E+01
r_4	-5.67E+01	1.49E+00	6.90E+01	-7.02E+01	4.23E+01	4.70E+01	-1.54E+01
r_5	-9.30E+00	7.80E+00	7.28E+00	-9.17E-01	-4.45E+00	-6.42E+00	-3.65E+00
r_6	1.32E+01	8.89E+00	5.29E+00	-3.90E+00	-7.75E+00	-3.99E-01	1.56E+00
n	-2.20E-01	-2.11E-01	-1.21E-01	-3.96E-02	5.24E-02	1.83E-02	7.03E-03
k	4.94E-03	1.81E-03	1.40E-03	1.02E-03	8.58E-04	1.03E-03	6.55E-03
f	1.78E+02	1.56E+02	1.54E+02	1.53E+02	1.77E+02	2.48E+02	2.31E+02

$\lambda/\ \mathrm{m}$	5.00E-07	1.00E-06	1.50E-06	2.00E-06	2.50E-06	3.00E-06	3.50E-06
U_{rel}	17%	26%	20%	17%	17%	17%	14%
$U/\mathrm{m^{-1}}$	8.61E+02	1.14E+03	8.86E+02	7.32E+02	8.58E+02	1.17E+03	9.11E+02
$u/\mathrm{m^{-1}}$	4.30E+02	5.66E+02	4.42E+02	3.66E+02	4.28E+02	5.84E+02	4.55E+02
k_{ex}	2.0	2.0	2.0	2.0	2.0	2.0	2.0
ν_{eff}	1081	395	713	1229	513	1012	886

Uncertainty component	$c \cdot u$/ m^{-1}						
$v(r_1)$	1.09E+02	1.02E+02	9.41E+01	7.97E+01	5.93E+01	4.02E+01	2.76E+01
$v(r_2)$	2.53E+02	2.54E+02	2.86E+02	2.62E+02	2.24E+02	1.94E+02	1.69E+02
$v(r_3)$	2.64E+02	1.69E+02	1.15E+02	1.67E+02	1.66E+02	1.64E+02	1.46E+02
$v(r_4)$	1.68E+02	1.52E+02	1.26E+02	8.11E+01	4.15E+01	5.05E+01	6.24E+01
$v(r_5)$	3.52E+01	6.10E+01	6.48E+01	5.85E+01	3.53E+01	1.91E+01	1.19E+01
$v(r_6)$	1.70E+01	2.38E+01	3.58E+01	4.78E+01	3.97E+01	2.36E+01	1.28E+01
r_1	-1.15E+00	-1.50E+00	-7.52E-01	2.90E-01	9.33E-01	9.25E-01	7.09E-01
r_2	-1.09E+02	-1.01E+02	-4.57E+01	-1.46E+01	-1.67E+01	-1.75E+01	-9.12E+00
r_3	9.71E+01	2.57E+01	1.32E+02	-7.50E+01	-1.02E+02	-4.59E+01	-2.52E+01
r_4	-1.01E+01	-3.59E+01	3.19E+01	7.27E+00	3.02E+01	-3.50E+00	-1.91E+01
r_5	-7.79E+00	-1.62E+01	6.65E+00	-2.43E+00	4.90E+00	1.84E+00	-2.92E+00
r_6	-5.36E+00	-3.52E+00	-5.62E+00	-2.06E+00	-1.39E+00	9.63E-01	1.07E+00
n	1.99E-01	9.37E-02	2.73E-01	1.85E-01	1.47E-01	1.62E+02	1.37E+02
k	5.52E-02	2.57E-01	9.35E-01	1.77E+00	5.02E+00	1.18E+01	2.38E+01
f	2.53E+02	2.05E+02	1.82E+02	1.92E+02	1.68E+02	1.56E+02	1.40E+02

λ/ m	4.00E-06	4.50E-06	5.00E-06	5.50E-06	6.00E-06	6.50E-06	7.00E-06
U_{rel}	14%	15%	16%	15%	15%	16%	15%
U/m^{-1}	1.02E+03	8.62E+02	8.48E+02	7.97E+02	7.09E+02	7.02E+02	6.16E+02
u/m^{-1}	5.11E+02	4.30E+02	4.23E+02	3.98E+02	3.54E+02	3.51E+02	3.08E+02
k_{ex}	2.0	2.0	2.0	2.0	2.0	2.0	2.0
ν_{eff}	1095	1022	787	781	820	948	970

Uncertainty component	$c \cdot u$/ m^{-1}					
$v(r_1)$	2.16E+01	1.96E+01	2.07E+01	2.36E+01	2.78E+01	3.41E+01
$v(r_2)$	1.43E+02	1.21E+02	1.09E+02	1.09E+02	1.19E+02	1.38E+02
$v(r_3)$	1.37E+02	1.32E+02	1.27E+02	1.24E+02	1.29E+02	1.46E+02
$v(r_4)$	7.37E+01	7.72E+01	8.02E+01	8.22E+01	8.62E+01	9.59E+01
$v(r_5)$	2.04E+01	3.01E+01	3.57E+01	3.89E+01	4.16E+01	4.58E+01
$v(r_6)$	9.06E+00	1.65E+01	2.52E+01	3.01E+01	3.31E+01	3.62E+01
r_1	4.59E-01	2.76E-01	1.45E-01	5.62E-02	-3.70E-03	-5.53E-02
r_2	7.61E-01	4.22E+00	2.87E+00	6.44E-01	-1.16E+00	-2.78E+00
r_3	-2.17E+01	-1.49E+01	-6.45E+00	-3.77E+00	-5.07E+00	-7.75E+00
r_4	-9.91E+00	-5.71E+00	-3.79E+00	-2.38E+00	-2.10E+00	-2.73E+00
r_5	-3.83E+00	-2.38E+00	-1.33E+00	-8.38E-01	-6.84E-01	-8.30E-01
r_6	-6.30E-01	-1.77E+00	-1.21E+00	-7.44E-01	-5.87E-01	-6.80E-01
n	1.27E+02	1.17E+02	1.02E+02	7.51E+01	4.46E+01	1.86E+01
k	1.52E+02	2.56E+02	3.81E+02	5.07E+02	6.13E+02	7.07E+02
f	1.31E+02	1.24E+02	1.20E+02	1.20E+02	1.27E+02	1.44E+02

λ/ m	7.50E-06	8.00E-06	8.50E-06	9.00E-06	9.50E-06	1.00E-05
U_{rel}	17%	21%	27%	33%	37%	37%
U/m^{-1}	6.42E+02	7.35E+02	9.13E+02	1.12E+03	1.33E+03	1.52E+03
u/m^{-1}	3.21E+02	3.67E+02	4.55E+02	5.60E+02	6.60E+02	7.58E+02
k_{ex}	2.0	2.0	2.0	2.0	2.0	2.0
ν_{eff}	1194	699	393	296	268	264

Table C- 8. Uncertainty on the modified extinction coefficient at 300 K.

Uncertainty component	$c \cdot u$/ m^{-1}						
$v(r_1)$	4.95E+01	1.10E+02	1.04E+02	7.44E+01	2.18E+01	7.06E+00	1.16E+01
$v(r_2)$	1.61E+02	3.34E+02	2.43E+02	2.46E+02	1.45E+02	4.43E+01	4.95E+01
$v(r_3)$	1.70E+02	1.26E+02	2.32E+02	1.52E+02	1.25E+02	5.85E+01	5.58E+01
$v(r_4)$	9.05E+01	5.78E+01	1.63E+02	7.15E+01	5.45E+01	3.84E+01	3.86E+01
$v(r_5)$	3.42E+01	4.08E+01	3.71E+01	5.34E+01	6.24E+00	1.63E+01	1.92E+01
$v(r_6)$	2.54E+01	2.74E+01	1.36E+01	4.66E+01	5.68E+00	1.04E+01	1.57E+01
r_1	2.13E+00	-5.69E+00	-1.27E+00	4.14E-01	6.00E-01	8.58E-02	-7.24E-03
r_2	-7.69E+01	-6.30E+01	-8.47E+01	-1.42E+01	-5.58E+00	2.89E+00	-2.37E-01
r_3	-6.76E+01	-1.51E+02	1.12E+02	-3.99E+01	-2.38E+01	5.71E-01	-8.55E-01
r_4	3.24E+01	-2.03E+00	-1.03E+01	6.54E+00	-1.61E+01	-2.09E+00	-4.78E-01
r_5	-8.41E+00	-1.86E+01	-1.72E-01	1.72E+00	-1.18E+00	-8.37E-01	-2.01E-01
r_6	-8.12E+00	-1.11E+01	3.08E+00	-2.52E+00	1.38E+00	-8.67E-01	-1.98E-01
n	-9.47E-02	-1.17E-01	2.98E-01	2.06E-01	1.36E+02	9.98E+01	-1.09E+01
k	-2.17E+00	-8.16E+00	2.16E+00	-2.02E+00	2.58E+01	1.31E+02	2.75E+02
f	1.60E+02	1.85E+02	2.32E+02	1.77E+02	1.19E+02	5.36E+01	5.48E+01

λ/ m	1.00E-06	2.50E-06	4.00E-06	5.50E-06	7.00E-06	8.50E-06	1.00E-05
U_{rel}	14%	17%	14%	14%	16%	25%	38%
U/m^{-1}	6.47E+02	9.11E+02	9.51E+02	7.29E+02	5.46E+02	3.87E+02	5.92E+02
u/m^{-1}	3.23E+02	4.55E+02	4.75E+02	3.64E+02	2.73E+02	1.93E+02	2.95E+02
k_{ex}	2.0	2.0	2.0	2.0	2.0	2.0	2.0
v_{eff}	1091	608	1126	727	960	669	261

Uncertainty component	$c \cdot u$/ m^{-1}						
$v(r_1)$	2.07E+01	2.32E+02	6.82E+01	1.53E+02	2.60E+02	2.02E+02	1.67E+02
$v(r_2)$	1.28E+02	6.07E+02	4.67E+02	4.94E+02	5.79E+02	5.01E+02	4.37E+02
$v(r_3)$	1.67E+02	4.78E+02	4.76E+02	4.46E+02	4.49E+02	4.09E+02	3.64E+02
$v(r_4)$	1.20E+02	2.51E+02	2.57E+02	2.51E+02	2.42E+02	2.30E+02	2.08E+02
$v(r_5)$	5.85E+01	1.01E+02	1.00E+02	1.04E+02	1.00E+02	9.76E+01	9.05E+01
$v(r_6)$	4.60E+01	6.95E+01	6.92E+01	7.24E+01	7.04E+01	6.99E+01	6.62E+01
r_1	2.81E-01	3.71E+02	1.45E+00	-1.59E+00	-6.43E+00	-4.03E+00	-2.85E+00
r_2	7.08E+00	4.83E+03	8.35E+00	-3.16E+01	-7.28E+01	-5.36E+01	-4.39E+01
r_3	5.35E+00	5.53E+03	-7.24E+01	-6.61E+01	-8.93E+01	-7.05E+01	-5.89E+01
r_4	-1.52E+00	9.56E+02	-2.54E+01	-1.99E+01	-2.00E+01	-1.64E+01	-1.33E+01
r_5	-1.01E+00	1.56E+02	-5.44E+00	-4.88E+00	-4.52E+00	-3.95E+00	-3.21E+00
r_6	-1.02E+00	7.52E+01	-2.89E+00	-3.04E+00	-2.89E+00	-2.70E+00	-2.31E+00
n	8.00E+01	1.06E+02	4.57E+01	1.28E+01	-4.13E-01	3.96E+00	4.50E+00
k	2.67E+02	5.51E+03	-1.24E+03	-6.50E+02	-2.64E+02	-4.95E+02	9.59E+01
f	1.59E+02	4.99E+02	4.51E+02	4.47E+02	4.76E+02	4.27E+02	3.78E+02

λ/ m	1.15E-05	1.30E-05	1.45E-05	1.60E-05	1.75E-05	1.90E-05	2.05E-05
U_{rel}	18%	131%	24%	17%	15%	16%	14%
U/m^{-1}	8.20E+02	1.86E+04	3.02E+03	2.17E+03	1.99E+03	1.96E+03	1.50E+03
u/m^{-1}	4.09E+02	9.29E+03	1.51E+03	1.08E+03	9.94E+02	9.81E+02	7.51E+02
k_{ex}	2.0	2.0	2.0	2.0	2.0	2.0	2.0
ν_{eff}	833	621	418	905	1001	1063	935

Uncertainty component	$c \cdot u$/ m^{-1}						
$v(r_1)$	1.57E+02	2.36E+02	2.13E+02	2.29E+02	2.14E+02	2.11E+02	2.11E+02
$v(r_2)$	4.17E+02	5.38E+02	5.06E+02	5.31E+02	5.13E+02	5.11E+02	5.12E+02
$v(r_3)$	3.46E+02	4.17E+02	3.98E+02	4.12E+02	4.03E+02	4.03E+02	4.04E+02
$v(r_4)$	1.98E+02	2.27E+02	2.19E+02	2.24E+02	2.20E+02	2.20E+02	2.21E+02
$v(r_5)$	8.68E+01	9.66E+01	9.38E+01	9.54E+01	9.39E+01	9.40E+01	9.42E+01
$v(r_6)$	6.43E+01	7.03E+01	6.89E+01	6.99E+01	6.92E+01	6.93E+01	6.94E+01
r_1	-2.49E+00	-5.46E+00	-4.53E+00	-5.11E+00	-4.50E+00	-4.34E+00	-4.33E+00
r_2	-4.20E+01	-6.61E+01	-5.94E+01	-6.42E+01	-5.96E+01	-5.85E+01	-5.83E+01
r_3	-5.70E+01	-8.29E+01	-7.70E+01	-8.27E+01	-7.91E+01	-7.88E+01	-7.90E+01
r_4	-1.24E+01	-1.71E+01	-1.60E+01	-1.70E+01	-1.65E+01	-1.66E+01	-1.67E+01
r_5	-2.88E+00	-3.68E+00	-3.40E+00	-3.53E+00	-3.40E+00	-3.40E+00	-3.42E+00
r_6	-2.07E+00	-2.45E+00	-2.26E+00	-2.29E+00	-2.18E+00	-2.15E+00	-2.15E+00
n	4.11E+00	2.38E+00	3.46E+00	3.50E+00	4.61E+00	5.58E+00	5.94E+00
k	2.47E+02	-4.68E+02	-3.70E+02	-4.31E+02	-2.04E+02	-3.40E+02	-1.89E+02
f	3.61E+02	4.43E+02	4.21E+02	4.38E+02	4.25E+02	4.25E+02	4.26E+02

λ/ m	2.20E-05	2.35E-05	2.50E-05	2.65E-05	2.80E-05	2.95E-05	3.00E-05
U_{rel}	15%	16%	15%	16%	14%	15%	14%
U/m^{-1}	1.51E+03	2.01E+03	1.84E+03	1.96E+03	1.75E+03	1.83E+03	1.75E+03
u/m^{-1}	7.52E+02	1.01E+03	9.20E+02	9.78E+02	8.75E+02	9.15E+02	8.72E+02
k_{ex}	2.0	2.0	2.0	2.0	2.0	2.0	2.0
ν_{eff}	1065	1081	1086	1085	977	1071	965

References

Alifanov, O. M. (2017). Inverse problems in identification and modeling of thermal processes: Russian contributions. *International Journal of Numerical Methods for Heat & Fluid Flow*, *27*(3), 711–728. https://doi.org/10.1108/HFF-03-2016-0099

Alifanov, O. M., Nenarokomov, A. V, & Gonzalez, V. M. (2009). Study of multilayer thermal insulation by inverse problems method. *Acta Astronautica*, *65*(9–10), 1284–1291. https://doi.org/10.1016/j.actaastro.2009.03.053

Alifanov, O. M., Salosina, M. O., Budnik, S. A., & Nenarokomov, A. V. (2023). Design of Aerospace Vehicles' Thermal Protection Based on Heat-Insulating Materials with Optimal Structure. *Aerospace*, *10*(7), 629. https://doi.org/10.3390/aerospace10070629

Al-Jothery, H. K. M., Albarody, T. M. B., Yusoff, P. S. M., Abdullah, M. A., & Hussein, A. R. (2020). A review of ultra-high temperature materials for thermal protection system. *IOP Conference Series: Materials Science and Engineering*, *863*(1), 012003. https://doi.org/10.1088/1757-899X/863/1/012003

Arambakam, R. (2013). *Modeling Effect of Microstructure on the Performance of Fibrous Heat* [PhD Thesis]. Virginia Commonwealth University.

Arambakam, R., Tafreshi, H. V., & Pourdeyhimi, B. (2013). Dual-scale 3-D approach for modeling radiative heat transfer in fibrous insulations. *International Journal of Heat and Mass Transfer*, *64*, 1109–1117. https://doi.org/10.1016/J.IJHEATMASSTRANSFER.2013.05.047

Arambakam, R., Tafreshi, H. V., & Pourdeyhimi, B. (2014). Modeling performance of multi-component fibrous insulations against conductive and radiative heat transfer. *International Journal of Heat and Mass Transfer*, *71*, 341–348. https://doi.org/10.1016/j.ijheatmasstransfer.2013.12.031

Asllanaj, F., Brige, X., & Jeandel, G. (2007). Transient combined radiation and conduction in a one-dimensional non-gray participating medium with anisotropic optical properties subjected to radiative flux at the boundaries. *Journal of Quantitative Spectroscopy and Radiative Transfer*, *107*(1), 17–29. https://doi.org/10.1016/j.jqsrt.2007.01.060

Asllanaj, F., Jeandel, G. E., Roche, J. R., & Lacroix, D. (2004). Transient combined radiation and conduction heat transfer in fibrous media with temperature and flux boundary conditions. *International Journal of Thermal Sciences*, *43*(10), 939–950. https://doi.org/10.1016/j.ijthermalsci.2004.02.007

Asllanaj, F., Jeandel, G., & Roche, J. R. (2001). Numerical solution of radiative transfer equation coupled with nonlinear heat conduction equation. *International Journal of Numerical Methods for Heat & Fluid Flow*, *11*(5), 449–473. https://doi.org/10.1108/EUM0000000005528

Asllanaj, F., Milandri, A., Jeandel, G., & Roche, J. R. (2002). A finite difference solution of non-linear systems of radiative-conductive heat transfer equations. *International Journal for Numerical Methods in Engineering*, *54*(11), 1649–1668. https://doi.org/10.1002/nme.490

ASTM C168-22. (2022). Standard Terminology Relating to Thermal Insulation. *ASTM International, West Conshohocken, PA, 2022*.

ASTM E1269-11. (2011). Standard Test Method for Determining Specific Heat Capacity by Differential Scanning Calorimetry. *ASTM International, West Conshohocken, PA, 2018*.

ASTM E1461-13. (2022). Standard Test Method for Thermal Diffusivity by the Flash Method. *ASTM International, West Conshohocken, PA, 2022*.

Baillis, D., & Sacadura, J. F. (2000). Thermal radiation properties of dispersed media: Theoretical prediction and experimental characterization. *Journal of Quantitative Spectroscopy and Radiative Transfer*, *67*(5), 327–363. https://doi.org/10.1016/S0022-4073(99)00234-4

Banas, R., & Cunnington, G. (1974). Determination of effective thermal conductivity for the Space Shuttle Orbiter's Reusable Surface Insulation/RSI. *AIAA Paper 74-730*. https://doi.org/10.2514/6.1974-730

Bankvall, C. G. (1974). Mechanisms of heat transfer in permeable insulation and their investigation in a special guarded hot plate. In R. P. Tye (Ed.), *Heat Transmission Measurements in Thermal Insulations*. ASTM International.

Barker, A. S. (1963). Infrared lattice vibrations and dielectric dispersion in corundum. *Physical Review*, *132*(4), 1474–1481. https://doi.org/10.1103/PhysRev.132.1474

Berger, M., & Bunsell, A. (1999). *Fine Ceramic Fibers*. Taylor & Francis.

Bhattacharyya, R. (1980). Heat-Transfer Model for Fibrous Insulations. In D. McElroy & R. Tye (Eds.), *Thermal Insulation Performance* (pp. 272–286). ASTM International. https://doi.org/10.1520/STP29279S

Billard, D., Gervais, F., & Piriou, B. (1976). Analysis of Multiphonon Absorption in Corundum. *Physica Status Solidi (b)*, *75*(1), 117–126. https://doi.org/10.1002/PSSB.2220750111

Billard, D., & Piriou, B. (1974). Absorption infrarouge du corindon de 77 a 2075 K. *Materials Research Bulletin*, *9*(7), 943–950. https://doi.org/10.1016/0025-5408(74)90174-3

BIPM, IEC, IFCC, ILAC, ISO, IUPAC, IUPAP, & OIML. (2008a). *Evaluation of measurement data - Guide to the expression of uncertainty in measurement: GUM 1995 with minor corrections, JCGM 100:2008*.

BIPM, IEC, IFCC, ILAC, ISO, IUPAC, IUPAP, & OIML. (2008b). *Evaluation of measurement data—Supplement 1 to the "Guide to the expression of uncertainty in measurement"—Propagation of distributions using a Monte Carlo method. Joint Committee for Guides in Metrology, JCGM 101: 2008*.

Bittle, R. R., & Taylor, R. E. (1984). Step-Heating Technique for Thermal Diffusivity Measurements of Large-Grained Heterogeneous Materials. *Journal of the American Ceramic Society*, *67*(3), 186–194. https://doi.org/10.1111/j.1151-2916.1984.tb19739.x

Bohren, C. F., & Huffman, D. R. (1983). *Absorption and Scattering of Light by Small Particles*. John Wiley & Sons.

Boulet, P., Jeandel, G., & Morlot, G. (1993). Model of radiative transfer in fibrous media—matrix method. *International Journal of Heat and Mass Transfer*, *36*(18), 4287–4297. https://doi.org/10.1016/0017-9310(93)90113-K

Bunsell. A. (2006). Oxide Fibers. In N. Bansal (Ed.), *Handbook of Ceramic Composites* (1st ed.). Springer US.

Caps, R., Trunzer, A., Büttner, D., Fricke, J., & Reiss, H. (1984). Spectral transmission and reflection properties of high temperature insulation materials. *International Journal of Heat and Mass Transfer*, *27*(10), 1865–1872. https://doi.org/10.1016/0017-9310(84)90168-6

Caria, M. (2000). *Measurement Analysis: An Introduction To The Statistical Analysis Of Laboratory Data In Physics, Chemistry And The Life Sciences*. World Scientific Publishing Company.

Carvajal, S. A., Garboczi, E. J., & Zarr, R. R. (2019). Comparison of models for heat transfer in high-density fibrous insulation. *Journal of Research of the National Institute of Standards and Technology*, *124*(124010), 1–21. https://doi.org/10.6028/jres.124.010

Cherepanov, V. V, & Alifanov, O. M. (2017). Modeling of spectral properties and the scattering phase function for lightweight heat protection spacecraft materials. *Journal of Heat Transfer*, *139*(3), 032701. https://doi.org/10.1115/1.4034814

Cherepanov, V. V, Alifanov, O. M., Morzhukhina, A. V, & Cherepanov, A. V. (2016). Interaction of radiation with orthogonal representative elements of highly porous materials. *Applied Mathematical Modelling*, *40*(5–6), 3459–3474. https://doi.org/10.1016/j.apm.2015.03.040

Cohen, L. D., Haracz, R. D., Cohen, A., & Acquista, C. (1983). Scattering of light from arbitrarily oriented finite cylinders. *Applied Optics*, *22*(5), 742. https://doi.org/10.1364/ao.22.000742

Cordero, R. R., Seckmeyer, G., Pissulla, D., & Labbe, F. (2007). Uncertainty of experimental integrals: application to the UV index calculation. *Metrologia*, *45*(1). https://doi.org/10.1088/0026-1394/45/1/001

Crouzier, L., Delvallée, A., Allard, A., Devoille, L., Ducourtieux, S., & Feltin, N. (2019). Methodology to evaluate the uncertainty associated with nanoparticle dimensional measurements by SEM. *Measurement Science and Technology*, *30*(8), 085004. https://doi.org/10.1088/1361-6501/AB1495

Cunnington, G. R., & Lee, S. C. (1996). Radiative properties of fibrous insulations: Theory versus experiment. *Journal of Thermophysics and Heat Transfer*, *10*(3), 460–466. https://doi.org/10.2514/3.811

Cunnington, G. R., Lee, S. C., & White, S. M. (1997). Radiation heat transfer in fiber-filled silica aerogel: Comparison of theory with experiment. *National Heat Transfer Conference, 1997*. https://doi.org/10.2514/6.1997-3884

Cunnington, G. R., Lee, S. C., & White, S. M. (1998). Radiative Properties of Fiber-Reinforced Aerogel: Theory Versus Experiment. *Journal of Thermophysics and Heat Transfer*, *12*(1), 17–22. https://doi.org/10.2514/2.6318

Curran, D., & Porter, J. M. (2020). A tomography-based effective thermal conductivity model for ceramic fiber insulation. *International Journal of Heat and Mass Transfer*, *160*, 120224. https://doi.org/10.1016/J.IJHEATMASSTRANSFER.2020.120224

Daoût, C., Rozenbaum, O., Meneses, D. D. S., & Rochais, D. (2023). Identification of the spectral complex refractive index of pure silica micrometric fibers versus temperature. *International Journal of Heat and Mass Transfer*, *204*, 123869. https://doi.org/10.1016/j.ijheatmasstransfer.2023.123869

Daryabeigi, K. (1999a). *Effective thermal conductivity of high temperature insulations for reusable launch vehicles. NASA/TM-1999-208972*.

Daryabeigi, K. (1999b). Analysis and Testing of High Temperature Fibrous Insulation for Reusable Launch Vehicles. AIAA 99-1044. *37th AIAA Aerospace Sciences Meeting and Exhibit*. https://doi.org/10.2514/6.1999-1044

Daryabeigi, K. (2001). Thermal Analysis and Design of Multi-layer Insulation for Re-entry Aerodynamic Heating, AIAA 2001-2834. *35th AIAA Thermophysics Conference*. https://doi.org/10.2514/6.2001-2834

Daryabeigi, K. (2002). Heat Transfer in High-Temperature Fibrous Insulation. *8th AIAA/ASME Joint Thermophysics and Heat Transfer Conference*. https://doi.org/10.2514/6.2002-3332

Daryabeigi, K. (2003). Heat Transfer in High-Temperature Fibrous Insulation. *Journal of Thermophysics and Heat Transfer*, *17*(1), 10–20. https://doi.org/10.2514/2.6746

Daryabeigi, K. (2010). Heat transfer modeling and validation for optically thick alumina fibrous insulation. In Gaal D & Gaal P (Eds.), *Proceedings of the Joint Conferences International Thermal Conductivity Conference 30 and Thermal Expansion 18* (pp. 120–132). Destech Publications.

Daryabeigi, K., Cunnington, G., & Knutson, J. R. (2013). Heat transfer modeling for rigid high-temperature fibrous insulation. *Journal of Thermophysics and Heat Transfer*, *27*(3), 414–421. https://doi.org/10.2514/1.T3998

Daryabeigi, K., Cunnington, G. R., & Knutson, J. R. (2008). Measurement of heat transfer in unbonded silica fibrous insulation and comparison with theory. *Proceedings of the 29th International Thermal Conductivity Conference, ITCC29 and the Proceedings of the 17th International Thermal Expansion Symposium, ITES17*, 292–301.

Daryabeigi, K., Cunnington, G. R., Miller, S. D., & Knutson, J. R. (2010). Combined Heat Transfer in High Porosity High Temperature Fibrous Insulations: Theory and Experimental Validation. *10th AIAA/ASME Joint Thermophysics and Heat Transfer Conference*, 1–15. https://doi.org/10.2514/6.2010-4660

Daryabeigi, K., Miller, S. D., & Cunnington, G. R. (2007). Heat Transfer in High Temperature Multilayer Insulation. *5th European Workshop on Thermal Protection Systems and Hot Structures*.

Deirmendjian, D. (1969). *Electromagnetic Scattering on Spherical*. Elsevier.

Deutsch, T. F. (1973). Absorption coefficient of infrared laser window materials. *Journal of Physics and Chemistry of Solids*, *34*(12), 2091–2104. https://doi.org/10.1016/S0022-3697(73)80057-5

Dobrovinskaya, E. R., Lytvynov, L. A., & Pishchik, V. (2009). Properties of Sapphire. In *Sapphire* (pp. 55–176). Springer, Boston, MA. https://doi.org/10.1007/978-0-387-85695-7_2

Dombrovskii, L. A. (1996). Approximate methods for calculating radiation heat transfer in dispersed systems. *Thermal Engineering*, *43*(3), 235–243.

Dombrovsky, L. A. (1996). Quartz-fiber thermal insulation: Infrared radiative properties and calculation of radiative-conductive heat transfer. *J. Heat Transfer*, *118*(2), 408–414. https://doi.org/10.1115/1.2825859

Domoto, G. A., & Wang, W. C. (1974). Radiative transfer in homogeneous nongray gases with nonisotropic particle scattering. *Journal of Heat Transfer*, *96*(3), 385–390. https://doi.org/10.1115/1.3450210

Doremus, R. H. (2008). Alumina. In J. F. Shackelford & R. H. Doremus (Eds.), *Ceramic and Glass Materials: Structure, Properties and Processing* (pp. 1–26). Springer US. https://doi.org/10.1007/978-0-387-73362-3_1

Du, N., Fan, J., Wu, H., & Sun, W. (2009). Optimal porosity distribution of fibrous insulation. *International Journal of Heat and Mass Transfer*, *52*(19–20), 4350–4357. https://doi.org/10.1016/j.ijheatmasstransfer.2009.03.067

Fletcher, A. (1993). *Zirconia* (3rd ed.). Elsevier.

Fu, J., Croarkin, M. C., & Vorburger, T. V. (1994). The measurement and uncertainty of a calibration standard for the scanning electron microscope. *Journal of Research-National Institute of Standards and Technology*, *99*, 191.

Gembarovic, J., Freeman, J., & Taylor, D. (2010). *Thermophysical Properties of Two Materials, TPRL-Report 4443*.

Gembarovic, J., & Taylor, R. E. (2007). A method for thermal diffusivity determination of thermal insulators. *International Journal of Thermophysics*, *28*(6), 2164–2175. https://doi.org/10.1007/s10765-007-0279-7

Gervais, F., & Piriou, B. (1974). Anharmonicity in several-polar-mode crystals: adjusting phonon self-energy of LO and TO modes in Al2O3 and TiO2 to fit infrared reflectivity. *Journal of Physics C: Solid State Physics*, *7*(13), 2374. https://doi.org/10.1088/0022-3719/7/13/017

Ghosh, G. (1994). Temperature dispersion of refractive indexes in some silicate fiber glasses. *IEEE Photonics Technology Letters*, *6*(3), 431–433. https://doi.org/10.1109/68.275509

Ghosh, G. (1997). Sellmeier coefficients and dispersion of thermo-optic coefficients for some optical glasses. *Applied Optics*, *36*(7), 1540–1546. https://doi.org/10.1364/AO.36.001540

Ghosh, G., Endo, M., & Iwasaki, T. (1994). Temperature-dependent Sellmeier coefficients and chromatic dispersions for some optical fiber glasses. *Journal of Lightwave Technology*, *12*(8), 1338–1342. https://doi.org/10.1109/50.317500

Gryvnak, D. A., & Burch, D. E. (1965). Optical and infrared properties of Al2O3 at elevated temperatures. *JOSA*, *55*(6), 625–629. https://doi.org/10.1364/JOSA.55.000625

Hager, N. E., & Steere, R. C. (1967). Radiant heat transfer in fibrous thermal insulation. *Journal of Applied Physics*, *38*(12), 4663–4668. https://doi.org/10.1063/1.1709200

Hottel, H. C., Sarofim, A. F., Vasalos, I. A., & Dalzell, W. H. (1970). Multiple scatter: comparison of theory with experiment. *J. Heat Transfer*, *92*(2), 285–291. https://doi.org/10.1115/1.3449662

Houston, R. L. (1980). *Combined radiation and conduction in a nongray participating Medium that absorbs, emits, and anisotropically scatters* [PhD Thesis]. The Ohio State University.

Houston, R. L., & Korpela, S. A. (1982). Heat Transfer Through Fiberglass Insulation. *International Heat Transfer Conference 7*, 499–504. https://doi.org/10.1615/IHTC7.4040

Howell, J. R., Mengüç, M. P., Daun, K., & Siegel, R. (2020). *Thermal Radiation Heat Transfer* (7th ed.). CRC Press.

Hsieh, C. K., & Su, K. C. (1979). Thermal radiative properties of glass from 0.32 to 206 μm. *Solar Energy*, *22*(1), 37–43. https://doi.org/10.1016/0038-092X(79)90057-4

Hudson, L. K., Misra, C., Perrotta, A. J., Wefers, K., & Williams, F. S. (2000). Aluminum oxide. *Ullmann's Encyclopedia of Industrial Chemistry*.

Hussain, M., & Tao, W.-Q. (2018). Numerical prediction of effective thermal conductivity of ceramic fiber board using lattice Boltzmann method. *Numerical Heat Transfer, Part A: Applications*, *74*(6), 1285–1300. https://doi.org/10.1080/10407782.2018.1523599

Incropera, F. P., DeWitt, D. P., Bergman, T. L., & Lavine, A. S. (2006). *Introduction to Heat Transfer*. Wiley.

International Organization for Standardization (ISO). (2007). *Thermal insulation — Vocabulary. (ISO 9229)*.

International Organization for Standardization (ISO). (2015). *Statistical methods for use in proficiency testing by interlaboratory comparison. (ISO 13528)*.

Jeandel, G., Boulet, P., & Morlot, G. (1993). Radiative transfer through a medium of silica fibres oriented in parallel planes. *International Journal of Heat and Mass Transfer*, *36*(2), 531–536. https://doi.org/10.1016/0017-9310(93)80027-R

Ji, R., Zhang, Z., Liu, L., & Wang, X. (2014). Numerical modeling and experimental study of heat transfer in ceramic fiberboard. *Textile Research Journal*, *84*(4), 411–421. https://doi.org/10.1177/0040517513485630

Kamdem, H. T. T., & Baillis, D. D. (2005). Radiative heat transfer using isotropic scaling approximation: Application to fibrous medium. *J. Heat Transfer*, *127*(10), 1115–1123. https://doi.org/10.1115/1.2035108

Kamdem, H. T. T., & Baillis, D. D. (2010). Reduced models for radiative heat transfer analysis through anisotropic fibrous medium. *J. Heat Transfer*, *132*(7), 0727031–0727038. https://doi.org/10.1115/1.4000994

Kamiuto, K. (1991). Two-parameter formula for the total effective thermal conductivities of ceramic-fiber insulations. *Energy*, *16*(4), 701–706. https://doi.org/10.1016/0360-5442(91)90018-H

Kamiuto, K., Kinoshita, I., Miyoshi, Y., & Hasegawa, S. (1982). Experimental study of simultaneous conductive and radiative heat transfer in ceramic fiber insulation. *Journal of Nuclear Science and Technology*, *19*(6), 460–468. https://doi.org/10.1080/18811248.1982.9734169

Kaptein, M., & van den Heuvel, E. (2022). *Statistics for Data Scientists: An Introduction to Probability, Statistics, and Data Analysis*. Springer International Publishing.

Kaviany, M. (1995). *Principles of Heat Transfer in Porous Media* (2th ed.). Springer New York.

Kerker, M. (1969). *The Scattering of Light and Other Electromagnetic Radiation*. Academic Press.

Kim, K. S., & Lines, M. E. (1993). Temperature dependence of chromatic dispersion in dispersion-shifted fibers: Experiment and analysis. *Journal of Applied Physics*, *73*(5), 2069–2074. https://doi.org/10.1063/1.353152

Kita, J., Engelbrecht, A., Schubert, F., Groß, A., Rettig, F., & Moos, R. (2015). Some practical points to consider with respect to thermal conductivity and electrical resistivity of ceramic substrates for high-temperature gas sensors. *Sensors and Actuators B: Chemical*, *213*, 541–546. https://doi.org/10.1016/j.snb.2015.01.041

Kostikov, V., Makhova, V., Trefilov S, & Trefilov V. (1995). Ceramic fibers. In V. Kostikov (Ed.), *Fiber Science and Technology*. Springer Science + Business Media.

Koval'chyuk, N. M., Listovnichaya, S. P., & Pilipovskii, Y. L. (1991). Heat insulating materials based on the fibers of refractory oxides: A review. *Refractories*, *32*(11), 621–624. https://doi.org/10.1007/BF01280860

Kurosaki, Y., & Yamada, J. (1991). Radiation Transport in Porous or Fibrous Media. In S. Kakaç, B. Kilkiş, F. Kulacki, & F. Arinç (Eds.), *Convective Heat and Mass Transfer in Porous Media* (pp. 347–390). Springer.

Larkin, B. K., & Churchill, S. W. (1959a). Heat transfer by radiation through porous insulations. *AIChE Journal*, *5*(4), 467–474. https://doi.org/10.1002/aic.690050413

Larkin, B. K., & Churchill, S. W. (1959b). Scattering and Absorption of Electromagnetic Radiation by Infinite Cylinders. *JOSA, Vol. 49, Issue 2, Pp. 188-190*, *49*(2), 188–190. https://doi.org/10.1364/JOSA.49.000188

Le, V. T., San Ha, N., & Goo, N. S. (2021). Advanced sandwich structures for thermal protection systems in hypersonic vehicles: A review. *Composites Part B: Engineering*, *226*, 109301. https://doi.org/10.1016/j.compositesb.2021.109301

Lee, S. C. (1986). Radiative transfer through a fibrous medium: Allowance for fiber orientation. *Journal of Quantitative Spectroscopy and Radiative Transfer*, *36*(3), 253–263. https://doi.org/10.1016/0022-4073(86)90073-7

Lee, S. C. (1989). Effect of fiber orientation on thermal radiation in fibrous media. *International Journal of Heat and Mass Transfer*, *32*(2), 311–319. https://doi.org/10.1016/0017-9310(89)90178-6

Lee, S. C. (1990). Scattering phase function for fibrous media. *International Journal of Heat and Mass Transfer*, *33*(10), 2183–2190. https://doi.org/10.1016/0017-9310(90)90119-F

Lee, S. C. (1992). Dependent scattering by parallel fibers-Effects of multiple scattering and wave interference. *Journal of Thermophysics and Heat Transfer*, *6*(4), 589–595. https://doi.org/10.2514/3.11538

Lee, S. C. (1994). Dependent vs independent scattering in fibrous composites containing parallel fibers. *Journal of Thermophysics and Heat Transfer*, *8*(4), 641–646. https://doi.org/10.2514/3.593

Lee, S. C., & Cunnington, G. R. (1998a). Fiber orientation effect on radiative heat transfer through fiber composites. *7th AIAA/ASME Joint Thermophysics and Heat Transfer Conference*. https://doi.org/10.2514/6.1998-2840

Lee, S. C., & Cunnington, G. R. (1998b). Heat transfer in fibrous insulations: comparison of theory and experiment. *Journal of Thermophysics and Heat Transfer*, *12*(3), 297–303. https://doi.org/10.2514/2.6356

Lee, S. C., & Cunnington, G. R. (1998c). Theoretical Models for Radiative Transfer in Fibrous Media. *Annual Review of Heat Transfer*, *9*(9), 159–218. https://doi.org/10.1615/AnnualRevHeatTransfer.v9.50

Lee, S. C., & Cunnington, G. R. (2000). Conduction and Radiation Heat Transfer in High-Porosity Fiber Thermal Insulation. *Journal of Thermophysics and Heat Transfer*, *14*(2), 121–136. https://doi.org/10.2514/2.6508

Leviton, D. B., & Frey, B. J. (2006). Temperature-dependent absolute refractive index measurements of synthetic fused silica. *Proc. SPIE 6273, Optomechanical Technologies for Astronomy, 62732K*, *6273*, 800–810. https://doi.org/10.1117/12.672853

Li, Y., Chen, H.-W., Wang, F.-Q., Xia, X.-L., & Tan, H.-P. (2021). A development to determine spectral radiative properties of semitransparent struts of open-cell ceramic foams: From macro-scale measurement to pore-scale simulation. *Infrared Physics & Technology*, *113*, 103646. https://doi.org/10.1016/j.infrared.2021.103646

Lind, A. C., & Greenberg, J. M. (1966). Electromagnetic scattering by obliquely oriented cylinders. *Journal of Applied Physics*, *37*(8), 3195–3203. https://doi.org/10.1063/1.1703184

Lumley, N. P. G., Ford, E., Minford, E., & Porter, J. M. (2015). A simplified model for effective thermal conductivity of highly porous ceramic fiber insulation. *Journal of Thermal Science and Engineering Applications*, *7*(4), 041022. https://doi.org/10.1117/12.672853

Malitson, I. H., Murphy, F. v., & Rodney, W. S. (1958). Refractive Index of Synthetic Sapphire. *JOSA, Vol. 48, Issue 1, Pp. 72-73*, *48*(1), 72–73. https://doi.org/10.1364/JOSA.48.000072

Marschall, J., Maddren, J., & Parks, J. (2001). Internal radiation transport and effective thermal conductivity of fibrous ceramic insulations. AIAA-2822. *35th AIAA Thermophysics Conference*. https://doi.org/10.2514/6.2001-2822

Marschall, J., & Milos, F. S. (1997). The calculation of anisotropic extinction coefficients for radiation diffusion in rigid fibrous ceramic insulations. *International Journal of Heat and Mass Transfer*, *40*(3), 627–634. https://doi.org/10.1016/0017-9310(96)00109-3

Mathes, R., Blumenberg, J., & Keller, K. (1990). Radiative heat transfer in insulations with random fibre orientation. *International Journal of Heat and Mass Transfer*, *33*(4), 767–770. https://doi.org/10.1016/0017-9310(90)90174-S

Matsuoka, J., Kitamura, N., Fujinaga, S., Kitaoka, T., & Yamashita, H. (1991). Temperature dependence of refractive index of SiO2 glass. *Journal of Non-Crystalline Solids*, *135*(1), 86–89. https://doi.org/10.1016/0022-3093(91)90447-E

Matthews, L. K., Viskanta, R., & Incropera, F. P. (1984). Development of inverse methods for determining thermophysical and radiative properties of high-temperature fibrous materials. *International Journal of Heat and Mass Transfer*, *27*(4), 487–495. https://doi.org/10.1016/0017-9310(84)90022-X

McKay, N. L., Timusk, T., & Farnworth, B. (1984). Determination of optical properties of fibrous thermal insulation. *Journal of Applied Physics*, *55*(11), 4064–4071. https://doi.org/10.1063/1.332996

Milandri, A., Asllanaj, F., & Jeandel, G. (2002). Determination of radiative properties of fibrous media by an inverse method—comparison with the Mie theory. *Journal of Quantitative Spectroscopy and Radiative Transfer*, *74*(5), 637–653. https://doi.org/10.1016/S0022-4073(01)00276-X

Mironov, R. A., Gaidenko, V. O., Zabezhailov, M. O., Tomchani, O. V, Cherepanov, V. V, & Alifanov, O. M. (2021). Radiative-Optical and Thermophysical Characteristics of Fibrous Silica-Based Heat Insulation. *Journal of Engineering Physics and Thermophysics*, *94*, 1600–1608. https://doi.org/10.1007/s10891-021-02441-3

Mironov, R. A., Tomchani, O. V., Guydenko, V. O., & Zabezhailov, M. O. (2021). Numerical and experimental determination of optical properties and thermal conductivity of ceramic composites based on fumed silica and silica fiber. *International Journal of Heat and Mass Transfer*, *181*, 122022. https://doi.org/10.1016/J.IJHEATMASSTRANSFER.2021.122022

Mishchenko, M. I. (2018). "Independent" and "dependent" scattering by particles in a multi-particle group. *OSA Continuum*, *1*(1), 243–260. https://doi.org/10.1364/OSAC.1.000243

Mishra, S. C., Krishna, C. H., & Kim, M. Y. (2011). Analysis of Conduction and Radiation Heat Transfer in a 2-D Cylindrical Medium Using the Modified Discrete Ordinate Method and the Lattice Boltzmann Method. *Numerical Heat Transfer, Part A: Applications*, *60*(3), 254–287. https://doi.org/10.1080/10407782.2011.588581

Modest, M. F., & Mazumder, S. (2021). *Radiative Heat Transfer* (4th ed.). Elsevier.

Moura, L. M. (2011). Inverse Thermal Radiation Problems: Estimation of Radiative Properties of Dispersed Media. In A. Ghajar (Ed.), *Thermal Measurements and Inverse Techniques* (pp. 723–752). CRC Press.

Nenarokomov, A. V, Alifanov, O. M., Krainova, I. V, Titov, D. M., & Morzhukhina, A. V. (2019). Estimation of environmental influence on spacecraft materials radiative properties by inverse problems technique. *Acta Astronautica*, *160*, 323–330. https://doi.org/10.1016/j.actaastro.2019.04.014

Nicolau, V. de P., Raynaud, M., & Sacadura, J. F. (1994). Spectral radiative properties identification of fiber insulating materials. *International Journal of Heat and Mass Transfer*, *37*, 311–324. https://doi.org/10.1016/0017-9310(94)90032-9

Okokpujie, I. P., Essien, V., Ikumapayi, O. M., Nnochiri, E. S., Okokpujie, K., & Akinlabi, E. (2022). An Overview of Thermal Insulation Material for Sustainable Engineering Building Application. *International Journal of Design & Nature and Ecodynamics*, *17*(6), 831–841. https://doi.org/10.18280/ijdne.170603

Palik, E. D. (1998). *Handbook of Optical Constants of Solids* (Issue v. 2). Elsevier Science.

Papadopoulos, A. (2005). State of the art in thermal insulation materials and aims for future developments. *Energy and Buildings*, *37*(1), 77–86. https://doi.org/10.1016/J.ENBUILD.2004.05.006

Pelanne, C. M. (1977). Heat Flow Principles in Thermal Insulations. *Journal of Thermal Insulation*, *1*(1), 48–80. https://doi.org/10.1177/109719637700100104

Petrov, V. A. (1997). Combined radiation and conduction heat transfer in high temperature fiber thermal insulation. *International Journal of Heat and Mass Transfer*, *40*(9), 2241–2247. https://doi.org/10.1016/S0017-9310(96)00242-6

Querry, M. R. (1985). *Optical constants. Report CRDC-CR-85034 (Contractor Report CRDC-CR-85034 1985)*.

Randrianalisoa, J., Haussener, S., Baillis, D., & Lipiński, W. (2017). Radiative characterization of random fibrous media with long cylindrical fibers: Comparison of single- and multi-RTE approaches. *Journal of Quantitative Spectroscopy and Radiative Transfer*, *202*, 220–232. https://doi.org/10.1016/J.JQSRT.2017.08.002

Rauch, H., Sutton, W., & McCreight, L. (1968). *Ceramic Fibers and Fibrous Composite Materials*. Academic Press.

Reiss, H., Schmaderer, F., Wahl, G., Ziegenbein, B., & Caps, R. (1987). Experimental investigation of extinction properties and thermal conductivity of metal-coated dielectric fibers in vacuum. *International Journal of Thermophysics 1987 8:2*, *8*(2), 263–280. https://doi.org/10.1007/BF00515209

Rodney, W. S., & Spindler, R. J. (1953). Refractive index of cesium bromide for ultraviolet, visible and infrared wavelengths. *J. Res. Natl. Bur. Stand*, *3*, 123.

Rodriguez, A., & Snapp, C. (2010). Orbiter Thermal Protection System. In N. W. Hale, K. Lulla, H. W. Lane, & G. Chapline (Eds.), *Wings in Orbit: Sientific and Engineering Legacies of the Space Shuttle*. NASA.

Rolt, S. (2020). *Optical Engineering Science*. Wiley.

Sacadura, J. F. (2011). Thermal radiative properties of complex media: theoretical prediction versus experimental identification. *Heat Transfer Engineering*, *32*(9), 754–770. https://doi.org/10.1080/01457632.2011.525140

Sacadura, J. F., & Baillis, D. (2002). Experimental characterization of thermal radiation properties of dispersed media. *International Journal of Thermal Sciences*, *41*(7), 699–707. https://doi.org/10.1016/S1290-0729(02)01365-0

Schäfer, J. (2011). *Implementierung und Anwendung analytischer und numerischer Verfahren zur Lösung der Maxwellgleichungen für die Untersuchung der Lichtausbreitung in biologischem Gewebe* [PhD Thesis]. Univerität Ulm.

Schäfer, J., Lee, S. C., & Kienle, A. (2012). Calculation of the near fields for the scattering of electromagnetic waves by multiple infinite cylinders at perpendicular incidence. *Journal of Quantitative Spectroscopy and Radiative Transfer*, *113*(16), 2113–2123. https://doi.org/10.1016/J.JQSRT.2012.05.019

Schneider, C. A., Rasband, W. S., & Eliceiri, K. W. (2012). NIH Image to ImageJ: 25 years of image analysis. *Nature Methods*, *9*(7), 671–675. https://doi.org/10.1038/nmeth.2089

Seydibeyoglu, M. O., Mohanty, A. K., & Misra, M. (2017). *Fiber Technology for Fiber-Reinforced Composites*. Elsevier Science.

Song, W. F., & Yu, W. D. (2012). Heat transfer through fibrous assemblies by fractal method. *Journal of Thermal Analysis and Calorimetry*, *110*(2), 897–905. https://doi.org/10.1007/s10973-011-1792-2

Stamnes, K., Thomas, G. E., & Stamnes, J. J. (2017). *Radiative Transfer in the Atmosphere and Ocean*. Cambridge University Press.

Stark, C., & Fricke, J. (1993). Improved heat-transfer models for fibrous insulations. *International Journal of Heat and Mass Transfer*, *36*(3), 617–625. https://doi.org/10.1016/0017-9310(93)80037-U

Tan, C. Z., & Arndt, J. (2001). The refractive index of silica glass and its dependence on pressure, temperature, and the wavelength of the incident light. In *Silicon-Based Material and Devices* (pp. 51–91). Elsevier.

Thomas, M. E. (1991). Temperature Dependence of the Complex Index of Refraction. In E. D. Palik (Ed.), *Handbook of optical constants of solids* (pp. 177–199). Academic Press.

Thomas, M. E. (2006). *Optical Propagation in Linear Media: Atmospheric Gases and Particles, Solid-State Components, and Water*. Oxford University Press.

Thomas, M. E., Andersson, S. K., Sova, R. M., & Joseph, R. I. (1998). Frequency and temperature dependence of the refractive index of sapphire. *Infrared Physics & Technology*, *39*(4), 235–249. https://doi.org/10.1016/S1350-4495(98)00010-3

Thomas, M. E., & Joseph, R. I. (1988). A comprehensive model for the intrinsic transmission properties of optical windows. *Proc. SPIE 0929, Infrared Optical Materials IV*, *929*, 87–93. https://doi.org/10.1117/12.945855

Thomas, M. E., Joseph, R. I., & Tropf, W. J. (1988). Infrared transmission properties of sapphire, spinel, yttria, and ALON as a function of temperature and frequency. *Applied Optics, Vol. 27, Issue 2, Pp. 239-245*, *27*(2), 239–245. https://doi.org/10.1364/AO.27.000239

Tilioua, A., Libessart, L., & Lassue, S. (2018). Characterization of the thermal properties of fibrous insulation materials made from recycled textile fibers for building applications:

Theoretical and experimental analyses. *Applied Thermal Engineering*, *142*, 56–67. https://doi.org/10.1016/j.applthermaleng.2018.06.071

Tong, T. W., McElroy, D. L., & Yarbrough, D. W. (1985). Transient conduction and radiation heat transfer in porous thermal insulations. *Journal of Thermal Insulation*, *9*(1), 13–29. https://doi.org/10.1177/109719638500900103

Tong, T. W., Swathi, P. S., & Cunnington, G. R. (1987). Examination of the Radiative Properties of Coated Silica Fibers: *Journal of Thermal Insulation*, *11*(1), 7–31. https://doi.org/10.1177/109719638701100103

Tong, T. W., & Tien, C. L. (1980). Analytical models for thermal radiation in fibrous insulations. *Journal of Building Physics*, *4*(1), 27–44. https://doi.org/10.1177/109719638000400102

Tong, T. W., & Tien, C. L. (1983). Radiative Heat Transfer in Fibrous Insulations—Part I: Analytical Study. *Journal of Heat Transfer*, *105*(1), 70–75. https://doi.org/10.1115/1.3245561

Tong, T. W., Yang, Q. S., & Tien, C. L. (1983). Radiative Heat Transfer in Fibrous Insulations—Part II: Experimental Study. *Journal of Heat Transfer*, *105*(1), 76–81. https://doi.org/10.1115/1.3245562

Touloukian, Y. S., Powell, R. W., Ho, C. Y., & Klemens, P. G. (1971). *Thermal Conductivity-Nonmetallic Solids. Thermophysical Properties of Matter - The TPRC Data Series* (Vol. 2). IFI/Plenum.

Tritt, T. M. (2006). *Thermal Conductivity: Theory, Properties, and Applications*. Springer US.

Tychanicz-Kwiecień, M., Wilk, J., & Gil, P. (2019). Review of High-Temperature Thermal Insulation Materials. *Journal of Thermophysics and Heat Transfer*, *33*(1), 271–284. https://doi.org/10.2514/1.T5420

Uyanna, O., & Najafi, H. (2020). Thermal protection systems for space vehicles: A review on technology development, current challenges and future prospects. *Acta Astronautica*, *176*, 341–356. https://doi.org/10.1016/j.actaastro.2020.06.047

van de Hulst, H. C. (1981). *Light Scattering by Small Particles*. Dover Publications.

Vanmol, D., & Anderson, J. (1992). Heat transfer characteristics of hypersonic waveriders with an emphasis on leading edge effects. *27th Thermophysics Conference*. https://doi.org/10.2514/6.1992-2920

Veiseh, S., & Hakkaki-Fard, A. (2009). Numerical modeling of combined radiation and conduction heat transfer in mineral wool insulations. *Heat Transfer Engineering*, *30*(6), 477–486. https://doi.org/10.1080/01457630802529065

Veiseh, S., Khodabandeh, N., & Hakkaki-Fard, A. (2009). Mathematical models for thermal conductivitydensity relationship in fibrous thermal insulations for practical applications. *Asian Journal of Civil Engineering*, *10*(2), 201–214.

Verschoor, J. D., Greebler, P., & Manville, N. J. (1952). Heat transfer by gas conduction and radiation in fibrous insulation. *Transactions of The American Society Of Mechanical Engineersf Mechanical Engineers*, 961–968. https://doi.org/10.1115/1.4015979

Vozár, L., & Srámková, T. (1997). Step heating method for thermal diffusivity measurement. *Proceedings of the XIV IMEKO World Congress*, 179–184.

Wang, K. Y., & Tien, C. L. (1983). Radiative heat transfer through opacified fibers and powders. *Journal of Quantitative Spectroscopy and Radiative Transfer*, *30*(3), 213–223. https://doi.org/10.1016/0022-4073(83)90059-6

Williams, S. D., & Curry, D. M. (1977). An analytical and experimental study for surface heat flux determination. *Journal of Spacecraft and Rockets*, *14*(10), 632–637. https://doi.org/10.2514/3.27987

Williams, S. D., & Curry, D. M. (1992). *Thermal protection materials: Thermophysical property data - NASA Reference Publication 1289*.

Williams, S. D., & Curry, D. M. (1993). *Prediction of rigid silica based insulation conductivity, NASA TP- 3276*.

Wilson, D. (2018). Continuous oxide fibers. In A. Bunsell (Ed.), *Handbook of Properties of Textile and Technical Fibres* (2nd ed.). Elsevier.

Wood, D. L., & Nassau, K. (1982). Refractive index of cubic zirconia stabilized with yttria. *Applied Optics*, *21*(16), 2978–2981.

Worrell, C. A. (1986). Infrared optical constants for CO2 laser waveguide materials. *Journal of Materials Science 1986 21:3*, *21*(3), 781–787. https://doi.org/10.1007/BF01117354

Wray, J. H., & Neu, J. T. (1969). Refractive index of several glasses as a function of wavelength and temperature. *JOSA*, *59*(6), 774–776. https://doi.org/10.1364/JOSA.59.000774

Xiao, B., Wang, W. E. I., Fan, J., Chen, H., Hu, X., Zhao, D., Zhang, X., & Ren, W. E. N. (2017). Optimization of the fractal-like architecture of porous fibrous materials related to permeability, diffusivity and thermal conductivity. *Fractals*, *25*(03), 1750030. https://doi.org/10.1142/S0218348X1750030X

Xie, Z., Xue, W., Chen, H., & Huang, Y. (2011). Mechanical and thermal properties of 99% and 92% alumina at cryogenic temperatures. *Ceramics International*, *37*(7), 2165–2168. https://doi.org/10.1016/j.ceramint.2011.03.066

Yang, J., Wu, H., Wang, M., He, S., & Huang, H. (2016). Prediction and optimization of radiative thermal properties of ultrafine fibrous insulations. *Applied Thermal Engineering*, *104*(5), 394–402. https://doi.org/10.1016/j.applthermaleng.2016.05.062

Yang, J., Wu, H., Wang, M., & Liang, Y. (2018). Prediction and optimization of radiative thermal properties of nano TiO2 assembled fibrous insulations. *International Journal of Heat and Mass Transfer*, *117*, 729–739. https://doi.org/10.1016/j.ijheatmasstransfer.2017.09.069

Yeh, Hy., & Roux, J. A. (1988). Spectral radiative properties of fiberglass insulation. *Journal of Thermophysics and Heat Transfer*, *2*(1), 75–81. https://doi.org/10.2514/3.56218

Yuen, W., Takara, E., & Cunnington G. (2003, March 16). Combined conductive/radiative heat transfer in high porosity fibrous insulation materials: theory and experiment. *The 6th ASME-JSME Thermal Engineering Joint Conference*.

Yuen, W. W., & Cunnington, G. (2007). Radiative heat transfer analysis of fibrous insulation materials using the zonal-GEF method. *Journal of Thermophysics and Heat Transfer*, *21*(1), 105–113. https://doi.org/10.2514/1.22412

Zarr, R. R. (1997). Standard Reference Materials: Glass Fiberboard, SRM 1450c, for Thermal Resistance from 280 K to 340 K. *NIST Special Publication*, *260*, 130. https://doi.org/10.6028/NIST.SP.260-130

Zarr, R. R. (2001). A history of testing heat insulators at the national institute of standards and technology. *Ashrae Transactions*, *107*(Pt.2), 661–672.

Zhang, B., Zhao, S., & He, X. (2008). Experimental and theoretical studies on high-temperature thermal properties of fibrous insulation. *Journal of Quantitative Spectroscopy and Radiative Transfer*, *109*(7), 1309–1324. https://doi.org/10.1016/j.jqsrt.2007.10.008

Zhang, B., Zhao, S., He, X., & Du, S. (2007). High temperature thermal physical properties of high-alumina fibrous insulation. *Journal of Materials Science & Technology*, *23*(6), 860.

Zhao, S., Zhang, B., Du, S., & He, X. (2009). Inverse identification of thermal properties of fibrous insulation from transient temperature measurements. *International Journal of Thermophysics*, *30*, 2021–2035. https://doi.org/10.1007/s10765-009-0680-5

Zhao, S., Zhang, B., & He, X. (2009). Temperature and pressure dependent effective thermal conductivity of fibrous insulation. *International Journal of Thermal Sciences*, *48*(2), 440–448. https://doi.org/10.1016/j.ijthermalsci.2008.05.003

Zhao, S., Zhang, B. M., & Du, S. Y. (2009). An inverse analysis to determine conductive and radiative properties of a fibrous medium. *Journal of Quantitative Spectroscopy and Radiative Transfer*, *110*(13), 1111–1123. https://doi.org/10.1016/j.jqsrt.2009.03.022

ZIRCAR Ceramics, Inc. (2020). *Alumina Paper Type APA*. https://www.zircarceramics.com/product/apa/

Zuev, A. V., & Prosuntsov, P. V. (2014). Model of the Structure of Fibrous Heat-Insulating Materials for Analyzing Combined Heat Transfer Processes. *Journal of Engineering Physics and Thermophysics*, *87*(6), 1374–1385. https://doi.org/10.1007/s10891-014-1140-z

Zverev, V. G., Gol'din, V. D., & Nazarenko, V. A. (2008). Radiation-conduction heat transfer in fibrous heat-resistant insulation under thermal effect. *High Temperature*, *46*, 108–114. https://doi.org/10.1134/s10740-008-1015-0